

3-D Visualization of Solvent Displacement Processes Using Laser Technology

by

Fang Fang

A thesis submitted in partial fulfillment of the requirements for the degree of

Master of Science

in

Petroleum Engineering

Department of Civil and Environmental Engineering  
University of Alberta

© Fang Fang, 2015

## **Abstract**

A technique to visualize miscible displacement in porous media using laser and the analysis of the results for different processes are presented in this thesis. After saturating the model made of different sized glass beads with oil, solvent was introduced either under dynamic (injection and production through a pair of horizontal wells) or static (diffusion of solvent into oil saturated model) conditions. The former simulates the VAPEX (vapor extraction) process dictated by viscous and gravitational forces and the latter (“diffusion experiments”) represents diffusion/gravity (and thereby convection) controlled displacement of oil by the solvent contacting the porous medium saturated with oil.

The refractive indices of saturated and injected fluids were made the same by mixing the fluids with lower and higher indices of refraction to make the model fully transparent. Fluorescent dyes that were only visible with excitation of laser were dissolved in the solvent. A laser sheet scanned the model while synchronous pictures were taken by two high speed cameras from two sides of the model. 2-D images obtained through this process were converted to 3-D visual data and qualitative and quantitative analyses were conducted.

An optimized injection method for the VAPEX process was determined by testing different - constant and variable- injection rates. The effect of solvent gravity and viscosity on the displacement (chamber growth) process was also analyzed through the 3-D images. Diffusion was the major factor in the transition zone at the edge of solvent chamber, as well as the solvent propagation from fracture to rock matrices.

“Diffusion” experiments were done to analyze the sweep and smoothness of the front (diffusion) interface for different pore sizes, solvent/oil gravity and viscosity ratios, and the boundary effects. The box-counting fractal dimension of the solvent diffusion front in 3-D was applied to compare the progress of the solvent-oil interfaces (mixing process) for different conditions.

## **Acknowledgements**

The process of making the decision to change my major from physics to Petroleum Engineering was a long one. I would like to thank my parents who encouraged me to study engineering. It was Dr. Tayfun Babadagli, my supervisor, who gave me the chance to work on such an interesting topic and who provided generous guidance, support, and valuable advice. I would like to show my gratitude to him. He would always answer my questions and provide me with hints or a way to solve problems.

I am highly appreciative of Dr. David Redford whose lectures enlightened my knowledge in heavy oil and oil sands recovery processes. The knowledge learned from his classes helped me to understand the first SAGD papers I read, which are closely related my research topic.

Special thanks to Dr. Tayfun Babadagli, NSERC Industrial Research Chair in Unconventional Oil Recovery (industrial partners are CNRL, Saudi Aramco, SUNCOR, Petrobank, Sherritt Oil, APEX Eng., PEMEX, Statoil, and Husky Energy), for his financial support. I am also grateful to the Faculty of Graduate Studies and Research (FGSR) and Graduate Students' Association (GSA) for funding the trip to SPE Annual Technical Conference and Exhibition in Amsterdam, Netherlands.

I would also like to thank the technical staff Todd Kinnee for his brilliant suggestions and modification on my experimental apparatus. I also appreciate my volunteer Yifei Yan for helping me with data acquisition and image processing in winter and summer 2015, Pam Keegan who carefully edited my papers, and all others in the EOGRRRC group for listening to my long complaining.

# Table of Content

<b>CHAPTER 1: Introduction</b> .....	<b>1</b>
1.1 Overview .....	2
1.2 Background and Statement of the Problem.....	3
1.3 Research Objectives .....	4
1.4 Structure of the Thesis.....	5
1.5 References .....	7
<b>CHAPTER 2: 3-D Visualization of Diffusive and Convective Solvent Transport Processes in Oil Saturated Porous Media Using Laser Technology</b> .....	<b>8</b>
2.1 Preface.....	9
2.2 Introduction .....	10
2.3 Experimental Set-up and Details.....	13
2.3.1 Experimental set-up.....	13
2.3.2 Refractive index matching.....	15
2.3.3 Model.....	17
2.3.4 Image processing .....	19
2.4 Experimental Results and Analysis.....	20
2.4.1 Diffusion of solvent-1 into 5 cm model.....	20
2.4.2 Diffusion of solvent-2 into 5 cm model.....	22
2.4.3 Injection of solvent-2 into VAPEX model at the injection rate of 1 ml/min.....	24
2.4.4 Injection of solvent-2 into VAPEX model at the injection rate of 1.5 ml/min.....	26
2.5 Conclusions .....	31
2.6 References .....	32
<b>CHAPTER 3: Three Dimensional Visualization of Solvent Chamber Growth during the VAPEX Processes: An Experimental Approach Using Laser</b> .....	<b>35</b>
3.1 Preface.....	36
3.2 Introduction .....	37
3.3 Experimental Details .....	40
3.3.1 Model.....	40
3.3.2 Refractive index matching.....	40
3.3.3 Experimental set-up.....	41
3.3.4 Determination of injection rates .....	42

3.3.5 Other experiment variables.....	43
3.4 Experimental Results and Analysis.....	44
3.4.1 Chamber size .....	44
3.4.2 Solvent flow between the wells .....	46
3.4.3 Fingering phenomenon .....	46
3.4.4 Downward displacement .....	47
3.4.5 Production curves .....	48
3.4.6 Comparison with 2-D models.....	49
3.4.7 Heterogeneity.....	53
3.4.8 Lower viscosity and density solvent.....	54
3.5 Conclusions and Remarks .....	55
3.6 References .....	57
<b>CHAPTER 4: 3-D Visualization of Solvent Diffusion into Oil Saturated Porous Media Using Laser Technology and Fractal Analysis of the Mixing/Displacement Process.....</b>	<b>80</b>
4.1 Preface.....	81
4.2 Introduction.....	82
4.3 Experimental Theory and Details.....	83
4.3.1 Model.....	84
4.3.2 Refractive index matching.....	84
4.3.3 Experimental set-up (Fig. 3).....	85
4.3.4 Image processing and fractal dimension (box-counting analysis).....	85
4.4 Experimental Results and Analysis.....	86
4.4.1 Solvent 1 diffusion into 4 mm glass beads packed plexiglass (oil-wet) wall model....	86
4.4.2 Solvent 2 diffusion into 4 mm glass beads packed plexiglass (oil-wet) wall model....	87
4.4.3 Solvent 2 diffusion into 4 mm glass beads packed glass (water-wet) wall model .....	88
4.4.4 Solvent 2 diffusion into 1 mm glass beads packed glass (water-wet) wall model .....	89
4.4.5 Solvent 3 diffusion into 4 mm glass beads packed glass (water-wet) wall model .....	90
4.4.6 Solvent 3 diffusion into 1 mm glass beads packed glass (water-wet) wall model .....	91
4.4.7 Comparison with 2-D results .....	91
4.5 Conclusions .....	92
4.6 References .....	93
<b>CHAPTER 5: Conclusions and Recommendations .....</b>	<b>110</b>

5.1 Conclusions and Contributions .....	111
5.2 Recommendations .....	114
5.3 References .....	115
<b>References .....</b>	<b>116</b>

## List of Tables

Table 2.1—Refractive index mixture rules of mixtures from two different fluids with $n_i$ as the refractive index, $\phi_i$ as the component of volume fraction, $p_i$ as the component weight fraction, and $\rho_i$ as the density ( $n=1, 2$ for fluid 1 and 2, $n= 12$ for mixture). ...	11
Table 2.2—Refractive indices of materials. ....	16
Table 2.3—Fluids used in the experiment after refractive index matching.....	16
Table 3.1—Refractive indices of original materials. ....	60
Table 3.2—Fluids used in the experiment after refractive index matching.....	60
Table 3.3—List of experiments. ....	61
Table 3.4—Parameters for experimental and theoretical model matching. ....	61
Table 4.1 Refractive indices of original materials. ....	95
Table 4.2 Fluids used in the experiment after refractive index matching.....	95
Table 4.3 List of Experiments.....	96

## List of Figures

Fig. 2.1—Experimental set-up.....	14
Fig. 2.2 —Side view of the model for injection experiment (to mimic VAPEX process) with injection rate of 1.5 ml/min during experiment. ....	15
Fig. 2.3—Model (VAPEX) before (left) and after (right) refractive index matching. ....	16
Fig. 2.4—The size of VAPEX (left) and diffusion (right) models .....	18
Fig. 2.5—The original image (left) and image after processing (right).....	20
Fig. 2.6 —Solvent 1 (blue) diffusion at 350 min in the 5 cm plastic glass model: 1 cm, 2 cm, 3 cm, 4 cm and 5 cm (left to right) from the front surface. ....	21
Fig. 2.7 —Solvent 1 (blue) diffusion at 500 min in the 5 cm plastic glass model: 1 cm, 2 cm, 3 cm, 4 cm and 5 cm (left to right) from the front surface. ....	21
Fig. 2.8 —Solvent 1 (blue) diffusion at 350 min in the 5 cm model in 3-D from different angles. 3-D image was generated from 2-D photos and rotated.....	21
Fig. 2.9—Glass beads distribution inside the model (left), along the walls (middle) and between the two patterns (right). ....	22
Fig. 2.10 —Solvent 2 (blue) diffusion at 385 min in the 5 cm plastic glass model: 1 cm, 2 cm, 3 cm, 4 cm and 5 cm (left to right) from the front surface.....	23
Fig. 2.11—Solvent 2 (blue) diffusion at 490 min in the 5 cm model in 3-D from different angles. 3-D image was generated from 2-D photos and rotated.....	23
Fig. 2.12—Solvent 2 (blue) injection in VAPEX model at 32 min with injection rate of 1 ml/min: 19 cm (left), 14 cm (middle), 7 cm (right) from the from injection port. ....	24
Fig. 2.13—Solvent 2 (blue) injection in VAPEX model at 112 min with injection rate of 1 ml/min: 19 cm (left), 14 cm (middle), 7 cm (right) from the from injection port. ....	25
Fig. 2.14 —Solvent 2 (blue) injection in VAPEX model at 298 min with injection rate of 1 ml/min: 19 cm (left), 14 cm (middle), 7 cm (right) from the from injection port. ....	25
Fig. 2.15—Solvent 2 (blue) injection in VAPEX model at 60 min with injection rate of 1.5 ml/min: 19 cm (left), 14 cm (middle), 7 cm (right) from the from injection port .....	27
Fig. 2.16 —Solvent 2 (blue) injection in VAPEX model at 320 min with injection rate of 1.5 ml/min: 19 cm (left), 14 cm (middle), 7 cm (right) from the from injection port. .	28

Fig. 2.17 —Solvent 2 (blue) injection in VAPEX model at 23 min with injection rate of 0.5 ml/min: 18 cm (left top), and 3.5 cm (right top) from the from injection port. ....	29
Fig. 2.18 —Solvent 2 (blue) injection in VAPEX model at 34 min with injection rate of 1 ml/min: 18 cm (left top), and 5 cm (right top) from the from injection port. ....	30
Figure 2.19 —Solvent 2 (blue) injection in VAPEX model at 22 min with injection rate of 1.5 ml/min: 18 cm (left top), and 3.5 cm (right top) from the from injection port. ....	30
Fig. 3.1—VAPEX model before (left) and after (right) refractive index matching (Fang and Babadagli 2014). ....	62
Fig. 3.2—Dimensions of VAPEX model. ....	62
Fig. 3.3— Laser imaging system set-up. ....	63
Fig. 3.4—VAPEX injected at 0.5 ml/min at 1 cm, 5 cm, 10 cm, 15 cm, 17.5 cm and 3-D images from the toe at 12 min.....	63
Fig. 3.5—VAPEX injected at 0.5 ml/min at 1 cm, 5 cm, 10 cm, 15 cm, 17.5 cm and 3-D images from the toe at 35 min.....	64
Fig. 3.6—VAPEX injected at 0.5 ml/min at 1 cm, 5 cm, 10 cm, 15 cm, 17.5 cm and 3-D images from the toe at 78 min.....	64
Fig. 3.7—VAPEX injected at 0.5 ml/min at 1 cm, 5 cm, 10 cm, 15 cm, 17.5 cm and 3-D images from the toe at 153 min.....	65
Fig. 3.8—VAPEX injected at 0.5 ml/min at 1 cm, 5 cm, 10 cm, 15 cm, 17.5 cm and 3-D images from the toe at 318 min.....	65
Fig. 3.9—VAPEX injected at 1.5 ml/min at 1 cm, 5 cm, 10 cm, 15 cm, 17.5 cm and 3-D images from the toe at 12 min.....	66
Fig. 3.10—VAPEX injected at 1.5 ml/min at 1 cm, 5 cm, 10 cm, 15 cm, 17.5 cm and 3-D images from the toe at 34 min.....	66
Fig. 3.11—VAPEX injected at 1.5 ml/min at 1 cm, 5 cm, 10 cm, 15 cm, 17.5 cm and 3-D images from the toe at 59 min.....	67
Fig. 3.12—VAPEX injected at 1.5 ml/min at 1 cm, 5 cm, 10 cm, 15 cm, 17.5 cm and 3-D images from the toe at 98 min.....	67
Fig. 3.13—VAPEX injected at 1.5 ml/min at 1 cm, 5 cm, 10 cm, 15 cm, 17.5 cm and 3-D images from the toe at 153 min.....	68

Fig. 3.14—VAPEX injected at 3 ml/min followed by 0.5 ml/min at 1 cm, 5 cm, 10 cm, 15 cm, 17.5 cm and 3-D images from the toe at 12 min.....	68
Fig. 3.15—VAPEX injected at 3 ml/min followed by 0.5 ml/min at 1 cm, 5 cm, 10 cm, 15 cm, 17.5 cm and 3-D images from the toe at 18 min.....	69
Fig. 3.16—VAPEX injected at 3 ml/min followed by 0.5 ml/min at 1 cm, 5 cm, 10 cm, 15 cm, 17.5 cm and 3-D images from the toe at 55 min. Two parts of the chamber are obvious: (1) Very narrow located near the injector, and (2) wide above this narrow part. ....	69
Fig. 3.17—VAPEX injected at 3 ml/min followed by 0.5 ml/min at 1 cm, 5 cm, 10 cm, 15 cm, 17.5 cm and 3-D images from the toe at 88 min. Two parts of the chamber are obvious: (1) Very narrow located near the injector, and (2) wide above this narrow part. ....	70
Fig. 3.18—VAPEX injected at 3 ml/min followed by 0.5 ml/min at 1 cm, 5 cm, 10 cm, 15 cm, 17.5 cm and 3-D images from the toe at 165 min. Two parts of the chamber are obvious: (1) Very narrow located near the injector, and (2) wide above this narrow part. ....	70
Fig. 3.19—VAPEX injected at 0.5 ml/min followed by 3 ml/min at 1 cm, 5 cm, 10 cm, 15 cm, 17.5 cm and 3-D images from the toe at 23 min.....	71
Fig. 3.20—VAPEX injected at 0.5 ml/min followed by 3 ml/min at 1 cm, 5 cm, 10 cm, 15 cm, 17.5 cm and 3-D images from the toe at 46 min.....	71
Fig. 3.21—VAPEX injected at 0.5 ml/min followed by 3 ml/min at 1 cm, 5 cm, 10 cm, 15 cm, 17.5 cm and 3-D images from the toe at 102 min.....	72
Fig. 3.22—VAPEX injected at 0.5 ml/min followed by 3 ml/min at 1 cm, 5 cm, 10 cm, 15 cm, 17.5 cm and 3-D images from the toe at 159 min.....	72
Fig. 3.23—The ratio of maximum width over maximum height of the solvent chambers with time at injection rates of 0.5 ml/min, 1.5 ml/min, and 3-0.5 ml/min.....	73
Fig. 3.24—The ratio of height at the toe and at the heel of the injector with time at injection rates of 0.5 ml/min, 1.5 ml/min, and 3-0.5 ml/min.....	73
Fig. 3.25—Solvent propagation in the injector at different time where $t_1 < t_2 < t_3$ . ....	74
Fig. 3.26—Oil concentration in the produced fluids vs. time for different injection rates and scenarios.....	74
Fig. 3.27—Oil production rate vs. time for different injection rates and scenarios. ....	75

Fig. 3.28—Matching of solvent front progressing velocity vs. injection rate at the heel (16.5 cm), in the middle (8 cm), and at the toe (1 cm). Symbols: Experimental data. Straight lines: Best matches to the experimental data using Eq. 5 and constants given in Table 4.....	75
Fig. 3.29—VAPEX injected at 1.5 ml/min into the model with low permeability zone at the top at 1 cm, 5 cm, 10 cm, 15 cm, 17.5 cm and 3-D images from the heel at 69 min. ..	76
Fig. 3.30—VAPEX injected at 1.5 ml/min into the model with low permeability zone at he top at 1 cm, 5 cm, 10 cm, 15 cm, 17.5 cm and 3-D images from the heel at 147 min. 76	76
Fig. 3.31—VAPEX injected at 0.5 ml/min into the model with low permeability zone at he top at 1 cm, 5 cm, 10 cm, 15 cm, 17.5 cm and 3-D images from the heel at 79 min. ..	77
Fig. 3.33—VAPEX injected at 1.5 ml/min into the model with low permeability zone in the middle at 1 cm, 5 cm, 10 cm, 15 cm, 17.5 cm and 3-D images from the heel at 147 min. ....	78
Fig. 3.34— Zoom of transition from low permeability zone to high permeability zone with injection rate of 1.5 ml/mim.....	78
Fig. 3.35— VAPEX (solvent 2) injected at 1.5 ml/min at 1 cm, 5 cm, 10 cm, 15 cm, 17.5 cm and 3-D images from the toe (middle) and the side (bottom) .....	79
Fig. 4.1 Dimension (a) of the oil-wet plexiglass (b) and water-wet glass (c) model.....	97
Fig. 4.2 Invisible glass beads in the fluid (oleic phase) at the bottom and the glass beads in the air at the top.....	97
Fig. 4.3 Laser imaging system set-up (Fang and Babadagli 2014).....	98
Fig. 4.4 3-D surface images of solvent 1 diffusion into 4 mm glass beads packed plexiglass (oil-wet) wall model at 180 min with threshold at 50 (left), 80 (middle) and 100 (right). ....	98
Fig. 4.5 Image processing for fractal dimension calculation from original images to binary images and outline images with thresholds of 50 (top), 80 (middle) and 100 (bottom). ....	98
Fig. 4.6 Solvent 1 diffusion into 4 mm glass beads packed plexiglass (oil-wet) wall model at 3 hrs (a), 6 hrs (b), 8 hrs (c), and 10 hrs (d). ....	99
Fig. 4.7 3-D surface images at threshold of 50 of solvent 1 diffusion into 4 mm glass beads packed plexiglass (oil-wet) wall model at 3 hrs (a), 6 hrs (b), 8 hrs (c), and 10 hrs (d). ....	99

Fig. 4.8 Fractal dimension of Solvent 1 diffusion into 4 mm glass beads packed plexiglass (oil-wet) wall model with thresholds of 50, 80 and 100. ....	100
Fig. 4.9 Fractal dimension in the center of solvent 1 diffusion in 4 mm glass beads packed plexiglass (oil-wet) wall model at different threshold (a), comparison with the whole model with thresholds of 50 (b), 80 (c), and 100 (d). ....	100
Fig. 4.10 Solvent 1 fill the pores at 3.6 cm from the front surface at 6 hrs (left) and 8 hrs (right) with a threshold of 80. ....	101
Fig. 4.11 3-D surface images at threshold of 50 of solvent 2 diffusion into 4 mm glass beads packed plexiglass (oil-wet) wall model at 3 hrs (a), 7 hrs (b), 11 hrs (c), and 15 hrs (d). ....	101
Fig. 4.12 Fractal dimension of Solvent 2 diffusion into 4 mm glass beads packed plexiglass (oil-wet) wall model with thresholds of 50, 80 and 100. ....	101
Fig. 4.13 Fractal dimension in the center of solvent 2 diffusion in 4 mm glass beads packed plexiglass (oil-wet) wall model at different thresholds (a), comparison with the whole model with threshold of 50 (b), 80 (c), and 100 (d). ....	102
Fig. 4.14 3-D surface images at threshold of 50 of solvent 2 diffusion into 4 mm glass beads packed glass (water-wet) wall model at 3 hrs (a), 5 hrs (b), 8 hrs (c), and 11 hrs (d). ....	102
Fig. 4.15 Fractal dimension of Solvent 2 diffusion into 4 mm glass beads packed glass (water-wet) wall model with thresholds of 50, 80 and 100. ....	103
Fig. 4.16 Fractal dimension in the center of solvent 2 diffusion in 4 mm glass beads packed glass (water-wet) wall model at different thresholds (a), and comparison with the whole model with thresholds of 50 (b), 80 (c), and 100 (d). ....	103
Fig. 4.17 3-D surface images at thresholds of 50 of solvent 2 diffusion into 1 mm glass beads packed glass (water-wet) wall model at 8 hrs (a), 16 hrs (b), 24 hrs (c), and 32 hrs (d). ....	104
Fig. 4.18 Fractal dimension of Solvent 2 diffusion into 1 mm glass beads packed glass (water-wet) wall model with thresholds of 50, 80 and 100. ....	104
Fig. 4.19 Fractal dimension in the center of solvent 2 diffusion in 1 mm glass beads packed glass (water-wet) wall model at different thresholds (a), and comparison with the whole model with thresholds of 50 (b), 80 (c), and 100 (d). ....	105
Fig. 4.20 3-D surface images at threshold of 50 of solvent 1 diffusion into 1 mm glass beads packed glass (water-wet) wall model at 5 min (a), 1 hrs (b), 2 hrs (c), and 3 hrs (d). ....	105

Fig. 4.21 Fractal dimension of Solvent 3 diffusion into 4 mm glass beads packed glass (water-wet) wall model with thresholds of 50, 80 and 100. ....	106
Fig. 4.22 Fractal dimension in the center of solvent 3 diffusion in 4 mm glass beads packed glass (water-wet) wall model at different thresholds (a), and comparison with the whole model with thresholds of 50 (b), 80 (c), and 100 (d). ....	106
Fig. 4.23 3-D surface images at a threshold of 50 of solvent 1 diffusion into 1 mm glass beads packed glass (water-wet) wall model at 5 min (a), 1 hrs (b), 4 hrs (c), and 7 hrs (d). ....	107
Fig. 4.24 Fractal dimension of Solvent 3 diffusion into 1 mm glass beads packed glass (water-wet) wall model with thresholds of 50, 80 and 100. ....	107
Fig. 4.25 Fractal dimension in the center of solvent 3 diffusion in 1 mm glass beads packed glass (water-wet) wall model at different thresholds (a), and comparison with the whole model with thresholds of 50 (b), 80 (c), and 100 (d). ....	108
Fig. 4.26 Comparison of 3-D and 2-D behavior (or fractal dimensions). 2-D data (blue diamond and green triangles) are from Hatiboglu and Babadagli (2005). ....	108
Fig. 4.27 Comparison of 3-D fractal dimension with “3-D versions” of 2-D fractal dimension (by adding 1 to the values given in Fig. 26). ....	109

## **CHAPTER 1: Introduction**

---

## 1.1 Overview

A great portion of the remaining oil reserves in the world fall into the heavy-oil category. High viscosity of this type of oils is the greatest challenge and can be tackled in two ways: (1) Thermal processes that heat the reservoir oil and (2) dilution of the oil by solvent injection.

Steam assisted gravity drainage (SAGD) is one of the most successful thermal methods commercially applied for extra heavy-oil and bitumen recovery. Its non-thermal version, VAPEX (vapor extraction), was proposed for reservoir types where SAGD is not applicable, such as thin formations where heat loss could be a problem.

The VAPEX process works with the similar principle as SAGD: Two horizontal wells are drilled, one above the other in a reservoir where light hydrocarbons (named as the solvent) are injected through the upper well. The solvent with less density forms a dome-shaped chamber, rises gradually and mixes with the oil at the boundary of the chamber, which is called the mixing layer. The dissolved oil drains by gravity to the horizontal well located below the injector. In this process, the expensive solvent should be used optimally for an efficient application. An optimum design of solvent injection requires a clear understanding of the diffusion, dispersion, and chamber growth (i.e., sweep of oil by injected solvent) phenomena during the process.

While a miscible fluid is injected into a fractured reservoir containing heavy-oil, a mass transfer occurs between the oil-saturated rock matrix and solvent-saturated fracture. This transfer is purely diffusive (Fickian type) but as the non-equilibrium condition is reached in the matrix due to density difference caused by mixing, gravity controlled convective mass transfer also takes place in addition to diffusion inside the rock matrix.

To understand the physics of these processes, advanced experimentation and visualization studies are needed, especially in 3-D.

## **1.2 Background and Statement of the Problem**

Use of hydrocarbon solvents in enhanced oil/heavy-oil recovery processes has received remarkable attention recently. Due to the relatively high price, hydrocarbon solvents should be used efficiently in these processes. An optimal design of solvent injection requires a clear understanding of solvent interaction with oil under diffusive and dispersive mixing, and gravitational and viscous displacement conditions. 3-D visualization experiments would be a powerful tool to study the science behind these processes.

It is commonly accepted that the steam/solvent chamber boundary is smooth in the SAGD/VAPEX process. However, Ito and Ipek (2005) stated that the chamber is dome-shaped in this type of gravity-dominated displacement with two horizontal wells, and viscous fingering may occur. Hele-Shaw model and sand/bead packed cells were used as a reference to study the thickness of the mixing layer (Das and Butler, 1998) and mass transfer (Das, 1998). 3-D visualization instead of 2-D models (Hele-Shaw or packed cells) is more reliable to avoid the boundary effect that is always present in two parallel plate models. Also, having a process implemented through a horizontal well system makes the third dimension crucially important.

Experimental analyses of oil-solvent mixing by diffusion in the presence of porous media have been practically done through core experiments. Although this type of experimentation is able to represent the process in 3-D, visualization of the frontal process may not be easily done to scrutinize the frontal progress of the mixing process. Hatiboglu and Babadagli (2004, 2007) clarified the effects of matrix shape, gravity, viscosity, and wettability through core experiments,

which may be considered a 3-D approach. They further performed parametric analyses visually using 2-D glass beads packed models under immiscible (Hatiboglu and Babadagli, 2010) and miscible conditions (Hatiboglu and Babadagli, 2007; Hatiboglu and Babadagli, 2008). A convective displacement was observed when the matrix-fracture diffusive interaction takes place in a counter-current manner.

All of these attempts, as well as many other miscible displacement applications, were made through core analysis without visualization or 2-D imaging systems. 3-D imaging of this kind of experimentation is highly restricted by the size of the model when CT-Scanners are used. As early as 1986, Chen and Wada (1986) proposed a technique for visualizing the distribution of oil, water, and quartz at different locations in a transparent model using laser. To distinguish the phases under laser, the oil and water phases were dyed with different colours of fluorescence, and the quartz did not fluoresce. In order to visualize inside the model, the refractive indices of the three phases were made the same. A 3-D laser visualization system scans the 3-D models slice-by-slice with small spacing between each other and the 2-D slices are conducted into 3-D images.

### **1.3 Research Objectives**

The main objective of the study is to understand the physics of miscible displacement during EOR process through 3-D visualization. To achieve this, we needed to reach the following sub goals:

1. As there has been no 3-D visualization study done to observe miscible EOR processes, a 3-D visualization system was designed to record the solvent flow and mixing with oil in 3-D models.

2. To find the optimum injection rate for the “best” sweep (or ideal chamber growth) in the VAPEX process, different injection schemes were applied:
  - Low injection rate, medium injection rate, high injection rate;
  - Starting with low injection rate, while the solvent has reached the top, increase the injection rate;
  - Starting with high injection rate, while the solvent has reached the top, decrease the injection rate.
3. In order to observe the effect of permeability and viscosity of solvent on the VAPEX process, a low permeable zone was placed above the injector and a lower viscosity and density solvent was injected.
4. To analyze the diffusion of solvent into oil-saturated porous medium under static conditions, different solvents were put into contact with the model made of fine and coarse porous glass beads saturated with oil in plexiglass and glass wall models.

## **1.4 Structure of the Thesis**

This is a paper-based thesis containing five chapters. Chapter 1 includes an overview, a statement of the problem, and research objectives. The following three chapters are papers either presented at conferences or submitted to journals.

Chapter 2 introduces the 3-D laser technique designed to scan refractive index matched transparent models. It also summarizes refractive index matching rules with equations and some commonly used fluids and solids for matching. The first experimental results such as 2-D pictures, some processed 2-D pictures, and few 3-D images are also included in this chapter.

Chapter 3 presents the VAPEX process in 2-D at different location in the model and 3-D images at different time. The chamber shape and expansion speed are related to injection rate. The optimum injection plan is also found by changing the injection rate and is explained by visual results. The viscosity and density affect the solvent chamber in the direction perpendicular and parallel to the wells. The effect in the shape of chamber and the transmission of solvent at the boundary of different permeability zones with the presence of a low permeability zone are presented.

In Chapter 4 fractal dimension is calculated to describe the smoothness of the solvent-oil interfaces when solvent diffused into oil-saturated porous media under static conditions. The fractal dimension values are compared for different size of pores and solvents. Experiments were repeated in plexiglass and glass wall models to clarify the effect of materials/boundary conditions on the process.

Chapter 5 lists the major conclusions of the thesis and suggestions for future works.

## 1.5 References

- Chen, J.D. and Wada, N. 1986. A New Technique for Visualizing the Distribution of Oil, Water, and Quartz Grains in a Transparent, Three-Dimensional, Porous Medium. *SPE Form Eval* **1** (2): 205–208. <http://dx.doi.org/10.2118/13349-PA>.
- Das, S.K. and Bulter, R.M. 1998. Mechanism of the Vapor Extraction Process for Heavy Oil and Bitumen. *Journal of Petroleum Science and Engineering* **21** (1-2): 43–59. [http://dx.doi.org/10.1016/S0920-4105\(98\)00002-3](http://dx.doi.org/10.1016/S0920-4105(98)00002-3).
- Das, S.K. 1998. Vapex: An Efficient Process for the Recovery of Heavy Oil and Bitumen. *SPE J.* **3** (3): 232–237. <http://dx.doi.org/10.2118/50941-PA>.
- Hatiboglu, C.U. and Babadagli, T. 2004. Experimental Analysis of Primary and Secondary Oil Recovery from Matrix by Counter-Current Diffusion and Spontaneous Imbibition. SPE 90312 paper presented at the SPE Annual Technical Conference and Exhibition, Houston, TX, 26–29 September. <http://dx.doi.org/10.2118/90312-MS>.
- Hatiboglu, C.U. and Babadagli, T. 2007. Oil Recovery by Counter-Current Spontaneous Imbibition: Effects of Matrix Shape Factor, Gravity, IFT, Oil Viscosity, Wettability, and Rock Type. *J. Pet. Sci. and Eng.* **59** (1-2): 106–122. <http://dx.doi.org/10.1016/j.petrol.2007.03.005>.
- Hatiboglu, C.U. and Babadagli, T. 2008. Diffusion Mass Transfer in Miscible Oil Recovery: Visual Experiment and Simulation. *Transport in Porous Media* **74** (2): 169–184. <http://dx.doi.org/10.1007/s11242-007-9189-1>.
- Hatiboglu, C.U. and Babadagli, T. 2010. Experimental and Visual Analysis of Co-and Counter-Current Spontaneous Imbibition for Different Viscosity Ratios, Interfacial Tensions, and Wettabilities. *J. Pet. Sci. and Eng.* **70** (3-4): 214–228. <http://dx.doi.org/10.1016/j.petrol.2009.11.013>.
- Ito, Y. and Ipek, G. 2005. Steam-Fingering Phenomenon during SAGD Process. Paper SPE-97729 presented at the SPE International Thermal Operations and Heavy Oil Symposium, Calgary, Alberta, Canada, 1–3 November. <http://dx.doi.org/10.2118/97729-MS>.

## **CHAPTER 2: 3-D Visualization of Diffusive and Convective Solvent Transport Processes in Oil Saturated Porous Media Using Laser Technology**

---

This paper is a modified and improved version of SPE-170649-MS, which was presented at SPE Annual Technical Conference and Exhibition, 27 October, Amsterdam, Netherlands. A version of this chapter has been submitted to a journal.

## 2.1 Preface

A technique to visualize miscible displacement in porous media is introduced in this paper. After saturating the model made of different sized glass beads with oil, solvent was introduced to mix and displace it. The refractive indices of saturated and injected fluids were made the same by mixing them with lower and higher indices of refraction. Rrefractive index matching made the model transparent. Fluorescent dyes that were only visible with excitation of laser were dissolved in the solvent. A laser sheet scanned the model while synchronous pictures were taken by two high speed cameras from two sides of the model. Two groups of models representing diffusive (no injection) and convective (injection of solvent) interaction, respectively, were considered to test the visualization system: (1) Solvent diffusion under purely static conditions, and (2) injection/production through a pair of horizontal wells. Visual data were analyzed and the limitations of the visualization technique introduced are presented.

## 2.2 Introduction

Use of hydrocarbon solvents in enhanced oil/heavy-oil recovery processes has received remarkable attention recently. Due to the relatively high price, hydrocarbon solvents should be used efficiently in these processes. An optimal design of solvent injection requires a clear understanding of solvent interaction with oil under diffusive and dispersive mixing, and gravitational and viscous displacement conditions. 3-D visualization experiments would be a powerful tool to study the science behind the processes.

As early as 1986, Chen and Wada (1986) proposed a technique for visualizing the distribution of oil, water, and quartz in a transparent model using laser. To distinguish the phases under laser, the oil and water phases were dyed with different colours of fluorescence, and the quartz did not fluoresce. In order to visualize inside the model, the refractive indices of the three phases were made the same. The refractive indices of liquids are commonly low compared to solids. Materials such as polymethylmethacrylate (PMMA), fuzed quartz, silica gel, and glass beads with low indices of refraction were chosen to match with the index of refraction of fluid mixtures (Wiederseiner et al., 2011). Different equations/mixture rules including the Heller equation (Heller, 1945), the Newton equation, the Lichtenecker equation, the Arago–Biot equation, the Dale–Gladstone equation, the Wiener equation, and the Lorentz–Lorenz equation (**Table 1**) can determine the refractive index of a solute (Wiederseiner et al., 2011). An image showed the distribution of the phases where the laser sheet was placed at.

Equation Name	Equation
Heller equation	$\frac{n_{12}-n_1}{n_1} = \frac{3m^2-1}{2m^2+2}$ , with $m = \frac{n_2}{n_1}$
Newton equation	$n_{12}^2 = \varphi_1 n_1 + \varphi_2 n_2$
Lichtenecker equation	$\ln n_{12} = \varphi_1 \ln n_1 + \varphi_2 \ln n_2$
Arago–Biot equation	$n_{12} = \varphi_1 n_1 + \varphi_2 n_2$
Dale–Gladstone equation	$\frac{n_{12} - 1}{\rho_{12}} = \frac{n_1 - 1}{\rho_1} p_1 + \frac{n_2 - 1}{\rho_2} p_2$
Wiener equation	$\frac{n_{12}^2 - n_1^2}{n_{12}^2 + 2n_1^2} = \varphi_2 \frac{n_2^2 - n_1^2}{n_2^2 + 2n_1^2}$
Lorentz–Lorenz equation	$\frac{n_{12} - 1}{(n_{12}^2 + 2)\rho_{12}} = \left(\frac{n_1^2 - 1}{n_1^2 + 2}\right) \frac{p_1}{\rho_1} + \left(\frac{n_2^2 - 1}{n_2^2 + 2}\right) \frac{p_2}{\rho_2}$

**Table 2.1—Refractive index mixture rules of mixtures from two different fluids with  $n_i$  as the refractive index,  $\phi_i$  as the component of volume fraction,  $p_i$  as the component weight fraction, and  $\rho_i$  as the density ( $n=1, 2$  for fluid 1 and 2,  $n=12$  for mixture).**

Obviously, the use of laser technique to visualize flow experiments in a non-porous medium is quite common. 3-D laser visualization systems with movable laser sheet and high speed CCD camera has been used for different purposes including the visualization of gas flow (Chao et al., 1990), reacting flows (Cessou et al., 2000), fuel in engine (Nygren et al., 2002), and even flames (Hut et al., 2002). Temperature could also be measured using the laser technique (Shutton and Fisher, 2008; Sakakibara and Andian, 1999). Chen et al. (2005) observed the mass transfer due to heat in a square section with a low fraction of glass beads particle suspension at the bottom in 3-D, where the fluid index of refraction was matched with the particles' and the density was matched with the emulsion tracer particles. Three dimensional imaging of 2 phase immiscible flow through a thin (1.3 cm) and small (2.5 cm x 4.5 cm) porous media was introduced by Sharma et al. (2011).

Experimental studies can be divided into two groups: (1) Solvent diffusion into an oil-saturated model (static experiments) and (2) solvent injection into an oil-saturated model through dynamic

experiments. While 3-D experimental studies of miscible displacement in porous media under static conditions are highly limited, studies on 2-D visualization of displacement processes do exist. Hatiboglu and Babadagli (2004, 2007a) conducted static experiments with air, water, solvent, and oil in cores to study the effect of matrix shape factor, gravity, viscosity, and rock type. In order to further understand how the factors influence the procedure, 2-D glass-bead-pack models were constructed for visualization (Hatiboglu and Babadagli, 2010).

In the dynamic experimentation, a limited number of visual studies have typically focused on solvent displacement. One of the most commonly searched techniques is the VAPEX (vapor extraction) process for heavy-oil recovery. In this process, solvent injected through horizontal well located on top of the producing one diffuses into oil to reduce the viscosity. This results in a gravity-dominated recovery process. It is commonly accepted that the solvent chamber boundary is smooth in the VAPEX process. However, Ito and Ipek (2005) stated that the chamber was dome-shaped in this type of gravity dominated displacement with two horizontal wells and viscous fingering may occur. 2-D glass beads pack VAPEX model for visualization was also presented by Das (1998) with similar observations. Yet, no experimental work has been reported in 3-D from in which the shape of solvent chamber along the well can be observed. This is mainly due to limitations of the 3-D model size to fit into sophisticated visualization tools such as X-ray tomography devices. Hence, a 3-D experimental system with a special imaging technique using laser was designed to clarify the physics and the mechanics of these processes. This approach allows the use of relatively larger model sizes to reflect the details that are missed at smaller scale models.

This paper presents a technique combining the above refractive index matching method and a 3-D laser imaging system to visualize the process of solvent diffusion into porous medium (under static conditions) and injection/production through a pair of horizontal wells in glass beads packed models (dynamic experiments). The former represents solvent mixing between fracture and matrix and oil recovery from the matrix in naturally/artificially fractured rocks. The latter mimics the VAPEX (vapor extraction) type process that was suggested for heavy-oil recovery from high permeability oil sands. This is why the model with an injection/production (convective transport) system will be called the VAPEX model from now on. Fluorescent dyes were introduced into the solvent so that the 3-D image systems could record solvent displacement in a dark background of oil. Each image presented the process at different points depending on the location of laser sheet. From those images, 3-D pictures can be constructed.

## **2.3 Experimental Set-up and Details**

**2.3.1 Experimental set-up (Fig. 2.1).** The experiment was operated in a dark space. A 445 nm wavelength 1.4 W power blue laser was used as the light source. The laser beam was expanded to a sheet by an expander, and a slide stage to which the laser source was fixed moved the laser sheet along the model. The solvent was colored by a yellow fluorescent dye that was visible with excitation of the laser sheet in the dark. Synchronous pictures were taken by high speed cameras located at the opposite surfaces of the model and perpendicular to the laser sheets (Fig. 2.2). Filters attached to the camera lens transmitted the yellow light of the fluorescent dyes and filtered the blue laser light, which acted as noise in the images. The apparatus was controlled by a computer program. The moving stage traveled 1 mm and two pictures were taken by the cameras from two sides of the model at each step. Once the whole model was scanned, the stage moved to the original position. Scanning the whole model only took about 13 to 50 sec depending on the size

of the models and the spacing between each picture. As long as the diffusion was slow and injection rate in the VAPEX model was low, the time during one cycle was significantly short compared to the whole process. The scans were 5 min apart for diffusion model and 15 min apart for the VAPEX model. The technique still has a problem in that the background scatters the light resulting in noise, especially when the concentration of solvent with tracer is high and bright. With shorter path length that is proportional to the distance from the image to the model surface, the image will be clearer, which is why two cameras were used.

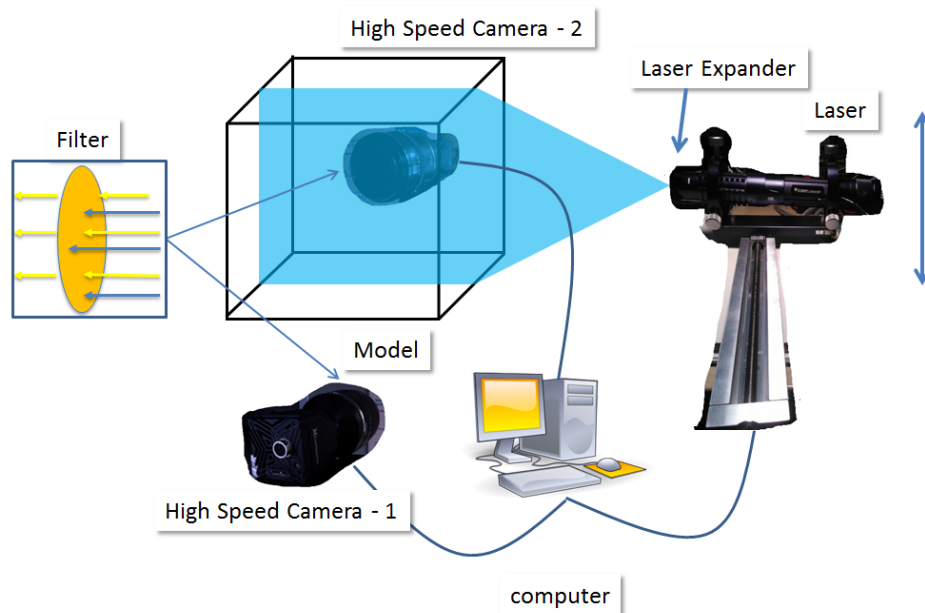


**Fig. 2.1—Experimental set-up.**

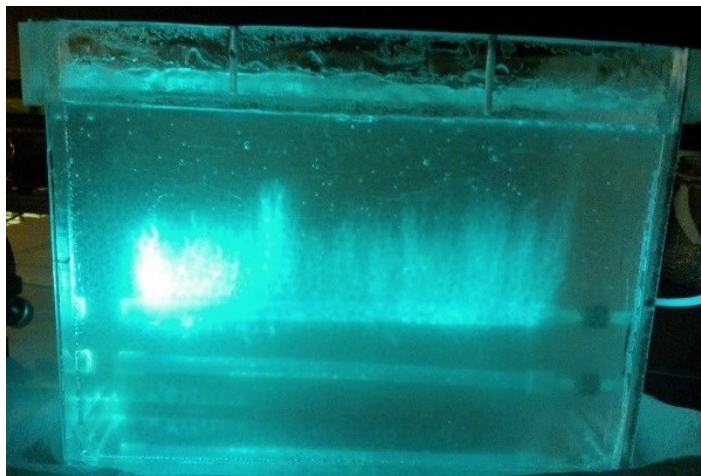


**Fig. 2.2—Side view of the model for injection experiment (to mimic VAPEX process) with injection rate of 1.5 ml/min during experiment.**

**2.3.2 Refractive index matching.** Refractive index matching is a method to visualize fluid flow in glass beads porous media, which resulted in transparency of the model system including glass beads, oil, and solvent (Fig. 2.3). Thus, the displacement of the solvent was visible if it was colored to be distinguished from oil. The index of refraction is commonly low for solvents and oil; therefore, the glass beads must have a relatively low refractive index, where in the experiment refractive index of 1.473 was chosen. The materials used for matching the indices of fluids are given in Table 2.2. Matching rules show that by mixing higher and lower refractive index fluids, the mixture would have the index of refraction between the two indices. Mixture rules were equations of volume ratios, or mass ratios with linear relation, power law, or more (Table 2.1) vary by authors (Wiederseiner et al., 2011). Thus, it was necessary to measure the refractive indices of the fluids and make corrections before every experiment. The properties of mixtures with index of refraction 1.473 are provided in Table 3.

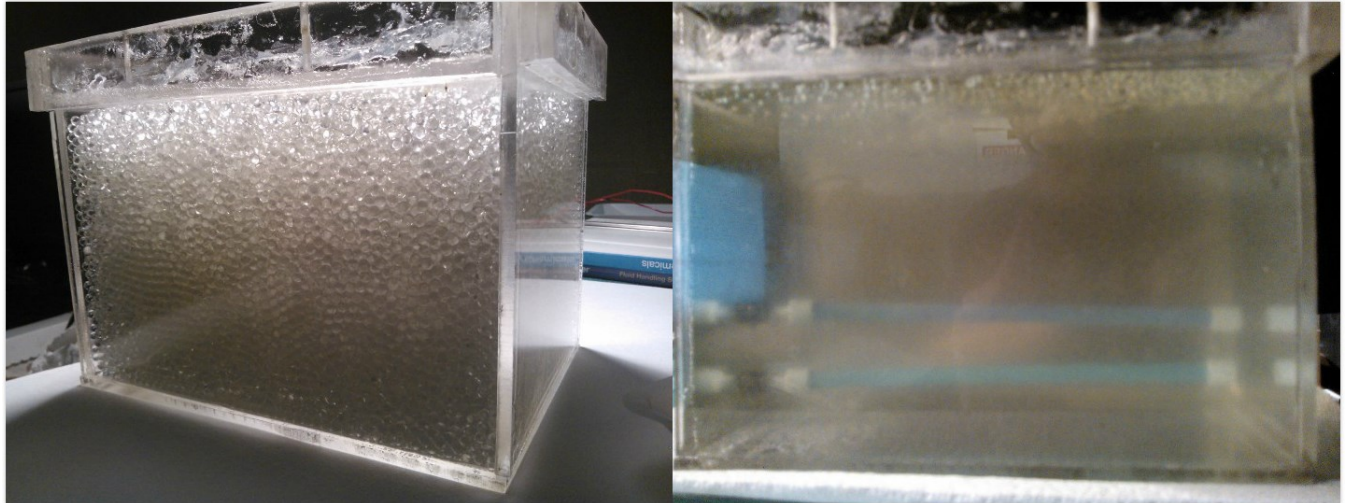


**Fig. 2.3—Model (VAPEX) before (left) and after (right) refractive index matching.**

		Refractive Index
1	Heptane	1.386
2	Kerosene	1.433
3	Light Mineral Oil	1.469
4	Heavy Mineral Oil	1.477
5	Toluene	1.497
6	Silicone Oil	1.52

**Table 2.2—Refractive indices of materials.**

		Refractive Index ±0.003	Density g/cc ±0.002	Viscosity cP ±5
Oleic Phase	Mixture 1 and 4	1.473	0.864	45
Solvent 1	Mixture 2 and 6	1.473	0.908	8
Solvent 2	Mixture 3 and 5	1.473	0.857	23
Porous Media	Glass Beads	1.473	NA	NA

**Table 2.3—Fluids used in the experiment after refractive index matching.**

Heavy mineral oil containing heptane was used as the oleic phase, while other mixtures with lower viscosities acted as solvent phases. However, the density and viscosity differences were limited due to mixing to match the index of refraction. Although the viscosity and density of

heavy mineral oil were relatively higher than most solvents, adding heptane strongly reduced them. On the other hand, to increase the refractive indices of solvents, silicone oil was considered (as recommended by other studies for this purpose) but its density was over 2 g/cc, which resulted in a denser solvent phase that was not applicable to VAPEX model. Another choice was toluene, of which density and viscosity were both low, but the refractive index was only 0.022 higher than our aim 1.473. Eventually, the silicone oil mixture (solvent-1 in **Table 3**) that yields 0.908 g/cc for solvent was selected for the pure diffusion experiment (static model), and the toluene mixture with density 0.857 g/cc (solvent-2 in **Table 2. 3**) was injected into VAPEX model (dynamic experiment).

**2.3.3 Model.** The plexiglass models were packed densely and homogeneously with glass beads for visualization. The VAPEX and diffusion models are shown in **Figure 2.4**. The diffusion model was cubic with a dimension of  $5 \times 5 \times 5 \text{ cm}^3$ . The bottom was open and covered by thick fabric layers to lift the model by several millimeters from the bottom and to assure the contact of oil and solvent was uniform through the area of the bottom part of the model. The solvent tray was 1.5 cm high. 1 mm and 4 mm diameter glass beads yielded permeability values around 70 Darcy and 1,120 Darcy, respectively, when the Kozeny-Carman equation (Mavko and Nur, 1997) was applied:

$$k = \frac{\phi^3 d^2}{72(1 - \phi)^2 \tau^2} \quad (1)$$

where  $\phi$  is the porosity,  $\tau$  is the relative roughness, and  $d$  is the diameter of the glass beads.

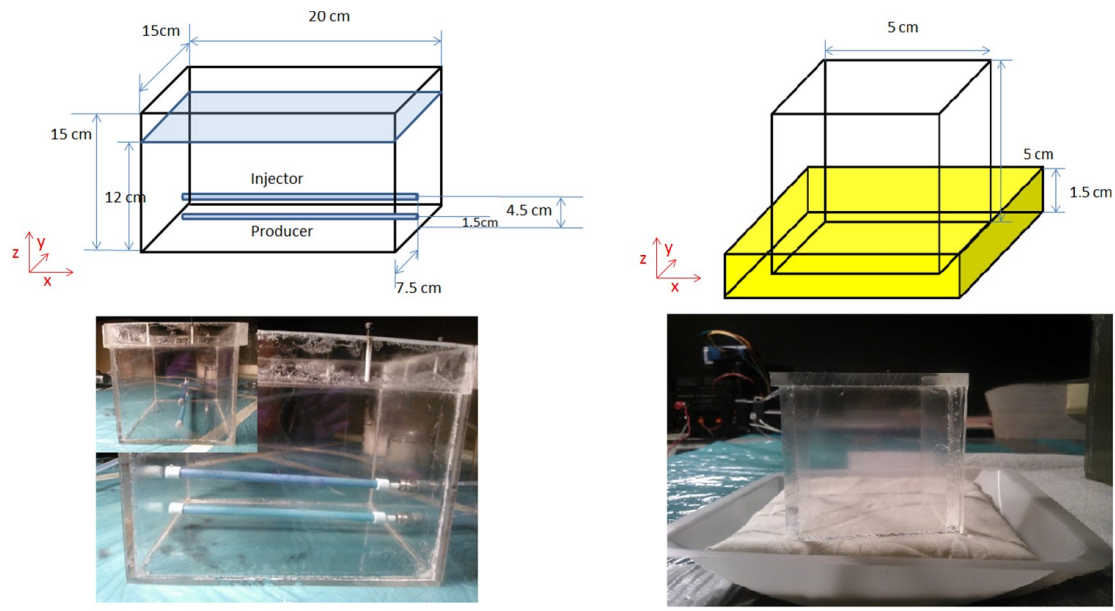


**Fig. 2.4—Size of VAPEX (left) and diffusion (right) models.**

The interaction type was counter-current diffusion; i.e., only one side of the model (bottom) was open for the interaction with solvent and all other sides were closed to flow. The level of solvent surface in the tray was about 1 cm higher than the bottom of the model. Air pressure supported the weight of oil in the model, which prevented downflow of oil through the high permeability model due to air pressure exerted from the top. The glass bead filled cubic model represented the rock matrix, while the solvent tray acted as the fracture.

The VAPEX model was 15 cm (width)  $\times$  20 cm (length)  $\times$  15 cm (height), but the lid was placed at 12 cm high. Thus, the actual size for the process was 15 cm (width)  $\times$  20 cm (length)  $\times$  12 cm (height). The two wells were drilled 1.5 cm and 4.5 cm above the bottom of the model. The wells had 1 cm end caps and 1.5 cm connectors (white section of the wells in the left picture of Fig. 2.1) of wells and injection tube at each end of the wells. Thus, the injection and production sections were 17.5 cm (blue section of the wells in the left picture of Fig. 2.1). In this particular model, 4 mm diameter glass beads were used due to the injection rate of the scaled model. The injection

rates were low enough such that gravity dominated the flow as Butler and Mokrys (1989) assumed. If the gravity-to-viscous ratio  $N_{g/v}$  was greater than  $H/L$ , gravity dominated the flow (Alkindi and Al-Wahaibi, 2011), where:

$$N_{g/v} = \frac{\rho_o - \rho_s}{\mu_{ref} \left(1 - \frac{\mu_s}{\mu_o}\right) \gamma} kg \quad (2)$$

where  $H$  is the height of the model,  $L$  is the length, and  $\gamma = \frac{q}{H\phi y}$  is the horizontal velocity in which  $q$  is the injection rate,  $\phi$  is the porosity, and  $y$  is the model length. As seen in Eq. 2, the lower the permeability is, the lower the injection rate should be. The maximum injection rates were found to be about 1.5 ml/min for 4 mm glass-bead-pack and 0.085 ml/min for 1 mm glass-bead-pack. Due to restrictions of the pump (accuracy at extremely low rates), 0.085 ml/min option that corresponds to 1 mm glass beads could not be used.

**2.3.4 Image processing.** The background (oleic phase) was subtracted from the 2-D images, while the solvent-swept area was brightened (Fig. 2.5). The solvent in the image was brighter close to the laser source especially in the larger models (VAPEX). Balancing the brightness improved the image but could not completely solve the problem. The 2-D pictures parallel to each other recorded at each position were converted into 3-D images by stacking them in line for each scan. The 3-D images at different times could be made into animation, if they were played in order at certain frequency.

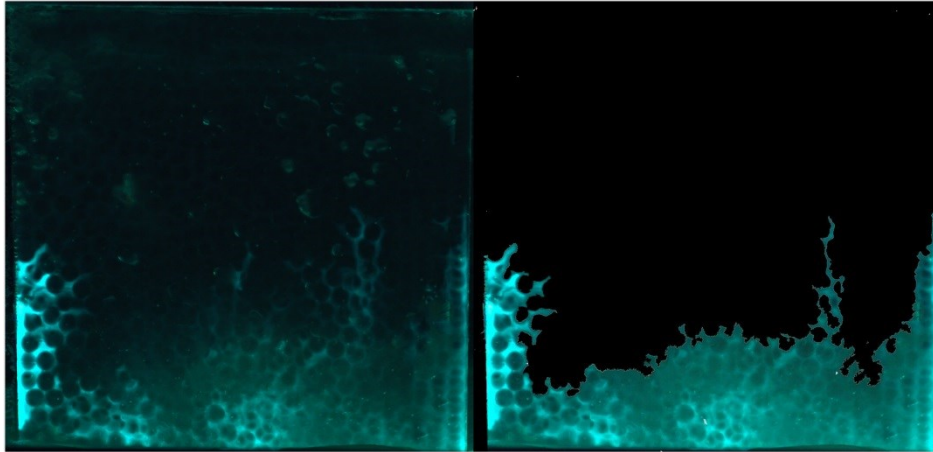


**Fig. 2.5—Original image (left) and image after processing (right).**

## **2.4 Experimental Results and Analysis**

**2.4.1 Diffusion of solvent-1 into 5 cm model.** Solvent-1 diffusion into heavy mineral oil and heptane mixture images are shown in **Figures 2.6—2.8**. **Figure 2.5** compares the original image taken by the camera (left) and its improved version after processing (right). As seen in **Figures 2.6 and 2.7**, the solvent front progress is faster at the left and right parts in each image (edges of the model). It is more obvious in 3-D image that the diffusion is faster at the back corner which is the intersection of the two walls (**Fig. 2.8**). The reasons were the oil-wet plastic glass walls of the model and the different glass beads distribution. The glass beads generally lined up horizontally inside the model (left image of **Fig. 2.9**) but distributed vertically along the left and right walls (middle image of **Fig. 2.9**). The pattern at the boundary of the two is shown in the right image of **Figure 2.9**. When the solvent reached the top surface, the solvent was drained down by gravity, which formed a convection caused by gravity and diffusion.

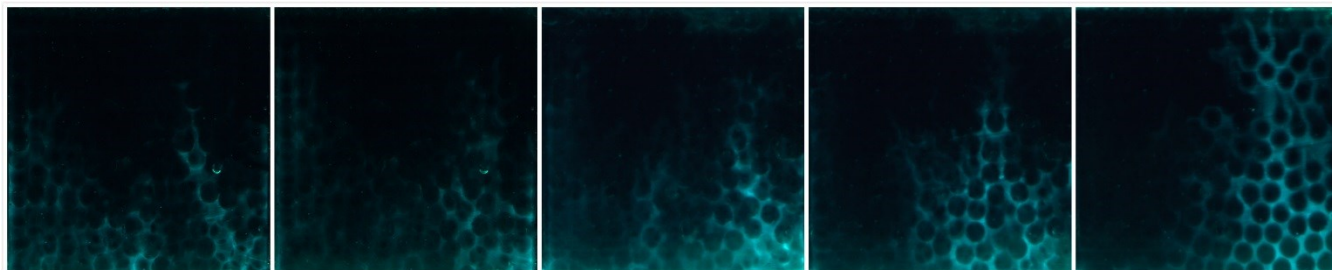


**Fig. 2.6—Solvent 1 (blue) diffusion at 350 min in the 5 cm plastic glass model: 1 cm, 2 cm, 3 cm, 4 cm and 5 cm (left to right) from the front surface.**

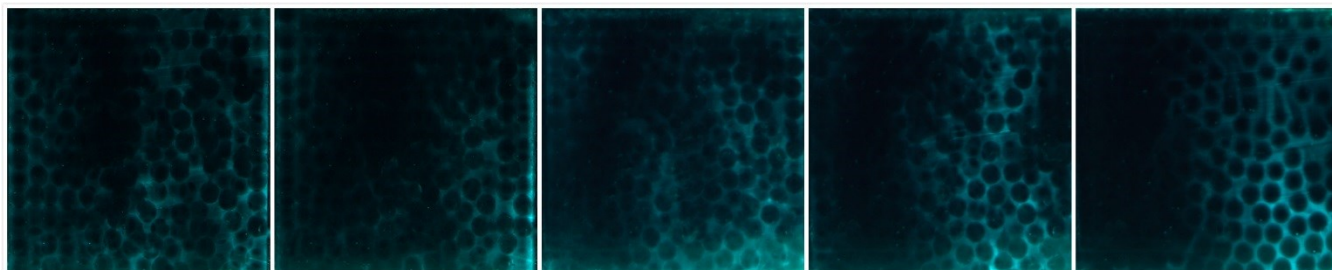


**Fig. 2.7—Solvent 1 (blue) diffusion at 500 min in the 5 cm plastic glass model: 1 cm, 2 cm, 3 cm, 4 cm and 5 cm (left to right) from the front surface.**

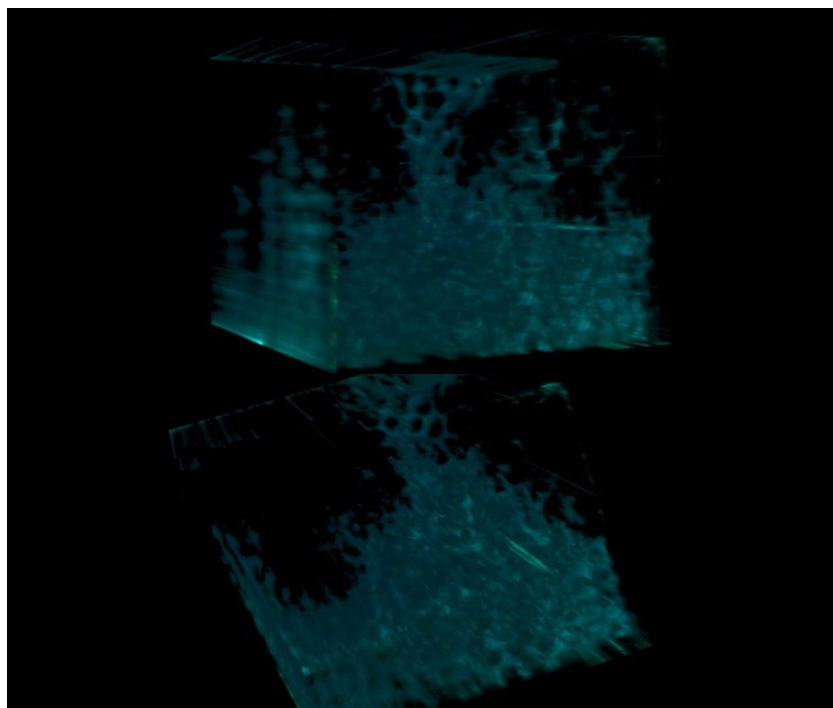


**Fig. 2.8—Solvent 1 (blue) diffusion at 350 min in the 5 cm model in 3-D from different angles. 3-D image was generated from 2-D photos and rotated.**

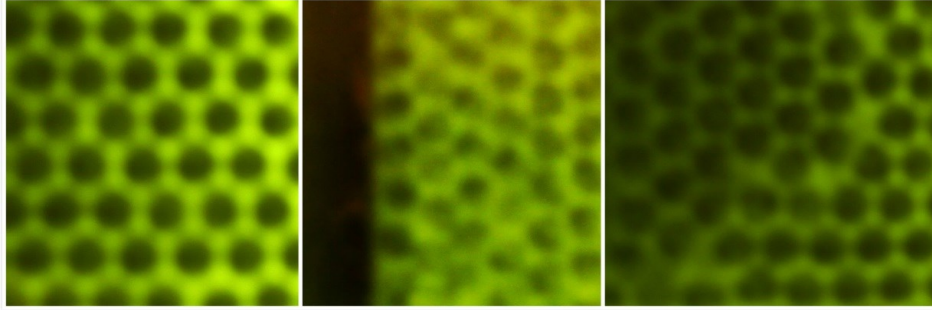


**Fig. 2.9—Glass beads distribution inside the model (left), along the walls (middle) and between the two patterns (right).**

**2.4.2 Diffusion of solvent-2 into 5 cm model.** The diffusion of less density solvent showed a similar behaviour to that of the denser solvent. The solvent front developed narrowly and faster near the sides (edges) of the model (right image of Fig. 2.10). Except for the very front image with the edges of the model at the sides (left images), the solvent always progressed faster in the middle. As the height of the solvent front increases and we move deeper into the model (left to right in Fig. 2.15—2.19), a “bullet shape” (Fig. 2.11) in the center was observed. A similar behaviour was observed by Hatiboglu and Babadagli (2008) through their 2-D visualization study on 5 x 5 cm glass bead model. They attributed this to “inner pressure distribution” that caused less resistance to flow at the middle of bottom for counter-current diffusion. The diffusion was much slower compared with the diffusion of solvent denser than oil especially at later stages. Within the range of 810 min to 1045 min, the solvent swept most of the area, but in the front image of the solvent spread around the top surface and stayed stationary due to lower density of solvent-2 compared to oil. Due to buoyancy, the process was supposed to be faster as lighter fluid rose upward. However, high viscosity slowed the process down as the solvent-2 with viscosity of 23 cP was significantly more viscous than solvent-1 with viscosity of 8 cP, where the oleic phase

was only 45 cP. As the diffusion rate for different compositions is different, further experiments need to be done to clarify the effect of the composition on the process.

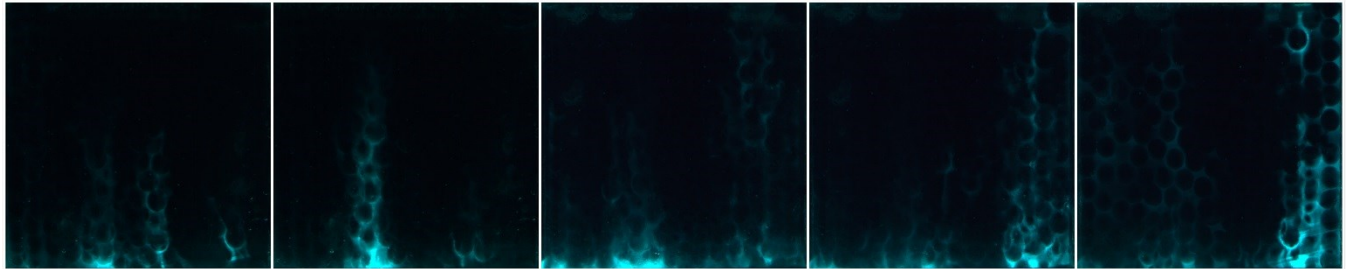


**Fig. 2.10—Solvent 2 (blue) diffusion at 385 min in the 5 cm plastic glass model: 1 cm, 2 cm, 3 cm, 4 cm and 5 cm (left to right) from the front surface.**

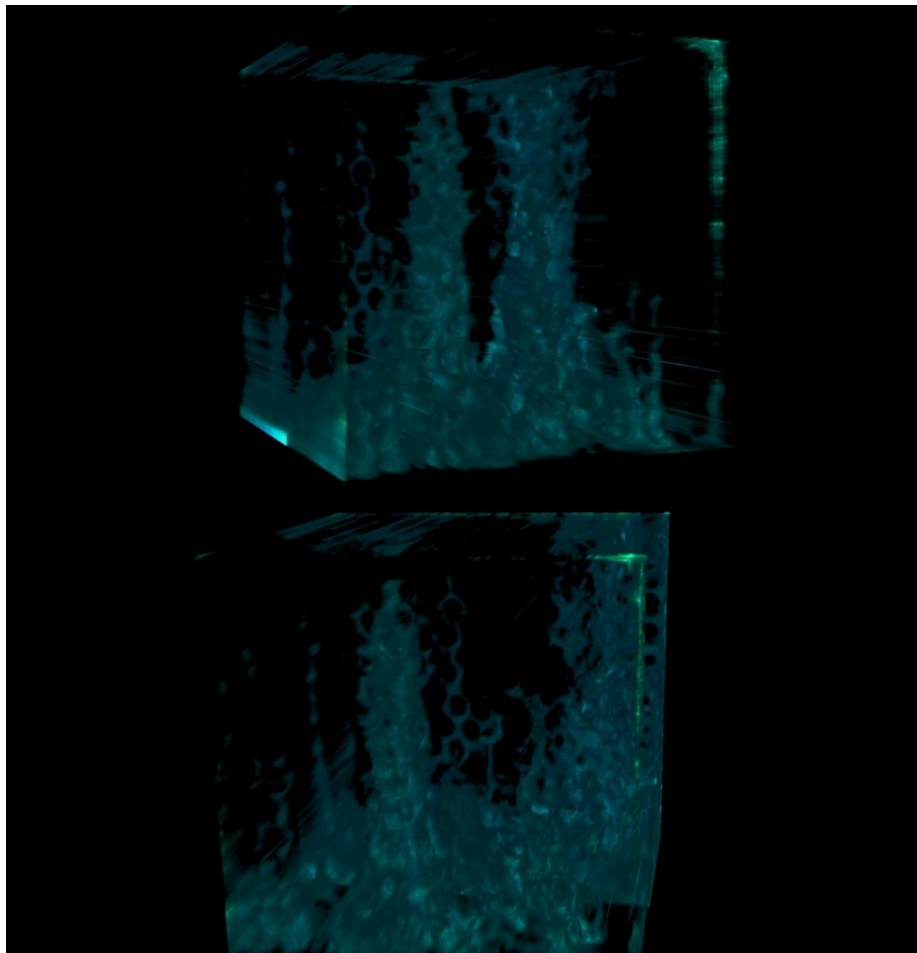


**Fig. 2.11—Solvent 2 (blue) diffusion at 490 min in the 5 cm model in 3-D from different angles. 3-D image was generated from 2-D photos and rotated.**

What was not observed in 2-D models by Hatiboglu and Babadagli (2008), however, was the behaviour of the front in the 3<sup>rd</sup> dimension. As seen in **Figure 2.6**, the height of the front (left image) is lower than those of 1 cm (middle image) and 2 cm (right image) deeper images. Thus, in x- and y-directions (width and length of the model) the front progress in a different manner. This opens a discussion on “bullet shape” frontal progress in a more realistic 3-D environment.

**2.4.3 Injection of solvent-2 into VAPEX model at the injection rate of 1 ml/min.** Most of the solvent chamber was dome-shaped, especially near the injection point, except for the tail of the injector due to low pressure (left images of **Fig. 2.12**). In spite of this, the chamber raised to the top at almost the same time (50 min located at 7 cm, and 60 min located at 19 cm) likely due to high permeability. Then, it spread along the top surface and displaced the denser oil downward. Thus, different chamber growth patterns were observed at different distances through the injector well (**Fig. 2.13**) and the differences in the patterns were consistent until the end of experiment (**Fig. 2.14**).

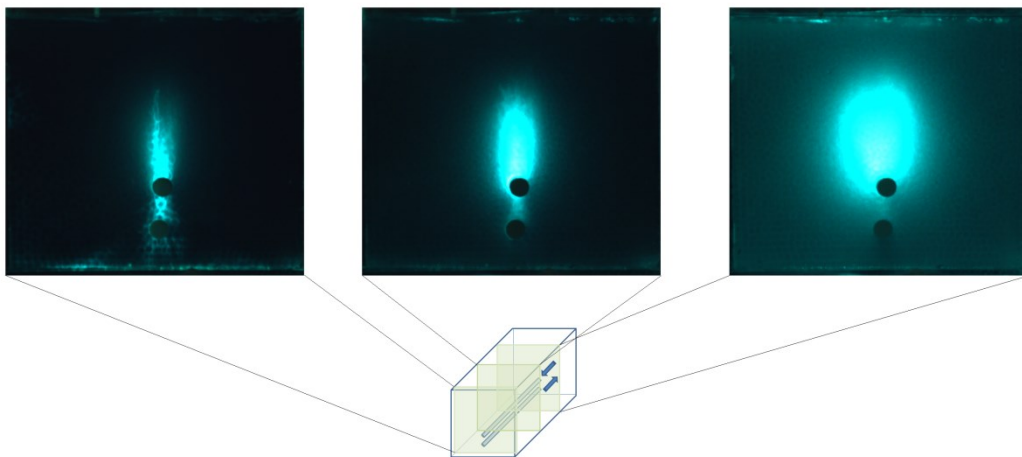


**Fig. 2.12—Solvent 2 (blue) injection in VAPEX model at 32 min with injection rate of 1 ml/min: 19 cm (left), 14 cm (middle), 7 cm (right) from the from injection port.**

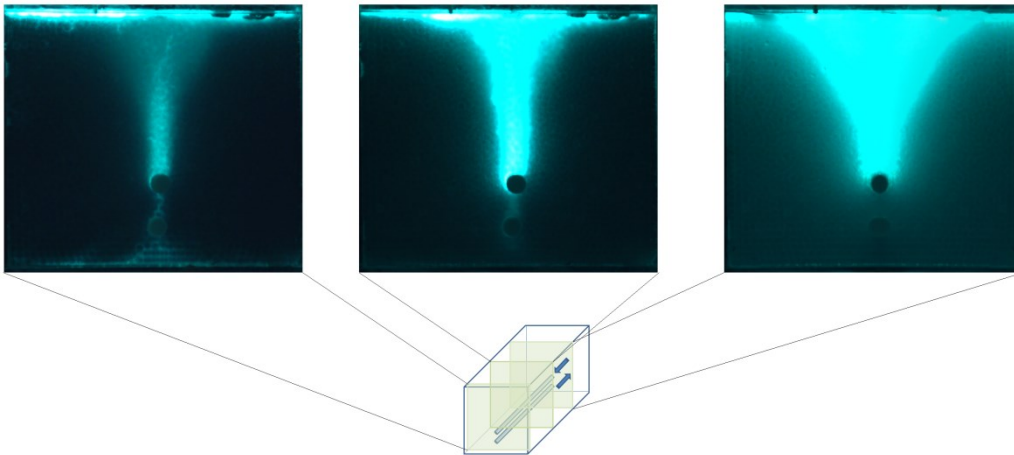


**Fig. 2.13—Solvent 2 (blue) injection in VAPEx model at 112 min with injection rate of 1 ml/min: 19 cm (left), 14 cm (middle), 7 cm (right) from the from injection port.**

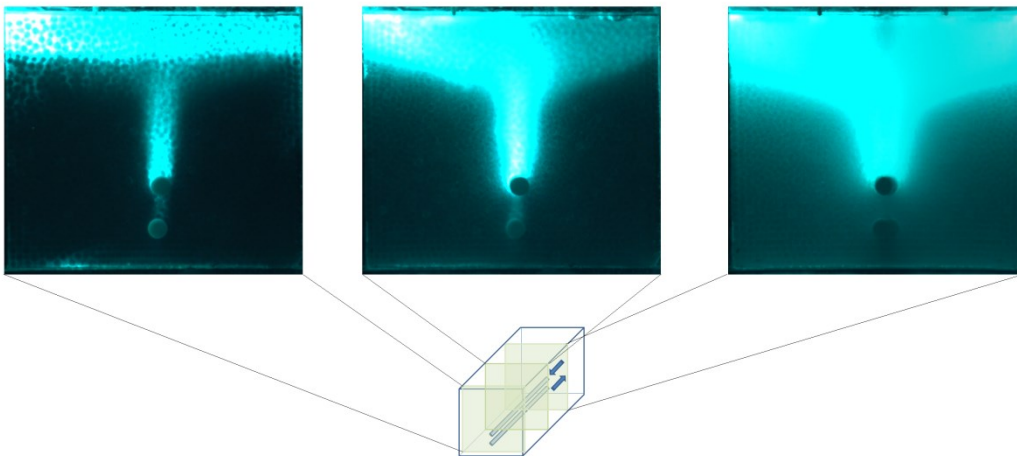


**Fig. 2.14—Solvent 2 (blue) injection in VAPEx model at 298 min with injection rate of 1 ml/min: 19 cm (left), 14 cm (middle), 7 cm (right) from the from injection port.**

The reason for this might be the same with diffusion boundary effect where the solvent tended to expand along the boundary instead of penetrating to the center of the model. It was widely accepted that the slope of the chamber would decrease when it had reached the top of the

reservoir. However, the slope did not change significantly except for the region where the bottom of solvent displaced from the top was contacted. It might differ for heavy oil and bitumen since the density and viscosity difference was small compared to field cases where the convective current at the top of the solvent chamber should be more significant and complex.

Due to the pressure loss along the injection tube, it was observed that the solvent chamber became smaller as the distance from the injection port increases. At the end of the well, the solvent chamber did not even form a dome-shape because the upward velocity was too low. Against the gravity effect, some solvent fell down to the bottom (left in **Figs. 2.12 through 2.14**) because the producer conducted the flow out of the model. The pressure along the production well was lower than that of the injector, which determines the flow direction by Darcy's law. However, a triangle-shaped solvent area below the producer was formed due to solvent diffusion. This was also observed in the experiment of solvent-1 diffusion where the solvent fingers were against the gravity effect due to density difference. The solvent front was wider when it touched the top surface. In this case, the solvent finger became wider once it had reached the bottom. As Ito and Ipek (2005) mentioned, viscous fingering did exist at the top of the solvent chamber in the images located at 19 cm and 14 cm in **Figure 2.12**.

**2.4.4 Injection of solvent-2 into VAPEX model at the injection rate of 1.5 ml/min.** Compared with the experiment with injection rate of 1 ml/min, the solvent chamber for 1.5 ml/min injection rate was wider with obvious fingering, and the size of the chamber was more uniform at higher injection rate. The solvent also reached the top around 60 min. However, it was the fingering that touched the top much earlier than the body of the solvent chamber. In **Fig. 2.15**, the chamber body was circled in red, and the other green area represented the fingering. From the side view (**Fig.**

2.2), it was observed that the solvent fingering rose cumbersomely but at the same height in average during the process. It was also observed that the solvent spread along the top surface and started to displace downward as similar to the lower injection rate case.

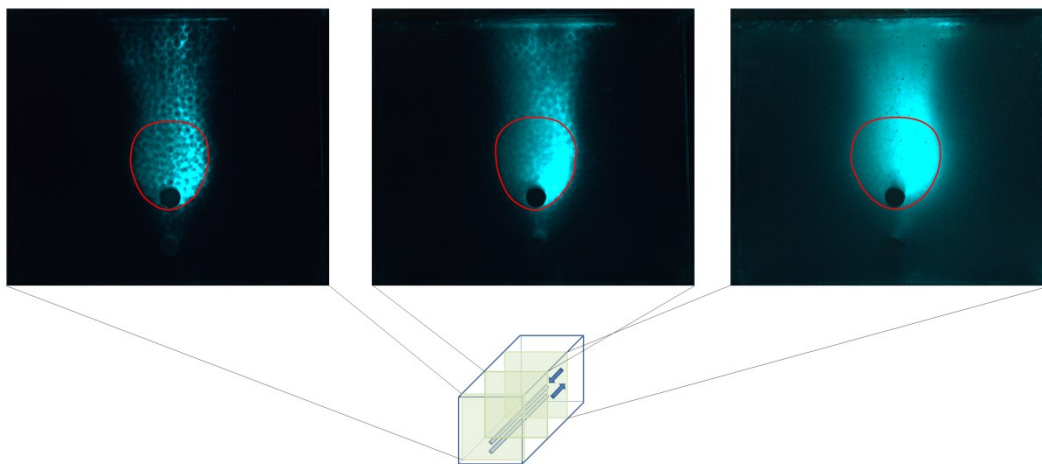


**Fig. 2.15—Solvent 2 (blue) injection in VAPEx model at 60 min with injection rate of 1.5 ml/min: 19 cm (left), 14 cm (middle), 7 cm (right) from the from injection port.**

The solvent chamber formed two sections at later stages: (1) the area from original solvent chamber close to the injector, and (2) the solvent displacing downward (Fig. 2.16 left). In the 1 ml/min injection rate case, the boundary was slightly tilted in part (2) (Fig. 2.14); while at injection rate of 1.5 ml/min, the slope decreased sharply and formed a concave upward shape (Fig. 2.16, indicated by red circles). The chamber reached at the top at similar time in both case. It can be predicted that if the injection rate is increased to a certain level, the wider section (1) and the steeper boundary of section (2) will have the same slope; hence the two parts are not distinguishable. The curvature of the oil/solvent mixing zone will increase the solvent/oil contact area, while linear boundary will decrease the area. To optimize the recovery, a maximum mixing area is expected by controlling the injection rate.

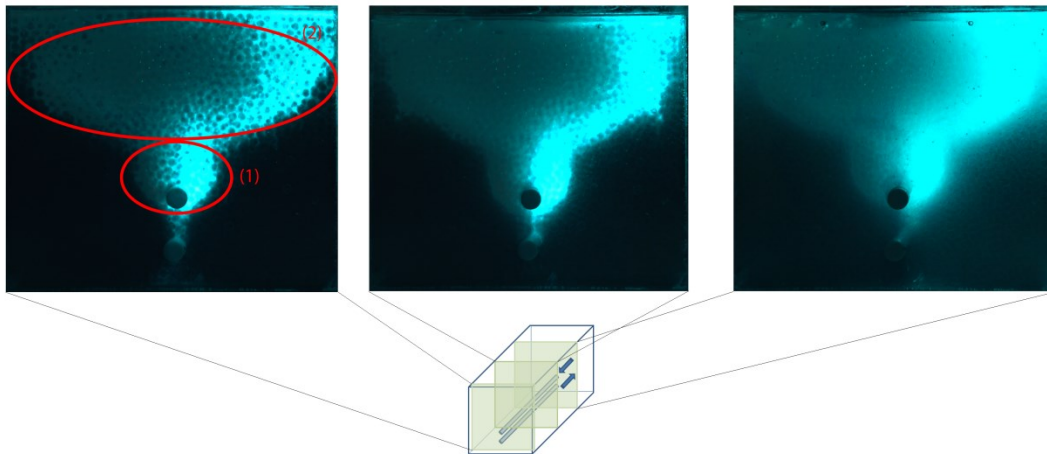


**Fig. 2.16—Solvent 2 (blue) injection in VAPEx model at 320 min with injection rate of 1.5 ml/min: 19 cm (left), 14 cm (middle), 7 cm (right) from the from injection port.**

**2.4.5 Limitations of the technique.** As stated in the “Experimental Set-Up” section, the scattering is a source of noise. Since the laser is scattered in the glass beads, the 1 mm thick laser sheet does not only excite the fluorescent dye within the 1 mm region, but also excite the fluorescence near the laser sheet by the reflected laser. Then, the surrounding fluorescence becomes the noise. On the other hand, cameras record the light emitted by the fluorescence transmitted though the transparent beads-oil-solvent media. For the same reason, the images are distorted due to the multi-reflection at the surface of glass beads. This is the reason why the images become fuzzy if it is deeper (from left to right in **Figs. 2.12- 2.16**), which limits the size (depth) of the model. This limitation depends on the number of glass beads and the concentration of fluorescent dye.

The energy of laser sheet decreases along the path in the beads-oil-solvent media due to absorption and energy used to excite the fluorescent dye. Therefore, the side further to the light source is darker (left in each image in **Figs. 2.15 and 2.16**). Hence, the brightness in the images does not represent the concentration of the solvent in this paper. However, for a model that is small

enough to consider a uniform laser intensity distribution at any location, the concentration can be found from the brightness.

Furthermore, to build 3-D images, the 2-D images are threshold and the dark areas are treated as oil and glass beads and removed from the images. Thus, the dark areas with unexcited fluorescence further to the laser source are removed by threshold. The result 3-D images show the bulk of solvent, but can hardly present the concentration or the falling oil. However, the motion of falling oil and raising solvent can be observed in the animation for each slice.

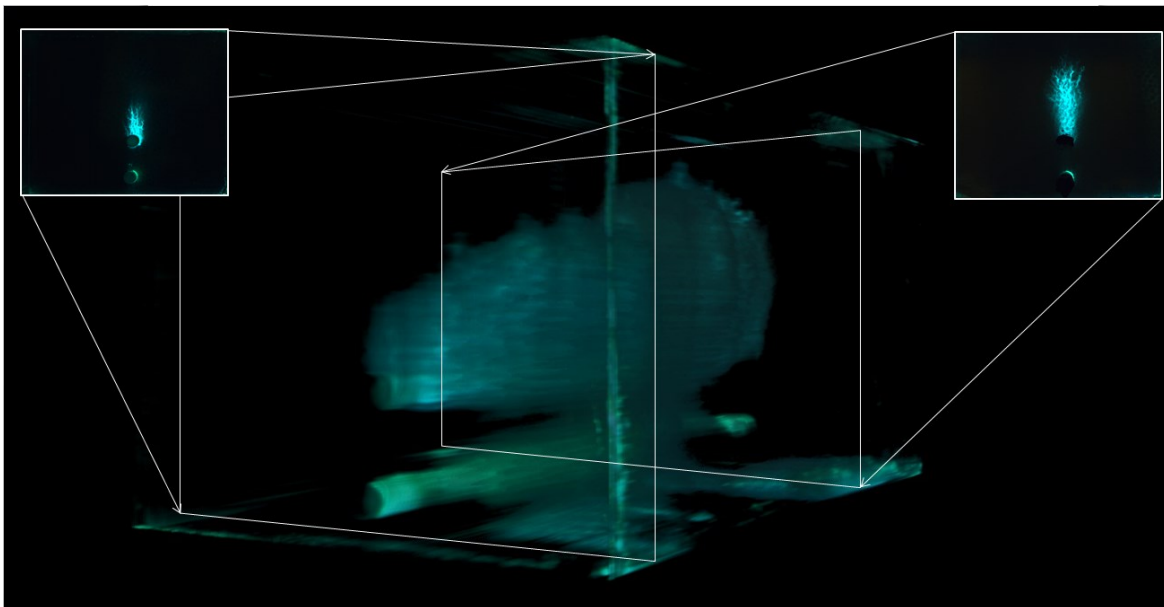


**Fig. 2.17—Solvent 2 (blue) injection in VAPEx model at 23 min with injection rate of 0.5 ml/min: 18 cm (left top), and 3.5 cm (right top) from the from injection port.**

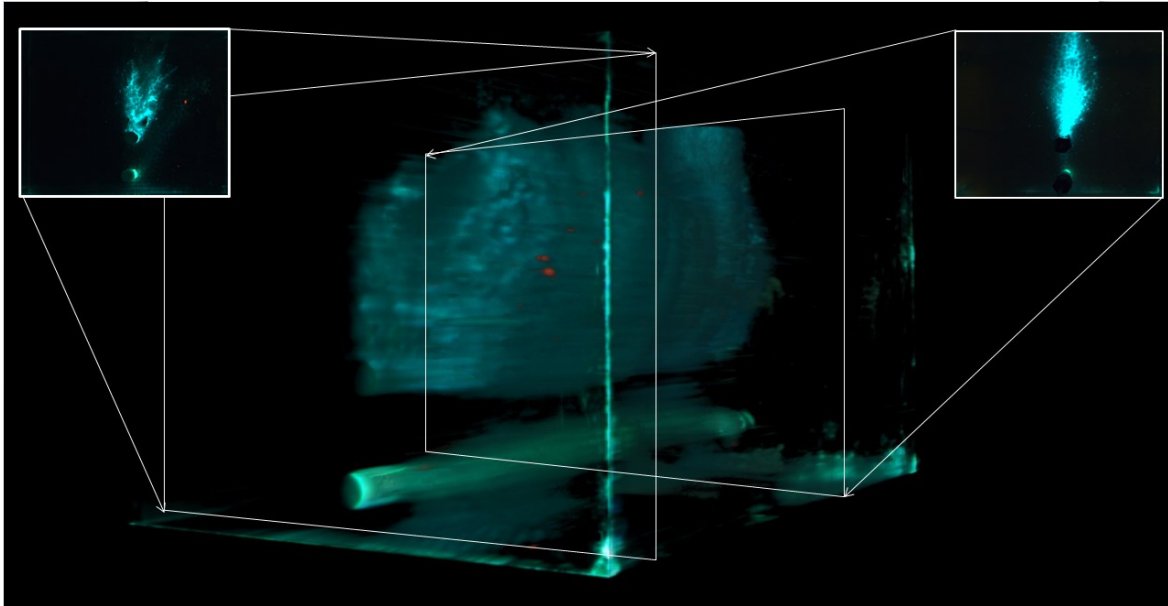


**Fig. 2.18—Solvent 2 (blue) injection in VAPEX model at 34 min with injection rate of 1 ml/min: 18 cm (left top), and 5 cm (right top) from the from injection port.**

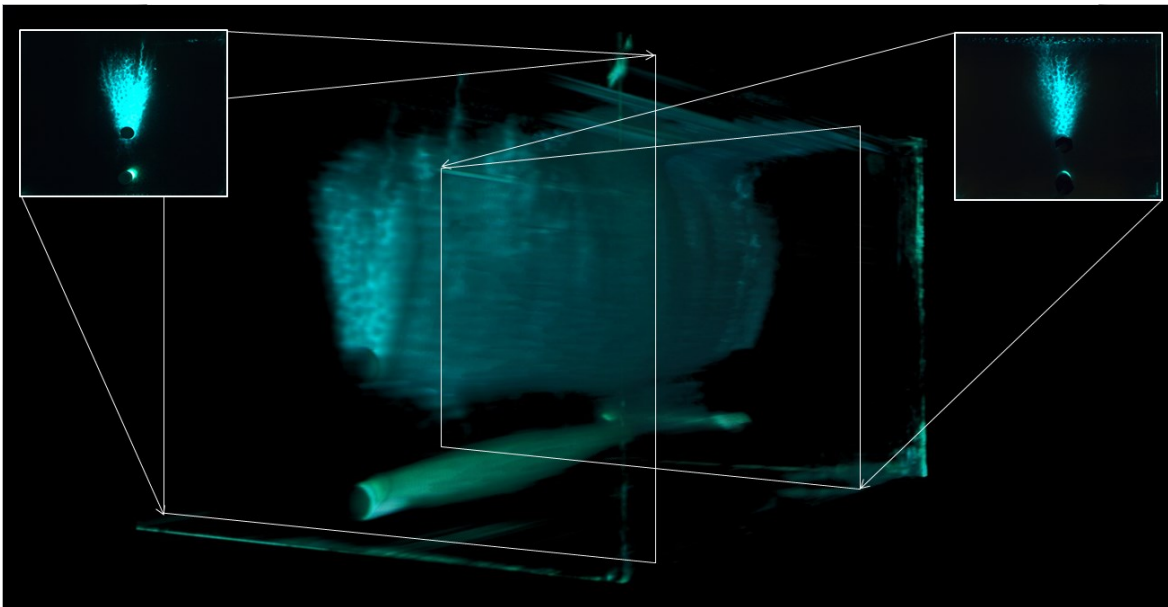


**Figure 2.19—Solvent 2 (blue) injection in VAPEX model at 22 min with injection rate of 1.5 ml/min: 18 cm (left top), and 3.5 cm (right top) from the from injection port.**

Despite these limitations, the images obtained were useful in analyzing the dynamics miscible flow processes in 3-D. Some examples with interpretations are included here covering different applications in the displacement in porous media. Further analysis of the VAPEX process using 3-D images obtained through the laser technique can be found in Fang and Babadagli (2014)

with additional discussion on the advantages of 3-D imaging of the experiments against 2-D models (Figs. 2.17-2.19). The dynamics of displacement front was captured against time in 3-D for sufficiently smaller time scale. Further attempts will be on the quantitative analysis of the diffusion controlled displacement process on a model given in Figure 2.4 (right side) using the images provided in Figs. 2.5 through 2.11. Note, however, that despite the positive factors, this type of experimentation is limited to certain viscosity ranges. The two phases (oil and solvent) and the solid part (glass beads) must have the same refractive index to obtain images (Table 2.3). This may result in certain density and viscosity values and the flexibility on the selection of these values are limited since the main factor is to maintain the same refractive index. As given in Table 2.3, we tried the widest density and viscosity ranges by mixing the oil and solvent phase with other chemical and further changes in this attempt requires rigorous efforts to find the possible chemical that gives larger density and viscosity differences, especially to model gravity dominated processes as well as displacement of heavy-oil.

## **2.5 Conclusions**

A 3-D visualization technique was applied to observe the solvent mixing/transport process with oil during pure diffusion (under static conditions) and convection (injection of solvents) conditions. The images generated were made distinguishable up to the center of the model, even for the largest one (15 x 20 x 15 cm), by adjustment of the refractive indices of the material used (oil, solvent, glass beads) and the selection of the proper dye added to solvent and further image processing. The size of model is strongly limited by scattering, multi-reflection and absorption of the laser. The 3-D images cannot present the difference in brightness inside the 3-D solvent volume.

In all diffusion models, the diffusion fronts tended to propagate near the edge of the model because of less resistance to flow. The viscous solvent took remarkably longer time to diffuse into the whole model and its viscous fingering was thinner compared to the low viscous solvent. To determine if this is dependent of density, viscosity or component, more solvent with different properties are needed. It was also observed that the diffusion front movement around the center of the model differed by increasing the size of the model. The showed a typical “bullet shape” type frontal progress.

The convective (VAPEX) model experiment showed that the solvent chamber was dome-shaped near to the injection point and its size decreased forming a vertical ellipse shape as the pressure along the injector decreased. However, no matter how narrow the chamber and how low the pressure, the top of the chamber arrived at the top about 1 hour for both injection rates. It was also found that there was viscous fingering at the top of the chamber, which was very outstanding at 1.5 ml/min injection rate. Fingering might be another reason why the solvent front raised at the similar rate. The solvent displaced the oil downward where the interface tilted more and even curved at higher injection.

## 2.6 References

- Alkindi, A.S., Al-Wahaibi, Y. M., Muggeridge, A. 2011. Experimental and Numerical Investigations into Oil-Drainage Rates during Vapor Extraction of Heavy Oils. *SPE J.* **16** (2): 343-357. <http://dx.doi.org/10.2118/141053-PA>.
- Butler R. and Morkys I.J. 1989. Solvent Analog Model of Steam-Assisted Gravity Drainage. *AOSTRA J Res* **5** (1):1-8. <http://dx.doi.org/10.2118/93-03-02>.
- Cessou1, A., Meier, U., and Stepowski, D. 2000. Applications of Planar Laser Induced Fluorescence in Turbulent Reacting Flows. *Meas. Sci. Technol.* **11**: 887. <http://dx.doi.org/10.1088/0957-0233/11/7/305>.
- Chao, Y.C., Han, J.M., and Jeng, M.S. 1990. A Quantitative Laser Sheet Image Processing Method for the Study of the Coherent Structure of a Circular Jet Flow. *Experiments in Fluids* **9**: 323-332. <http://dx.doi.org/10.1007/BF00188761>.

- Chen, J.D. and Wada, N. 1986. A New Technique for visualizing the Distribution of Oil, Water, and Quartz Grains in a Transparent, Three-Dimensional, Porous Medium. *SPE Form Eval* **1** (2):205-208. <http://dx.doi.org/10.2118/13349-PA>.
- Chen, B., Mikamib, F., Nishikawab, N. 2005. Experimental Studies on Transient Features of Natural Convection in Particles Suspensions. *International Journal of Heat and Mass Transfer*. **48** (14): 2933–2942. <http://dx.doi.org/10.1016/j.ijheatmasstransfer.2004.11.016>.
- Das, S.K. 1998. VAPEX: An Efficient Process for the Recovery of Heavy Oil and Bitumen. *SPE J.* **3**: 232-267. <http://dx.doi.org/10.2118/50941-PA>.
- Fang, F. and Babadagli, T. 2014. Three Dimensional Visualization of Solvent Chamber Growth in Solvent Injection Processes: An Experimental Approach. Paper IPTC 18115, presented at the Int. Petr. Tech. Conf. (IPTC), Kuala Lumpur, Malaysia, 10-12 Dec.
- Hatiboglu, C.U. and Babadagli, T. 2004. Experimental Analysis of Primary and Secondary Oil recovery from Matrix by Counter-Current Diffusion and Spontaneous Imbibition. SPE 90312 paper presented at the SPE Annual Technical Conference and Exhibition, Houston, TX, 26-29 September. <http://dx.doi.org/10.2118/90312-MS>.
- Hatiboglu, C.U. and Babadagli, T. 2005. Visualization Studies on Matrix- Fracture Transfer Due to Diffusion. Paper 2005-077 presented at the Canadian International Petroleum Conference, Calgary, Alberta, Canada, 7-9 June. <http://dx.doi.org/10.2118/2005-077>.
- Hatiboglu, C.U. and Babadagli, T. 2007a. Oil recovery by counter-current spontaneous imbibition: Effects of matrix shape factor, gravity, IFT, oil viscosity, wettability, and rock type. *J. Pet. Sci. and Eng.* **59** (1-2): 106-122. <http://dx.doi.org/10.1016/j.petrol.2007.03.005>.
- Hatiboglu, C.U. and Babadagli, T. 2007b. Lattice-Boltzmann Simulation of Solvent Diffusion into Oil-Saturated Porous Media. *Phys. Rev. E* **76**. <http://dx.doi.org/10.1103/PhysRevE.76.066309>.
- Hatiboglu, C.U. and Babadagli, T. 2008. Diffusion Mass Transfer in Miscible Oil Recovery: Visual Experiment and Simulation. *J Transport in Porous Media* **74** (2): 169-184. <http://dx.doi.org/10.1007/s11242-007-9189-1>.
- Hatiboglu, C.U. and Babadagli, T. 2010. Experimental and Visual Analysis of Co-and Counter-Current Spontaneous Imbibition for Different Viscosity Ratios, Interfacial Tensions, and Wettabilities. *J. Pet. Sci. and Eng.* **70** (3-4): 214-228. <http://dx.doi.org/10.1016/j.petrol.2009.11.013>.
- Heller, W. 1945. The Determination of Refractive Indices of Colloidal Particles by Means of a New Mixture Rule or from Measurements of Light Scattering. *Phys. Rev. E.* **68**: 5–10. <http://dx.doi.org/10.1103/PhysRev.68.5>.
- Hut, J., Omrane, A., Nygren, J, Kaminski, et al. 2002. Quantitative Three-Dimensional Imaging of Soot Volume Fraction in Turbulent Non-premixed Flames. *Experiments in Fluids* **33**: 265-269. <http://dx.doi.org/10.1007/s00348-002-0410-2>.
- Ito, Y. and Ipek, G. 2005. Steam-Fingering Phenomenon during SAGD Process. Paper SPE-97729 presented at the SPE International Thermal Operations and Heavy Oil Symposium, Calgary, Alberta, Canada, 1-3 November. <http://dx.doi.org/10.2118/97729-MS>.

- Mavko, G. and Nur, A. 1997. The Effect of a Percolation Threshold in the Kozeny-Carman Relation. *Geophysics* **62** (1480-1482). <http://dx.doi.org/10.1190/1.1444251>.
- Nygren, J., Richter, M. Alden, M., et al. 2002. Three-Dimensional Laser Induced Fluorescence of Fuel Distribution in an HCCI Engine. Proc., Combustion Institute, **29** (679–685). [http://dx.doi.org/10.1016/S1540-7489\(02\)80087-6](http://dx.doi.org/10.1016/S1540-7489(02)80087-6).
- Sakakibara, J., Adrian, R.J. 1999. Whole Field Measurement of Temperature in Water Using Two-Color Laser Induced Fluorescence. *Experiments in Fluids*. **26** (1-2): 7–15. <http://dx.doi.org/10.1007/s003480050260>.
- Sharma, P., Aswathi, P., Sane, A., et al. 2011. Three-Dimensional Real-Time Imaging of Bi-Phasic Flow through Porous Media. *Review of Scientific Instruments*, **82**. <http://dx.doi.org/10.1063/1.3658822>.
- Sutton, J. A., Fisher, B. T., Fleming, J. W. 2008. A Laser-Induced Fluorescence Measurement for Aqueous Fluid Flows with Improved Temperature Sensitivity. *Experiments in Fluids*. **45** (5): 869-881. <http://dx.doi.org/10.1007/s00348-008-0506-4>.
- Wiederseiner, S., Andreini, N., Epely-Chauvin, G., et al. 2001. Refractive-Index and Density Matching in Concentrated Particle Suspensions: A Review. *Experiments in Fluids* **50**: 1183-1206. <http://dx.doi.org/10.1007/s00348-010-0996-8>.

## **CHAPTER 3: Three Dimensional Visualization of Solvent Chamber Growth during the VAPEX Processes: An Experimental Approach Using Laser**

---

This paper is a modified and improved version of IPTC-18115-MS, which was presented at International Petroleum Technology Conference, 11 December, Kuala Lumpur, Malaysia. A version of this chapter has been submitted to a journal.

### 3.1 Preface

VAPEX is a non-thermal process proposed as an alternative to SAGD due to its applicability in thinner reservoirs, advantage of energy efficiency, produced oil quality, and environmental saving. Its high cost caused by the injected solvent, however, requires further efforts to optimize the process. This, in turn, entails a clear understanding of the physics of the process. To acquire this understanding, a 3-D visualization technique was applied to a VAPEX model packed with glass beads. The oil saturated porous media and the solvent injected into the model processed refractive indices matched with the glass beads, which made the model transparent. Laser illuminated the yellow fluorescent dye dissolved in the solvent to distinguish it from the oil. Two high-speed cameras recorded the process from two sides of the model while a laser sheet moved along the model.

A dome-shaped solvent chamber with viscous fingering on its top was observed. The injection pressure influenced the size of the chamber especially in the horizontal direction, which was not possible to identify through standard 2-D tests. Also, the solvent spread along the ceiling of the model and then displaced the oil down. The boundary of the solvent and oil was tilted and even curved at different injection rates. Finally, variable injection rate cases were compared with constant rate trials and an optimum operation plan was proposed through the analysis of the production rate, produced oil quality, and 3-D images of the chamber growth.

## 3.2 Introduction

With decreasing conventional oil reserves and the increasing demand of hydrocarbon fuels, huge resources of heavy oil and bitumen have received remarkable attention recently. In these resources, high oil viscosity is the greatest challenge faced, with two ways of tackling it: (1) Thermal processes that heat the reservoir oil and (2) dilution of the oil by solvent injection. SAGD (steam assisted gravity drainage) is one of the most successful thermal methods commercially applied for extra heavy-oil and bitumen recovery. Its non-thermal version, VAPEX (vapor extraction), was proposed for reservoir types where SAGD is not applicable, such as thin formations where heat loss could be a problem.

The VAPEX process works with the similar principle as SAGD. Two horizontal wells are drilled, one above the other in a reservoir where light hydrocarbons (named as the solvent) are injected through the upper well. The solvent with less density forms a dome-shaped chamber, rises gradually and mixes with the oil at the boundary of the chamber, which is called the mixing layer. The dissolved oil drains by gravity to the horizontal well located below the injector. In this process, the expensive solvent should be used optimally for an efficient application. An optimum design of solvent injection requires a clear understanding of the diffusion, dispersion, and chamber growth (i.e., sweep of oil by injected solvent) phenomena during the process.

Since VAPEX was introduced by Butler and Mokrys in 1991, a very limited number of visual studies have been performed to analyze the physics of the process. Hele-Shaw model and sand/bead packed cells were used as a reference to study the thickness of the mixing layer (Das and Butler 1998) and mass transfer (Das 1998). The chamber was assumed to be dome-shaped

with parabolic top (Butler and Mokrys, 1992) in theoretical analyses and circle in a number of numerical studies (Lin et al., 2014).

An analogy can also be made to the “sister” process to SAGD, where the process is controlled by heat transfer (thermal diffusivity) rather than mass transfer as in the VAPEX process. Despite a smooth interface, Ito and Ipek (2005) stated there could be fingering at the upper surface as observed in field scale SAGD applications (UTF Phase A and B) through their images obtained from numerical simulations matched with field data. Sasaki et al. (2001) showed images in a packed 2-D model with steam fingering, as well.

3-D visualization instead of 2-D models (Hele-Shaw or packed cells) is more reliable to avoid the boundary effect that is always presents in two parallel plate models. Also, having a process implemented through a horizontal well system makes the third dimension as crucially important. However, such a process is highly difficult to visualize in a 3-D environment. Devices like X-Ray or NMR are limited in the model size and image resolution. Data collection through probes to generate images is another possibility, but this may be destructive due to intrusion of sensor elements. This paper adapts the third option, which is the laser technique to visualize the VAPEX process in 3-D.

Chen and Wada (1986) introduced a laser assisted visualization technique to obtain the distribution of oil, water, and quartz in a transparent model. In this type of application, all three phases had to be refractive index (RI) matched such that the whole model is transparent. Fang and Babadagli (2014) prepared a model filled with glass beads before and after RI matching, as given in **Figure 3.1**. Because the RI of the fluids is basically lower than the solids, the materials acting as the porous media should have relatively low RI, such as polymethylmethacrylate

(PMMA), fused quartz, silica gel, and low index of refraction glass beads (Wiederseiner et al., 2011).

Recently, a real time 3-D imaging system of two phase flow in a small porous media cell was reported with movable laser sheet and a high speed camera (Sharma et al., 2011). This 3-D system has been used not only for liquid flows but also gas flow (Chao et al., 1990), fuel in engine (Nygren et al., 2002), and, even, flames (Hut et al. ,2002).

This paper is a continuation of our previous publications (Fang and Babadagli, 2014) where the initial results and images of VAPEX were introduced. Here, we generate more images and analyze them for clarifications on the physics of the VAPEX process and then propose an optimal injection design for an efficient application of the VAPEX process. The optimization is typically based on the duration of injection and injection pressure (or rate). However, the optimum operation pressure of VAPEX (and, even, SAGD) is controversial (Al-Bahlani and Babadagli, 2009). The driving force is gravity; hence, high pressure may not be necessary. Obviously, low pressure is more energy efficient, while injection pressure implies higher reservoir temperature, which leads to a preferable bitumen viscosity (Gates et al. 2005). However, Das (2005) simulated SAGD at low pressure and pointed out that there would be less sand and H<sub>2</sub>S contained in the production fluids due to low temperature. An economic SAGD project indicated by Butler and Yee (2002) for Imperial Oil SAGD pilot HWP1 started at reservoir pressure and after 2 years the pressure was kept at 1/5 – 1/4 of the initial pressure. Inspired from these studies on SAGD, in this paper, experiments were operated at constant pressures and variable pressures, as similar to Butler and Yee (2002).

### 3.3 Experimental Details

**3.3.1 Model.** A three dimensional VAPEX model filled densely with 4 mm diameter glass beads was in a dimension of 15 cm (width) x 20 cm (length) x 15 cm (height) with the lid placed 12 cm above the bottom. Thus, the effective size of the model was 15 cm (width) x 20 cm (length) x 12 cm (height) (Fig. 3.2). The producer was located 1.5 cm from the bottom of the model and the separation of the two wells was 3 cm. The wells were 20 cm long in total with a 1.5 cm joint to the injection tube and a 1 cm end cap. The injecting length was 17.5 cm (right image in Fig. 3.2).

**3.3.2 Refractive index matching.** In order to visualize and record the image in all positions during the VAPEX process, matching of the refractive indices (RI) is required for all three phases including the oil, solvent, and glass beads. When the materials in the model system have the same RI, the glass beads and the interface between the oil and solvent are invisible ( Fig. 3.1). The refractive indices of oil and solvent were adjusted to that of the glass beads because the RI of solids is fixed at the same temperature. Generally, liquids have a lower RI than solids. Thus, the RI of glass beads must be in a fluids-achievable range, which was 1.473 in this experiment. Fluids RI matching rules show that the RI of a mixture can be adjusted to a range between two refractive indices by mixing fluids with the two indices of refraction at certain concentration. Wiederseiner et al. (2001) summarized the numbers of mixing rules including Heller equation, Newton equation, Lichtenecker equation, Arago–Biot equation, Dale–Gladstone equation, Wiener equation, and Lorentz–Lorenz equation. Thus, it is difficult to choose one rule over another and thereby measuring the mixture RI every time before experiments is a necessity.

**Table 1** shows the materials that the oleic and solvent phases were mixed from. For visualization in 3-D, all the materials have to be transparent, thus the viscosities and, more critically, densities

are limited. Heavy mineral oil was chosen as the base of oleic phase and was diluted by adding about 14 vol% of heptane to reach the RI to 1.473. However, the viscosity of heavy mineral oil decreased sharply to around 45 cp due to dilution. Toluene, a high RI, low density, and viscosity fluid was chosen to increase the RI of the solvent phase. As toluene dissolves the materials used to create the wells and model, which are made of plastic, the concentration of toluene cannot be high. Therefore, the fluids mixed with toluene should have a RI lower but close to 1.473. To achieve this, light mineral oil was used. This resulted in the viscosity of solvent phase not significantly lower than the oleic phase (Table 2).

**3.3.3 Experimental set-up.** The experiment was operated in a dark room at room temperature with laser as light source. Due to the size of the model, a 445 nm wavelength 1.5 W high power laser can penetrate deep into the model. An expanded lens attached to the laser expanded the beam to a sheet, which illuminated a slice of solvent with yellow fluorescent dyes. A movable stage carried the laser along the model, and the laser sheet scanned the model when the stage was moving. Simultaneously, two high speed CCD cameras at opposite surface of the model took pictures perpendicularly to the laser sheet. When the stage moved every 1 mm, two synchronous pictures were taken by each camera. Once the whole model was scanned, the stage moved to the original position. The set-up is shown in Figure 3.3.

The filters located in front of the cameras blocked the blue laser and transmitted the yellow solvent color. In a picture, the bright fluid is the solvent, the dark area represents the oil, and the dark circles in the solvent region are the glass beads. Due to the size of the model and the small step size of the stage, one cycle took about 5 min. Then each scan was started every 10-13 min. The scan frequency was limited by the accuracy of the movable stage and took 2 sec to move 1

mm for each image. A higher scan speed can be reached with a mirror and lens system (Wiederseiner et al., 2001) for small models, but to apply this system to our model, a 28 cm diameter lens had to be used, which was difficult to handle. The technique is limited by the power of laser because as the laser penetrates into a material, its intensity decreases exponentially. Hence, the brightness of the solvent decreases and far deep in the model the solvent becomes difficult to distinguish. On the other hand, the background scatters the laser, especially when the laser intensity is high, which results in noise at brighter areas.

**3.3.4 Determination of injection rates.** Butler and Mokrys (1989) and Trivedi and Babadagli (2008) stated that the injection rate should be sufficiently low so that the gravity dominates the flow. Fayer et al. (1991) and Alkindi and Al-Wahaibi (2011) determined this by gravity-to-viscous ratio  $N_{g/v}$  for 2-D VAPEX model. For  $N_{g/v} > H/L$ , gravity dominates the flow, where:

$$N_{g/v} = \frac{\rho_o - \rho_s}{\mu_{ref} \left(1 - \frac{\mu_s}{\mu_o}\right) \gamma} kg \quad (1)$$

where  $\gamma = \frac{q}{H\phi y}$  is the horizontal velocity,  $q$  is the injection rate,  $H$  is the height of the beads pack,  $\phi$  is the porosity, and  $y$  is the length of the model. The permeability can be calculated from the Kozeny-Carman equation (Mavko and Nur, 1997):

$$k = \frac{\phi^3 d^2}{72(1 - \phi)^2 \tau^2} \quad (2)$$

where  $\phi$  is the porosity,  $\tau$  is the relative roughness, and  $d$  is the diameter of the glass beads.

As seen, the injection rate has to do with permeability and, thereby, glass bead size. However, limitations of the model exist such as the size of the glass beads and the maximum pressure (generated by injection) that the model can stand. Based on these restrictions, and in order to obtain a gravity-dominated flow regime based on Eq. 1, 4 mm diameter glass beads with a maximum injection rate of 1.5 ml/min were selected for solvent 1. Notice that due to a lack of physical (and visualization) experiments, formulae for scaled injection rate were not found for 3-D models. The length of the model “y” in the formula is the thickness of the 2-D model. The calculated rate only shows an approximate range of injection.

The experiments were conducted at constant and variable injection rates. For the constant injection rate experiments, the rate was kept at the maximum value that the model can handle to be in the gravity-dominated regime. For SAGD application, Collins (2007) suggested an operation method where the initial pressure is high until the steam chamber contacts the overburden. Considering this suggestion and the analogy between VAPEX and SAGD, a variable rate option was adapted and the solvent was injected at a high rate of 3 ml/min until the front of the solvent reached the top of the model. Then, the injection rate was switched to 0.5 ml/min when the chamber rose to the top. Another experiment starting at low injection rate (0.5 ml/min) followed by high injection rate of 3 ml/min after the chamber reached the top was also performed for comparison.

**3.3.5 Other experiment variables.** A list of all the experiment for this paper is given in Table 3. To study the heterogeneous reservoir effect, a low permeable zone filled with 1 mm diameter glass beads was inserted into the homogeneous model. The low permeable zone is 5 cm thick located in the middle (2 cm above the injector) and at the top of the model. The low permeable

zone was not placed at the bottom since the glass beads are small enough to fall into the injector and producer, and in industry, the well pairs are not usually drilled in low permeable zones due to low communication between wells. A thin mesh between the low and high permeability zones is used to prevent the beads from mixing together. The permeability is 70 Darcy for 1 mm glass bead porous media, significantly lower than that of the 4 mm diameter bead media (1120 Darcy). In both cases, the experiments were operated at 1.5 ml/min and 0.5 ml/min constantly.

A lighter solvent (solvent 2) with 0.830 g/cc density and viscosity less than 1 cp was introduced in an experiment. The maximum allowed injection rate was 5 ml/min, but in order to compare with previous solvent (solvent 1), 1.5 ml/min was selected.

### **3.4 Experimental Results and Analysis**

**3.4.1 Chamber size.** Generally, before the solvent front progressed to the top of the model, the chamber surface was rough at the top, dome-shaped at the higher part, and V-shaped at the lower part of the well. The width became narrower from the heel to the toe of the wells due to lower pressure and injection rate (from the right to the left images given in **Figs. 3.4 through 3.18**). Notice that in all 3D images, the chamber at 17.54 cm end suddenly got thinner due to the non-flow connector connecting the well and injection tube (right of **Fig. 3.2**) At 0.5 ml/min, due to the loss of pressure along the well, the upward velocity was so low that the chamber did not even form a dome shape at the end of the injection well. When the injection rate was increased from 0.5 ml/min to 3 ml/min in the variable rate experiment (started at 0.5 ml/min and increased to 3 ml/min after the solvent progressed to the top, **Fig. 3.19 through 3.22**), the chamber width expanded. This can be observed by comparing **Figures 3.20 and 3.21**, however, the chamber was still narrower than that of 1.5 ml/min. The chamber was slightly taller close to the injection point than that at

the tail of the injector. However, the difference was negligibly small, especially at the injection rate lower than 1.5 ml/min (gravity strongly dominates the flow) (Figs. 3.4–3.13). The difference in the width and height were more obvious at the higher injection rate (3 ml/min) (red triangles in Fig. 3.15). This resulted in the solvent fronts, located above the toe through the heel of the injector, reaching the ceiling almost simultaneously for the same injection rate. This shape trend was consistent until the end of the experiment.

Figure 3.23 shows the ratio of chamber maximum width over maximum height at the widest part (16.5 cm) at different times and injection rates before the chamber reached the top of the model. As the data points in the figure are all taken before the injection rate was adjusted, it can be treated as a constant rate injection of 0.5 ml/min, 1.5 ml/min, and 3 ml/min. The ratio decreases until 20 min, because initially the height approaches zero but the width equals to the width of the injector, which means the ratio approaches infinity when time was close to 0 min. The ratio increased later due to injection. As the width is a dependent of injection rate but height is almost independent of the rate, the ratio is lower at lower injection rates. During 3 ml/min injection the width was even greater than the height of chamber after 30 min. However, the difference was small when gravity strongly dominated the flow (less than 1.5 ml/min). This was more obvious by viewing the images than comparing the data of ratio.

The ratios of height (Fig. 3.24) at the toe (narrower) and the heel (wider) of the injector are all less than unity, which proves that the chamber size depends on the pressure distribution along the injector. The height ratio is time dependent due to the solvent flow rate in the injector. As the solvent enters the injector, it propagates in the cavity inside the tube with its front non-vertically (Fig. 3.25). As a result, even if the whole tube was injecting, the volume of the solvent, as well as

the pressure gradient, at each position is different. The curve will be stable until the solvent fully fills the injector when only pressure gradient affects the shape difference along the injector.

The solvent chamber of the highest injection at 3 ml/min rose the fastest as expected, but the time for all the rates to reach the top of the model differed slightly from each other. It took 47 min, 43 min, and 40 min for 0.5 ml/min, 1.5 ml/min, and 3 ml/min injection rates, respectively. It can be concluded that the chamber tended to grow horizontally instead of vertically. During the ramp-up phase, more solvent injection into the model led to higher sweep efficiency.

**3.4.2 Solvent flow between the wells.** Against the buoyancy, lighter solvent also sank to the production tube, possibly due to diffusion and pressure difference because pressure along the producer was lower than the injector (its lowest point is the production port close to the heel). Furthermore, as the injection point had the highest pressure, the pressure difference at this point was highest between the two wells, which led to faster downward solvent flow as observed in the 3-D images in **Figure 3.4** through 18. Cuthiell's et al. (2003) experiment with an injector located along the top edge and a producer located along the bottom edge of the model was a zoom of the communication between the wells. He also observed early solvent breakthrough near the injector later expanding along the well. In the areas where the solvent flowed through, the viscosity of oil decreased, which enabled the communication of the wells and improved the drainage of oil, and hence the recovery. (**Figs. 3.4-3.8 and 3.10-3.18**).

**3.4.3 Fingering phenomenon.** As shown by Ito and Ipek (2005), viscous fingering occurred at the top of the steam chamber, as also observed in 2-D sand pack experiment by Sasaki et al. (2001). Because the solvent chamber was narrow at low injection rates (0.5 ml/min), it was difficult to comment on fingering. From the images of higher rate experiments (1.5 ml/min and

3 ml/min in Figs. 3.9, 3.10, 3.14 and 3.15 where the red triangles indicate the chamber body, and the rough areas above them are due to solvent fingering), it can be seen that the fingering was significantly higher than the solvent chamber body. This is also the reason why the solvent front progressed to the top almost simultaneously. It was the viscous fingering that rose to the ceiling of the model first, not the solvent body.

**3.4.4 Downward displacement.** After the solvent front reached the top, it quickly spread along the ceiling of the model and displaced the denser oil down. At low injection rates, the interface between the solvent and the oil was almost horizontal and slightly tilted to the increasing chamber. When the injection rate increased to 1.5 ml/min, the slope of the interface became larger and curved downward near the region of raising solvent. At non-constant injection rate, during this stage, the injection rate was as low as 0.5 ml/min; however, the appearance was quite different with constant 0.5 ml/min injection. Two parts of the chamber are observed: (1) a very narrow part located near the injector, and (2) a wide part above this narrow part (Figs. 3.16-3.18). This change in width was very clear near the tail of the injection tube. Afterward, the solvent also spread under the ceiling of the model and the interface was even steeper than that of 1.5 ml/min injection; however, the boundary of solvent and oil curved in an upward, opposite direction (red curves in Fig. 3.17). The solvent chamber at ramp-up phase was so wide and close to the vertical wall of the model. Thus, the oil tended to drain along the inclined and curved chamber boundary rather than displacing downward. As evidence, at 0.5 ml/min initial injection, even though the width of the chamber increased, the change was not significant enough to change the curvature of downward displacing solvent/oil boundary. In summary, the downward displacement was strongly dependent on the initial injection rate. At the same time, the

diffusion boundary effect appeared along the model sides was observed, as seen in **Figures 3.17 and 3.18** (arrow directed to 17.5 cm).

**3.4.5 Production curves.** The concentration of oil in the produced fluid is plotted in **Figure 3.26**. When the injection rate was low at 0.5 ml/min, the produced fluid was observed with a high concentration of oil above 90% with relatively small variation. The curve did not show a trend. Since the low injection pressure resulted in a smaller pressure difference between the injector and producer, the solvent flowed between the tubes relatively slower. On the other hand, the higher injection rate built a low viscosity region between the wells. Hence, more solvent was produced. As mentioned in the downward displacement section, the downward displacement depended on the initial injection rate. Shown in **Figure 3.26**, there was no obvious change along the curve even if the injection rate increased from 0.5 ml/min to 3 ml/min. When the injection rate was increased to 1.5 ml/min, the produced fluid contained more solvent. Oil concentration dropped down until around 40 min when the highest point of the solvent chamber reached the top of the model. The curve showed quite erratic behavior from 70 min to 120 min, where the peak point appeared at 90 min when the ceiling of the model was covered by solvent. This was also observed from 57 to 90 min at 3 ml/min – 0.5 ml/min injection rates even though the solvent raise was faster and the erratic behavior was earlier. The oil production rate steadily dropped in the 3 ml/min – 0.5 ml/min experiment.

The total solvent oil ratio (SOR) was 1.059 and 1.130 with 0.5 ml/min and 1.5 ml/min injection rates. It was 1.0830 for the decreasing rate case (the injection started at 3 ml/min and reduced to 0.5 after the solvent chamber has reached the top), and 1.063 for the increasing rate case (the injection started at 0.5 ml/min and rose to 3 ml/min after the solvent front reached the top). The

high initial injection rate operation led to high sweep efficiency, while low constant and initial injection rate gave stable and high oil concentration. Both resulted in low cumulative solvent oil ratio (SOR). From this project's economic standpoint, 0.5 ml/min and both variable rate cases had similar SOR. However, in early times, high initial injection rate at 3 ml/min had a higher production rate (Fig. 3.27), which is more time-saving and economical.

**3.4.6 Comparison with 2-D models.** Das et al. (1998) and Butler et al. (1991) observed oil-solvent interface in a form of fingers in a Hele-Shaw cell, but the fingers layer did not appear in porous media packed models (Das and Butler, 1998; Das, 1998). Our 3-D VAPEX model did not show a fingers pattern at the interface either, instead, diffusion phenomenon was observed during the downward displacement phase. We also showed a raising solvent chamber above the wells and a slightly tilted downward displacement solvent layer at low injection rates, while the interface of downward displacement phase in 2-D was not distinguishable from the raising solvent chamber part. This means that the interface was almost straight (Das and Butler, 1998; Das, 1998). Their interface was similar with our high initial injection rate (3 ml/min – 0.5 ml/min) close to the injection point with higher pressure (17.5 cm image in Fig. 3.17). Due to -relatively-limited number of studies on the physics of the VAPEX process, one may take the SAGD studies as an analogy. The raising solvent chamber and solvent layer phenomenon were found similar to the low pressure ES-SAGD simulation (Ivory et al., 2008). The differences between our 3-D model and others' 2-D ones can be attributed to high injection pressure, which leads to straighter interfaces, and the low oil viscosity in our 3-D model (due to refractive index matching).

Another 2-D downward sweep experiment visualized the solvent displacement between two injection points representing two horizontal wells in the x-z plane (wells are located along the

top edge and the bottom edge of a model, Cuthiell's et al., 2003). This model only focused on the communication between the wells. It was found that the solvent breakthrough was first reached near the injection point and the solvent chamber spread in the y-direction also showing severe fingering. Decrease of pressure along the wells caused longer breakthrough time. These are in line with our observations in 3-D model but we were able to delineate the chamber growth and fingering in the third dimension (along a horizontal well) as a function of injection rate/pressure.

In 2-D visualization, the solvent chamber was observed in the direction perpendicular to the wells. In this view, a dome-shaped top and V-shaped bottom chambers were observed, but the change of solvent chamber shape and size cannot be interpreted. From the field experience, it is known that the solvent chamber was smaller further along the well, and it is necessary to keep the chamber size uniform to optimize the sweep efficiency especially at the tail of the well. From 3-D models, the width of the solvent chamber was found to be more dependent on the pressure. Thus, the low sweep efficiency due to pressure loss is caused by small horizontal expansion of the solvent chamber.

On the other hand, the boundary effect (the gap between two parallel plates of the 2-D) may play a significant role in solvent diffusion (Fang and Babadagli, 2014). For a 3-D model, this effect is negligible; the diffusion boundary effect only become effective close to the walls which is a significantly small space for a 15 cm x 20 cm x 15 cm model with the wells located in the middle (Fig. 3.1).

In a final attempt, a quantitative analysis was performed to indicate the limitations of 2-D models, taking advantage of 3-D visual data generated in the present study. To date, most of the efforts

were made on symmetrical 2-D approaches to analyze the physics of the process and to propose performance estimation models for VAPEX (or analog SAGD models using solvent approach) as mentioned earlier. We modified Monkrys and Butler's (1993) model of solvent chamber expansion in 2D Hele-Shaw cell to test it against our 3-D visual results. They used the following equation to calculate the solvent front progressing speed:

$$u = \frac{1 - c_s}{c_s} \frac{K}{\mu} \left( \frac{\partial P}{\partial y} - \Delta \rho g \right) \quad (3)$$

and the slope of the chamber top near the middle (small x):

$$m = \frac{1}{2(1 - c_{max}) \Delta \rho g x} \frac{\partial \phi}{\partial x} \quad (4)$$

where  $c_s$  is the solvent concentration at the solvent front,  $K$  is the permeability,  $\mu$  is the viscosity of oil,  $\frac{\partial P}{\partial y}$  is the pressure gradient in vertical direction,  $\frac{\partial \phi}{\partial x}$  is the potential gradient in horizontal direction,  $\Delta \rho$  is the density difference and  $g$  is the gravitational acceleration. The pressure gradient  $\frac{\partial P}{\partial y}$  is proportional to the pressure gradient around the injector. Therefore, with the same concentration of solvent, the height of solvent chamber is a factor of not only the pressure gradient but also the density difference of oil and solvent. Furthermore, the concentration of solvent is also a function of injection rate. It was also observed in the experiment that the rising velocity of solvent front is not directly related to the injection rate. While, as there is no gravity effect in horizontal direction, the slope around the middle of solvent front is directly proportional to the injection rate, which was seen that the top of chamber was more flat at a higher rate. If the

pressure gradient in the porous pipe representing the well is known, a better approach of chamber unitary along injector can be obtained.

By assuming linear regression at solvent front and injector one may assume that:

$$\left(\frac{\partial P}{\partial y}\right)_{\text{solvent front}} = (\beta Q_{inj})_{\text{injector}} \quad (5)$$

and:

$$\left(\frac{1 - c_s}{c_s}\right)_{\text{solvent front}} = \left(\alpha \frac{1 - c_s}{c_s}\right)_{\text{injector}} \quad (6)$$

Then, Equation 3 can be written as:

$$u = \alpha \frac{1 - c_s}{c_s} \frac{K}{\mu} (\beta Q_{inj} - \Delta \rho g) \quad (7)$$

in SI unit.

A matching with Monkrys and Butler's (1993) model to the experimental data obtained using the images given in the paper at the heel (16.5 cm), toe (1 cm), middle (8 cm) of the injector is shown in **Figure 3.28**. The parameters of  $\beta$  and  $\alpha \frac{(1-c_s)}{c_s}$  that yields the best match to the experimental data are shown in **Table 3.4**.  $\beta$  increases as the location further to the injection point, while  $\alpha \frac{(1-c_s)}{c_s}$  decreases. Increase in  $\beta$  indicates the pressure gradient drops along the injector. It is also agreed with **Figure 3.28** that the solvent front progress slower further to the injection point. Note that the above described model is linear and even though the slope of the straight lines

given for three different points throughout the well changes systematically (as well as the constants given in **Table 3.4**). The experimental data shown in **Figure 3.28** imply that further development of this type of analytical model approach is needed to capture the physics of the process. The analytical model gives perfect match to the experimental data obtained for the heel (16.5 cm) point. As seen, the effect of rate on the chamber growth is linear and the 2-D models are useful to describe the process at this point. At the middle (8 cm) and toe (1 cm) points, however, the experimental data do not show a perfect linear model and a deviation can be seen as one gets away from the heel, i.e., the injection point in our experiments representing the starting point of the horizontal section of the well. Further attempts can be made to capture this rate dependency effect on the analytical models.

**3.4.7 Heterogeneity.** Most of studies about heterogeneity impact on SAGD process with a negligible thickness of low permeability zone or non-permeable zone (shale) focused on the flow in the area other than this zone (Li et al., 2011 and Ravalec et al., 2009). Obviously, the steam will bypass the shale and raises from the edge. Few 2D visualization experiments with continuous/discontinuous low permeability layers done by Jiang and Butler (1996) showed the steam and solvent progress through the low and high permeability zones.

Similar with homogeneous model, when the solvent chamber touched the top of the high permeability zone in the 4 mm beads zone with well pairs, it quickly spread along the top boundary in this zone (**Fig. 3.29**). The trend of shape for different injection rates in uniform glass packed model was also observed in the 4 mm beads zone. For higher injection rate (**Figs. 3.29 and 3.30**), the chamber was wider compared with slower injection (**Fig. 3.31**). From the 2-D images (top) in **Figs. 3.30 through 3.32**, it was observed that the solvent front was also higher in the middle but

only slightly protruding compared with homogeneous model (Figs. 3.9 and 3.10), because the upward velocity in the low permeability zone was significantly lower than the horizontal speed at the top of the high permeability zone. For the same reason, when the solvent entered the high permeability zone, it quickly raised to the top of the model, cover the top of the zone and displace downward same as the uniform beads pack. At last, it could even fill this zone as presented by Jiang and Butler (1996). However, the solvent swept area in the low permeability zone was much higher than the top zone due to smaller pore size. Since there is not a significant advance in time for solvent reaching the interface of low and high permeability zones, the breakthrough point was not one (Fig. 3.34).

With the present of the low permeability zone, the time for solvent to reach the top of the model near the injection point was similar for all heterogeneous cases, around 70 - 80 min, while it took 90 min for 1.5 ml/min injection with low permeability zone at the top. When the low permeability zone was in the middle, the solvent top was still in the low permeability zone near the toe. Thus, low porosity reservoir is more injection rate sensitive.

**3.4.8 Lower viscosity and density solvent.** Solvent 2 with lower viscosity and density was injected into the uniform beads packed model. The mobility ratio for solvent 2 is higher than that of solvent 1. Therefore, it was difficult for the solvent to displace from the heel to the toe of the injector. This resulted in short injection (7.3 cm in Fig. 3.35) length along the injector. Due to low viscosity and density, the solvent rose to the top in 2 min, but the width of the solvent chamber kept almost the same through the experiment.

### **3.5 Conclusions and remarks**

A model with two horizontal tubes filled with glass beads was used to clarify the dynamics of the displacement process during VAPEX. A 3-D visualization technique using laser as the light source and CCD camera to record the images was applied to observe the process in the model. The system's set-up was able to visualize a model as large as 15 cm x 20 cm x 15 cm, but can only be applied to slow processes (like diffusion dominated displacement) as the scanning duration is long.

It was observed from the images that the solvent chamber was wider, taller, and dome-shaped when the injection pressure was high. Due to the pressure loss along the wells, the chamber became smaller in both horizontal and vertical directions but had less effect on the height. As the height was less dependent on pressure, the time for solvent to reach the top of the model was similar for the injection rates of 0.5 ml/min, 1.5 ml/min, and 3 ml/min. One of the reasons for this might be the fingering phenomenon, which progressed much faster than that of the solvent - chamber- body. At the same time, solvent also fell downward due to diffusion and the pressure difference between the wells. After the solvent had spread along the ceiling, it started to displace the oil downward, whose interface with oil tilted towards the rising solvent chamber in the middle. The shape of solvent boundary was found to be dependent on the initial injection rate. Diffusion boundary effect was found at the later stages of the variable rates case, which started at 3ml/min and followed by 0.5 ml/min.

Compared to 2-D model, a 3-D model showed not only the cross sectional view of a solvent chamber but also the change of solvent chamber shape and size along the injection-tube due to pressure loss. It also overcomes the capillary pressure of close placed parallel plates, and reduced

the effect of solvent boundary effect on the chamber growth and displacement. 3-D visualization was limited by the size of the model, the viscosity of the oil, the operation pressure and temperature. Notice that the gas (solvent vapor) refractive index is close to 1 which is almost impossible to find a solid (porous media) that can match with gas refractive index. Furthermore, the index of refraction is a variable with temperature. The experimental results shows an agreement with the theoretical model by Monkryns and Butler's (1993) by assuming linear relation between the injection rate and pressure gradient at the solvent front, oil-solvent concentration ratio around the injector and at the chamber top. However, as moved away from the heel (the injection point in our experiments) towards the toe, deviation from this model is clearly seen due to injection rate effect. This effect can be included in the analytical models as well as the rate dependent scaling relationships.

A low permeability layer in the middle of the model can be treated as a tight zone, while a low permeability layer at the top can represent not only a tight zone but also an overburden. It was concerned that the gap between the glass beads and the solid model lid causes the spread of solvent along the top of the model in a short period of time. But, it was approved that the lid behaved just an extreme case of tight layer (i.e., a boundary). The solvent still quickly spread below the low permeability zone with 1 mm glass beads layer (thigh zone) at the top. Flowing through the low permeability zone in the middle, the solvent chamber became wider and entered the high permeability zone through multiple points. It can also be concluded that the solvent chamber is less uniform in a tighter reservoir.

The phenomena of the extremely lighter and thinner solvent injection differ a lot from the thicker solvent case. The solvent rose much faster due to large density difference between the solvent

and oleic phase. For a constant injection rate, higher vertical speed led to a smaller chamber width. High mobility ratio made it difficult to displace the oil towards the injector. Hence, the injection area along the well is turned out to be shorter and covered only a portion of the well.

Due to refractive index matching, the viscosity of oleic phase is low as the viscosity decreases sharply if a fluid is mixed with another thin fluid. The experiment with less viscous oil still shows the uniform trend of the progressing speed of the solvent chamber. Butler (1985) has presented dimensionless numbers of length, area and flowrate, but the dimensionless flow rate cannot be applied to the lab scale as it resulted in a 3888.6 bbl/day or 429300 ml/min which obviously is not fit in the lab scale. Thus, the rate used in this paper only satisfies the condition that the gravity dominates the flow (**Eq.1**).

### 3.6 References

- Al-Bahlani, A.M. and Babadagli, T. 2009. SAGD Laboratory Experimental and Numerical Simulation Studies: A Review of Current Status and Future Issues. *J. Petr. Sci. and Eng.* **68** (3–4): 135–150. <http://dx.doi.org/10.1016/j.petrol.2009.06.011>.
- Alkindi, A. S. and Al-Wahaibi, Y. M. 2011. Experimental and Numerical Investigations into Oil-Drainage Rates during Vapor Extraction of Heavy Oils. *SPE J.* **16** (2): 343–357. <http://dx.doi.org/10.2118/141053-PA>.
- Butler, R. and Morkys I.J. 1989. Solvent Analog Model of Steam-Assisted Gravity Drainage. *AOSTRA J Res* **5** (1): 1–8. <http://dx.doi.org/10.2118/93-03-02>.
- Butler, R. M. and Morkys, I. J. 1991. A New Process (VAPEX) for Recovering Heavy Oils Using Hot Water and Hydrocarbon Vapour. *J. Cdn. Pet. Tech.* **30** (1).
- Butler, R. M. 1985. A New Approach to the Modelling of Steam-Assisted Gravity Drainage. *JCPT.* **24** (03). <http://dx.doi.org/10.2118/85-03-01>.
- Butler, A. M. and Morkys, I. J. 1992. Recovery Of Heavy Oils Using Vaporized Hydrocarbon Solvents: Further Development Of The Vapex Process. Paper SS-92-7 presented at Technical Meeting/Petroleum Conference of The South Saskatchewan Section, Regina, Saskatchewan, Canada, 7 - 9 October. <http://dx.doi.org/10.2118/SS-92-7>.
- Butler, R. M. and Yee, C. T. 2002. Progress in the In Situ Recovery of Heavy Oils and Bitumen. *JCPT.* **41** (1). <http://dx.doi.org/10.2118/02-01-02>.
- Chao, Y. C., Han, J. M., and Jeng, M. S. 1990. A Quantitative Laser Sheet Image Processing Method for the Study of the Coherent Structure of a Circular Jet Flow. *Experiments in Fluids* **9**: 323-332. <http://dx.doi.org/10.1007/BF00188761>.
- Chen, J. D. and Wada, N.1986. A New Technique for visualizing the Distribution of Oil, Water,

- and Quartz Grains in a Transparent, Three-Dimensional, Porous Medium. *SPE Form Eval* **1** (2):205-208. <http://dx.doi.org/10.2118/13349-PA>.
- Collins, P. M. 2007. The False Lucre of Low-Pressure SAGD. *JCPT* **46** (1). <http://dx.doi.org/10.2118/07-01-02>.
- Cuthiell, D., McCarthy, C., Frauenfeld, T., et al. 2003. Investigation of the VAPEX Process Using CT Scanning and Numerical Simulation. *JCPT* **42** (2). <http://dx.doi.org/10.2118/03-02-04>.
- Das, S. K. and Bulter, R. M. 1998. Mechanism of the Vapor Extraction Process for Heavy Oil and Bitumen. *Journal of Petroleum Science and Engineering* **21** (1-2): 43–59. [http://dx.doi.org/10.1016/S0920-4105\(98\)00002-3](http://dx.doi.org/10.1016/S0920-4105(98)00002-3).
- Das, S. 2005. Improving the Performance of SAGD. SPE-97921-MS presented at the SPE International Thermal Operations and Heavy Oil Symposium, Calgary, Alberta, Canada, 1-3 November. <http://dx.doi.org/10.2118/97921-MS>.
- Das, S. K. 1998. Vapex: An Efficient Process for the Recovery of Heavy Oil and Bitumen. *SPE J.* **3** (3): 232–237. <http://dx.doi.org/10.2118/50941-PA>.
- Fang, F. and Babadagli, T. 2014. Three Dimensional Visualization of Solvent Chamber Growth in Solvent Injection Processes: An Experimental Approach. SPE 170649 presented at SPE Annual Technical Conference & Exhibition, Amsterdam, Netherlands, 27 -30 October.
- Fayers, F.J. and Ann H.M. 1990. Extensions to Dietz Theory and Behavior of Gravity Tongues in Slightly Tilted Reservoirs. *SPE* **5** (4): 487–494. <http://dx.doi.org/10.2118/18438-PA>.
- Gates, I. D., Kenny, J., Hernandez-Hdez, I. L., et al. 2007. Steam Injection Strategy and Energetics of Steam-Assisted Gravity Drainage. *SPE Reservoir Evaluation & Engineering* **10** (1): 19 – 34. <http://dx.doi.org/10.2118/97742-PA>.
- Hut, J., Omrane, A., Nygren, J., et al. 2002. Quantitative Three-Dimensional Imaging of Soot Volume Fraction in Turbulent Non-premixed Flames. *Experiments in Fluids* **33**: 265-269. <http://dx.doi.org/10.1007/s00348-002-0410-2>.
- Ito, Y. and Ipek, G. 2005. Steam-Fingering Phenomenon During SAGD Process. Paper SPE-97729 presented at the SPE International Thermal Operations and Heavy Oil Symposium, Calgary, Alberta, Canada, 1-3 November. <http://dx.doi.org/10.2118/97729-MS>.
- Ivory, J. J., Zheng, R., Nasr, T. N., et al. 2008. Investigation of Low Pressure ES-SAGD. SPE-117759-MS presented at International Thermal Operations and Heavy Oil Symposium, Calgary, Alberta, Canada, 20-23 October. <http://dx.doi.org/10.2118/117759-MS>.
- Jiang, Q. and Butler, R. M., 1996. Experimental Studies on Effects of Reservoir Heterogeneity on the Vapex Process. *JCPT* **35** (10): 46-54. <http://dx.doi.org/10.2118/96-10-04>.
- Li, W., Mamora, D., Li, Y. and Qiu, F. 2011. Numerical Investigation of Potential Injection Strategies to Reduce Shale Barrier Impacts on SAGD Process. *JCPT* **50** (03): 57-64. <http://dx.doi.org/10.2118/133298-PA>.
- Lin, L., Zeng, F. and Gu, Y. 2014. A Circular Solvent Chamber Model for Simulating the VAPEX Heavy Oil Recovery Process. *Journal of Petroleum Science and Engineering* **118**: 27–39. <http://dx.doi.org/10.1016/j.petrol.2014.03.010>.
- Mavko, G. and Nur, A. 1997. The Effect of a Percolation Threshold in the Kozeny-Carman Relation. *Geophysics* **62**: 1480-1482. <http://dx.doi.org/10.1190/1.1444251>.
- Monkrys, I. J. and Butler, R. M., 1993. The Rise of Interfering Solvent Chambers: Solvent Analog Model of Steam-Assisted Gravity Drainage. *JCPT*, 26-36. <http://dx.doi.org/10.2118/93-03-02>
- Nygren, J., Richter, M. Alden, M., et al. 2002. Three-Dimensional Laser Induced Fluorescence of Fuel Distribution in an HCCI Engine. *Proc., Combustion Institute* **29**: 679–685.

- [http://dx.doi.org/10.1016/S1540-7489\(02\)80087-6](http://dx.doi.org/10.1016/S1540-7489(02)80087-6).
- Ravalec, M. L.; Morlot, C.; Marmier R. and Foulon, D. 2009. Heterogeneity Impact on SAGD Process Performance in Mobile Heavy Oil Reservoirs. *Oil & Gas Science and Technology – Rev. IFP* **64** (4): 469-476. <http://dx.doi.org/10.2516/ogst/2009014>.
- Sasaki, K.S., Akibayashi, N., Yazawa, Q.T., et al. 2001. Experimental Modeling of the SAGD Process-Enhancing SAGD Performance with Periodic Stimulation of the Horizontal Producer. *SPE Journal* **6** (01): 89–97. <http://dx.doi.org/10.2118/69742-PA>.
- Sharma, P., Aswathi, P., Sane, A., et al. 2011. Three-Dimensional Real-Time Imaging of Bi-Phasic Flow through Porous Media. *Rev. Sci. Instrum.* **82** (11). <http://dx.doi.org/10.1063/1.3658822>.
- Trivedi, J. and Babadagli, T. 2008. Efficiency of Diffusion Controlled Miscible Displacement in Fractured Porous Media. *Transport in Porous Media.* **71**(3): 379-394.
- Wiederseiner, S., Andreini, N., Epely-Chauvin, G., et al. 2001. Refractive-Index and Density Matching in Concentrated Particle Suspensions: A Review. *Experiments in Fluids* **50**: 1183–1206. <http://dx.doi.org/10.1007/s00348-010-0996-8>.

Refractive Index		
1	Heptane	1.386
2	Light Mineral Oil	1.469
3	Heavy Mineral Oil	1.483
4	Toluene	1.497

**Table 3.1—Refractive indices of original materials.**

		Refractive Index	Density g/cc	Viscosity cP
		±0.0003	±0.003	±5
Oleic Phase	Mixture 1 and 3	1.4730	0.866	45
Solvent Phase 1	Mixture 2 and 4	1.4730	0.857	23
Solvent Phase 2	Mixture 1 and 4	1.4730	0.830	< 1
Porous Media	Glass Beads	1.4730	-	-

**Table 3.2—Fluids used in the experiment after refractive index matching.**

No.	Solvent	Injection Rate (ml/min)	Homogeneous/Heterogeneous
1	1	1.5	Homogeneous
2	1	0.5	Homogeneous
3	1	3 followed by 0.5	Homogeneous
4	1	0.5 followed by 3	Homogeneous
5	1	1.5	Low permeable zone in the middle
6	1	0.5	Low permeable zone in the middle
7	1	1.5	Low permeable zone at the top
8	1	0.5	Low permeable zone at the top
9	2	1.5	Homogeneous

**Table 3.3—List of experiments.**

	$\beta$	$\beta$	$\alpha(1-c_s)/c_s$
	SI unit	$Q_{inj}$ in ml/min	SI unit
Heel (16.5 cm)	326510.6	0.00544	11.0107
Middle (8 cm)	637036294.2	10.6193	8.6828
Toe (1 cm)	829062665.6	13.8204	6.8137

**Table 3.4—Parameters for experimental and theoretical model matching.**

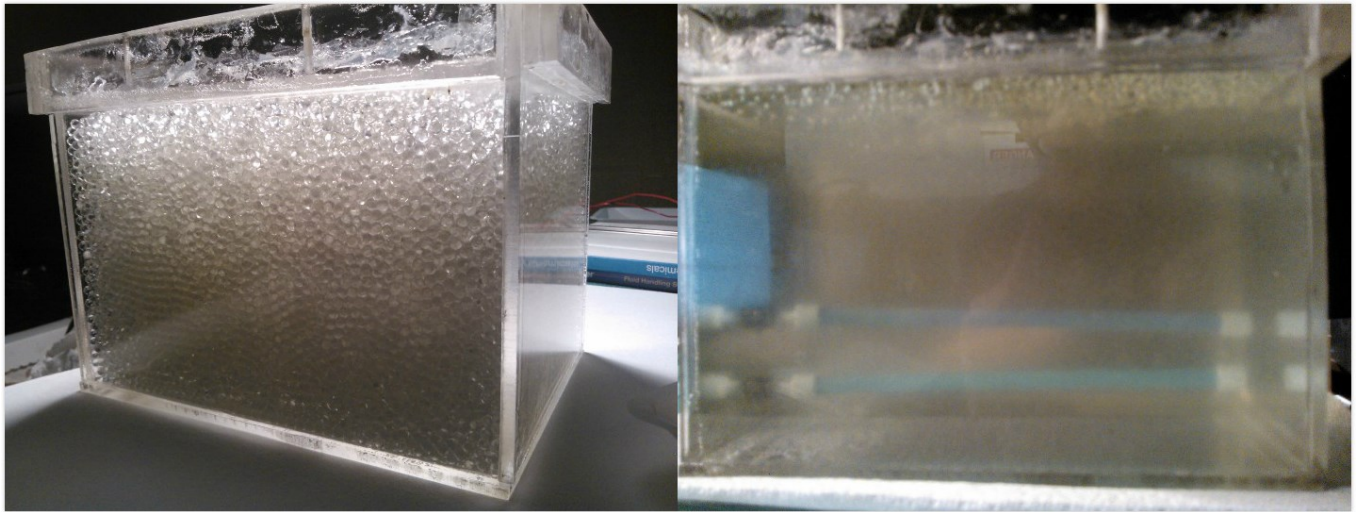


**Fig. 3.1—VAPEx model before (left) and after (right) refractive index matching (Fang and Babadagli, 2014).**

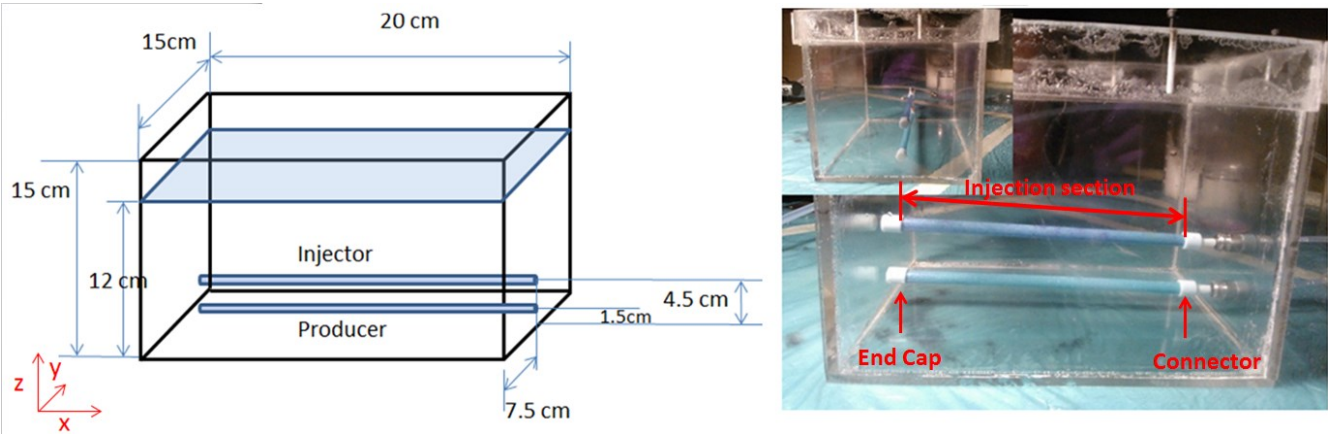


**Fig. 3.2—Dimensions of VAPEx model (Fang and Babadagli, 2014).**

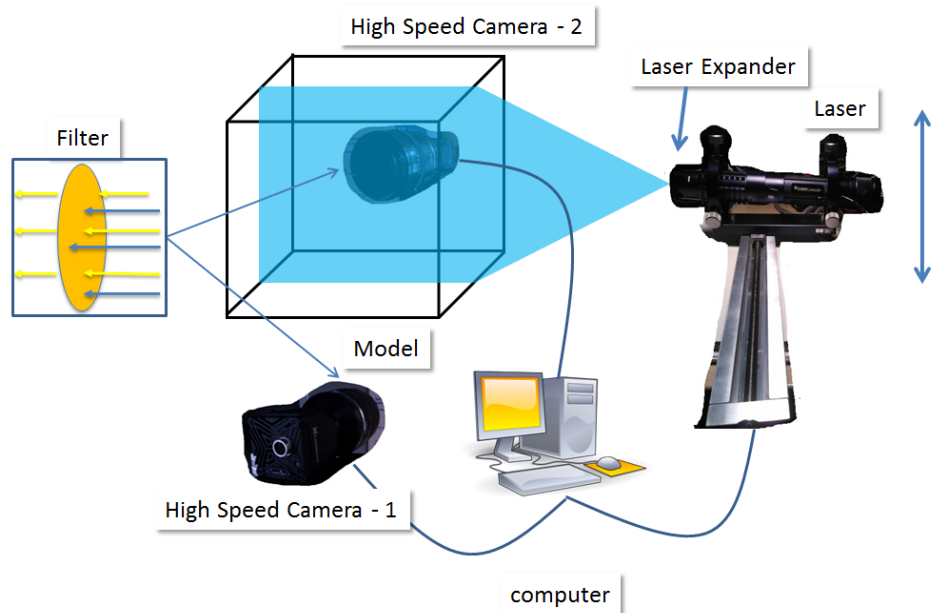


**Fig. 3.3— Laser imaging system set-up (Fang and Babadagli, 2014).**

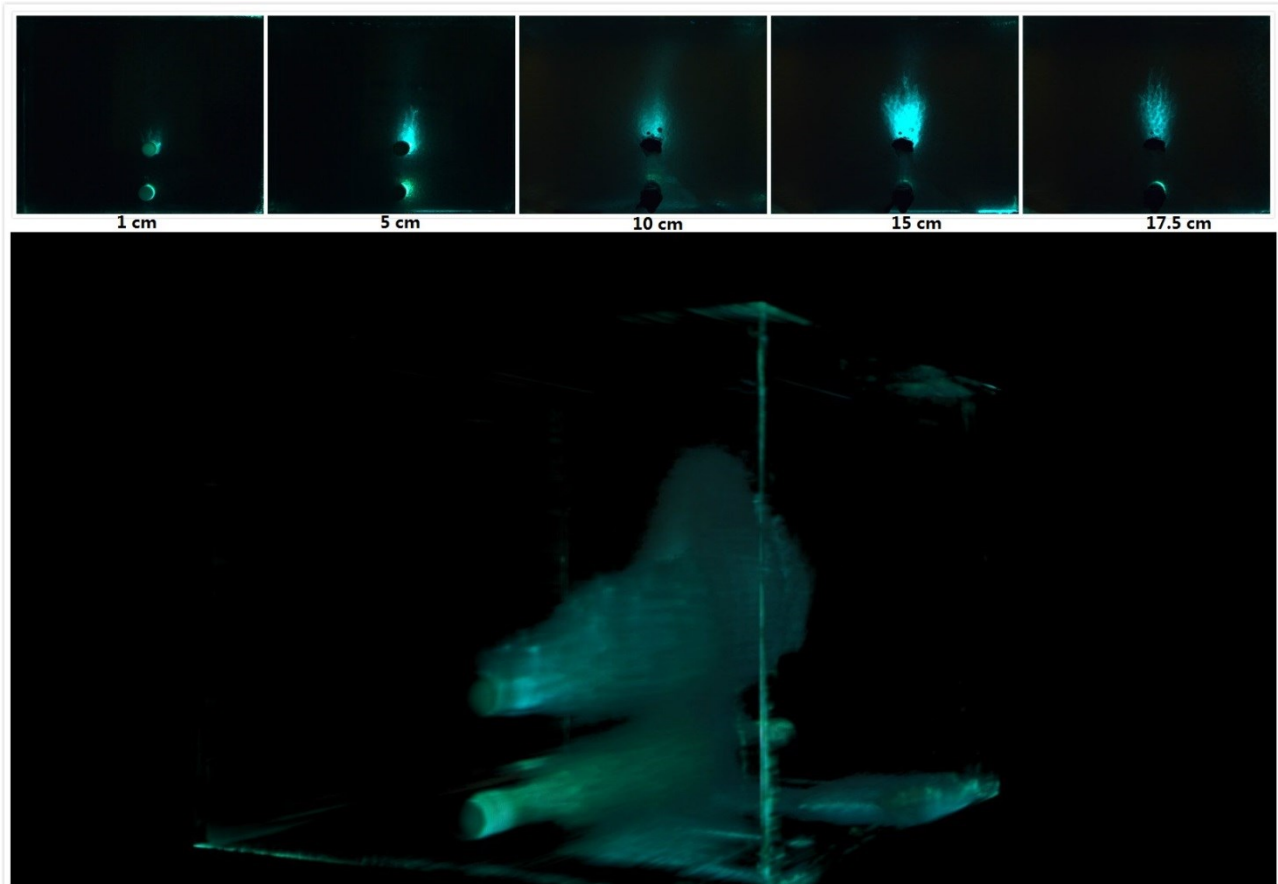


**Fig. 3.4—VAPEx injected at 0.5 ml/min at 1 cm, 5 cm, 10 cm, 15 cm, 17.5 cm and 3-D images from the toe at 12 min.**

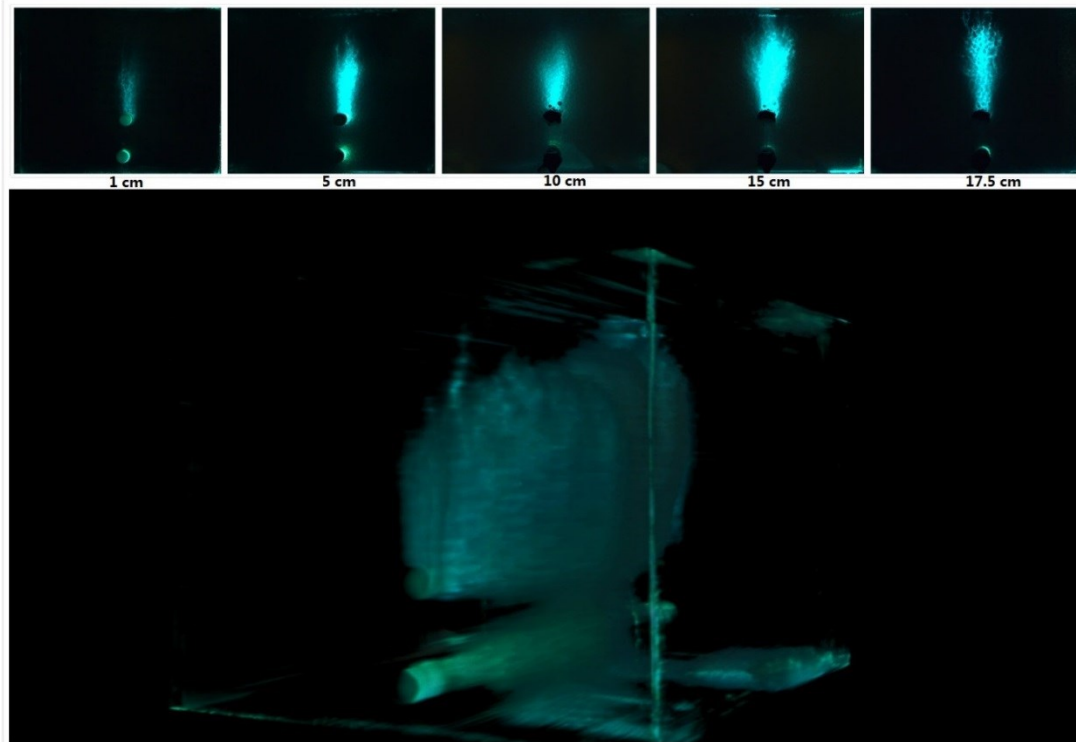


**Fig. 3.5—VAPEX injected at 0.5 ml/min at 1 cm, 5 cm, 10 cm, 15 cm, 17.5 cm and 3-D images from the toe at 35 min.**

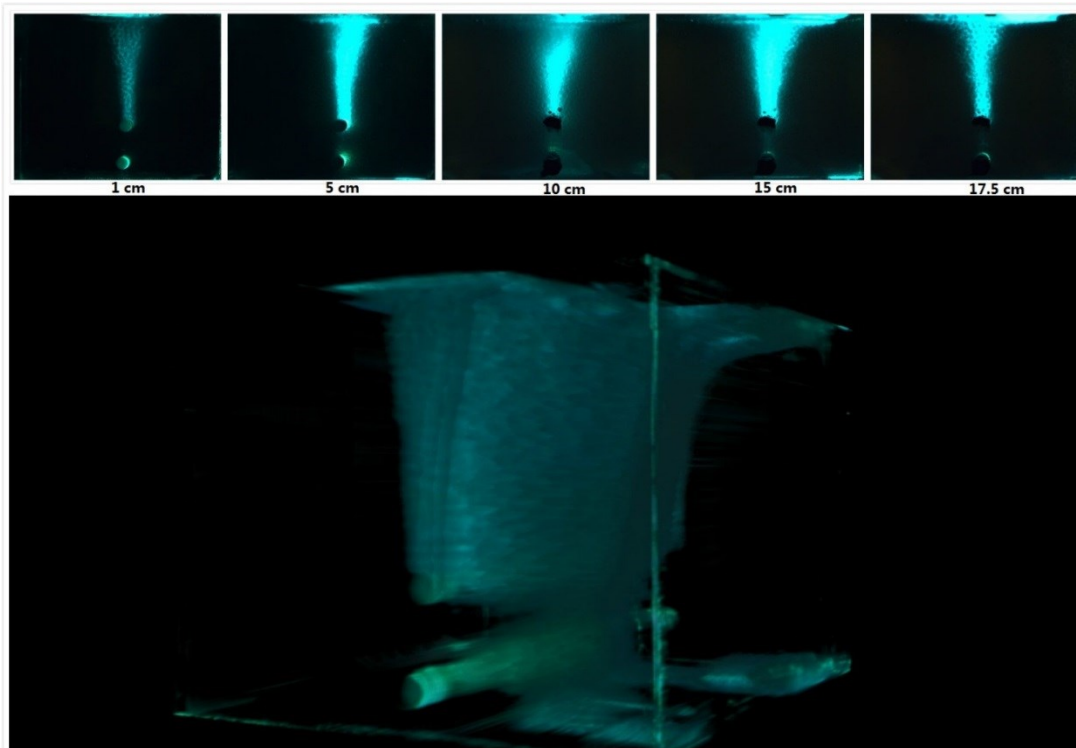


**Fig. 3.6—VAPEX injected at 0.5 ml/min at 1 cm, 5 cm, 10 cm, 15 cm, 17.5 cm and 3-D images from the toe at 78 min.**

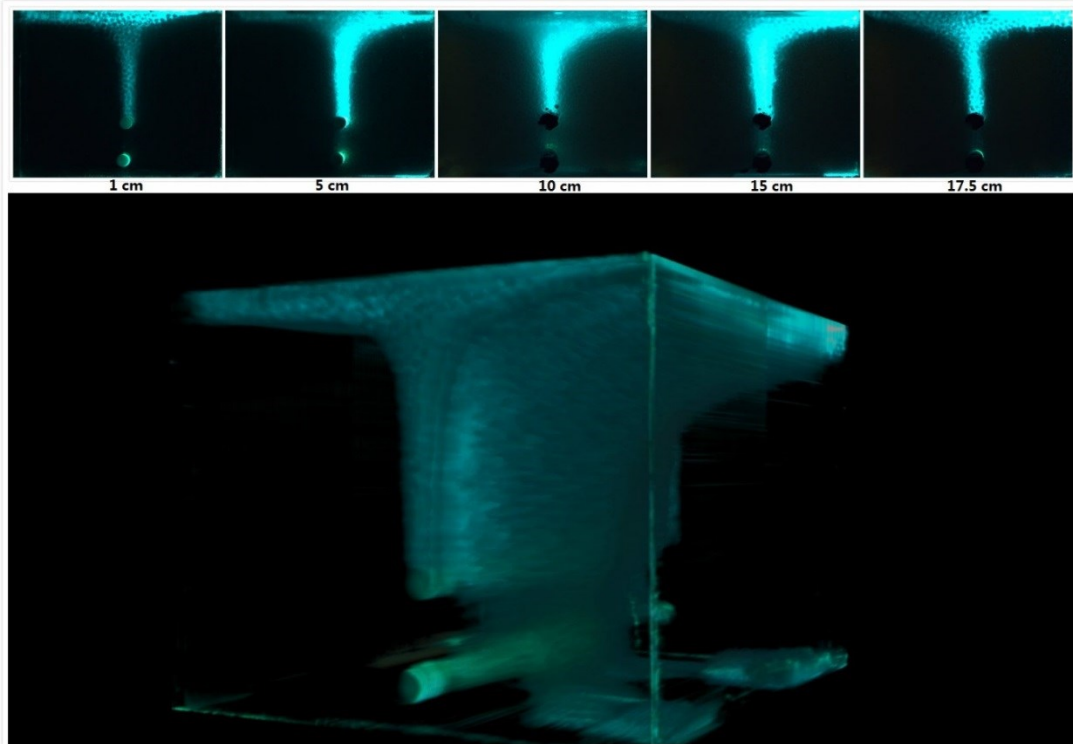


**Fig. 3.7—VAPEX injected at 0.5 ml/min at 1 cm, 5 cm, 10 cm, 15 cm, 17.5 cm and 3-D images from the toe at 153 min.**

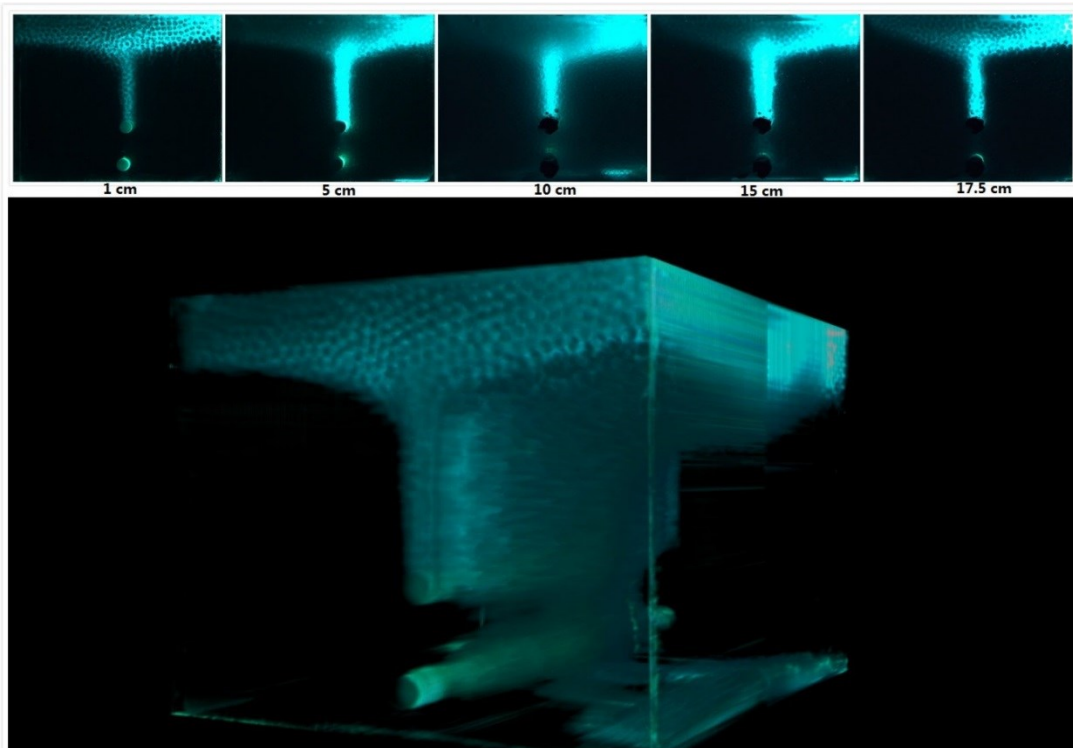


**Fig. 3.8—VAPEX injected at 0.5 ml/min at 1 cm, 5 cm, 10 cm, 15 cm, 17.5 cm and 3-D images from the toe at 318 min.**

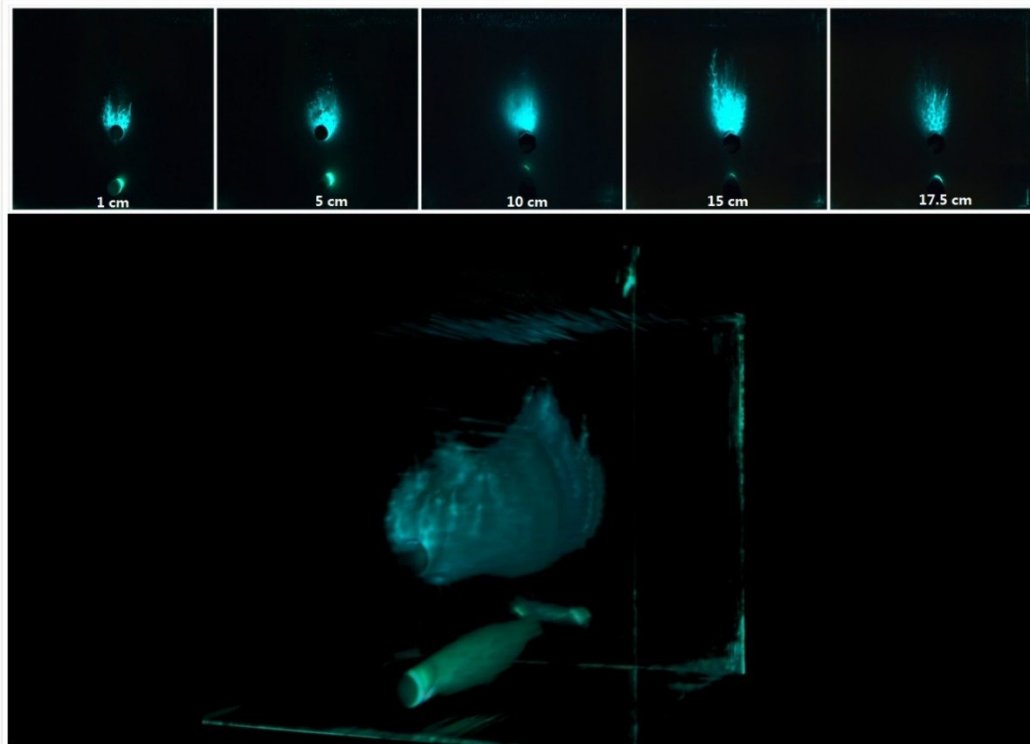


**Fig. 3.9—VAPEX injected at 1.5 ml/min at 1 cm, 5 cm, 10 cm, 15 cm, 17.5 cm and 3-D images from the toe at 12 min.**

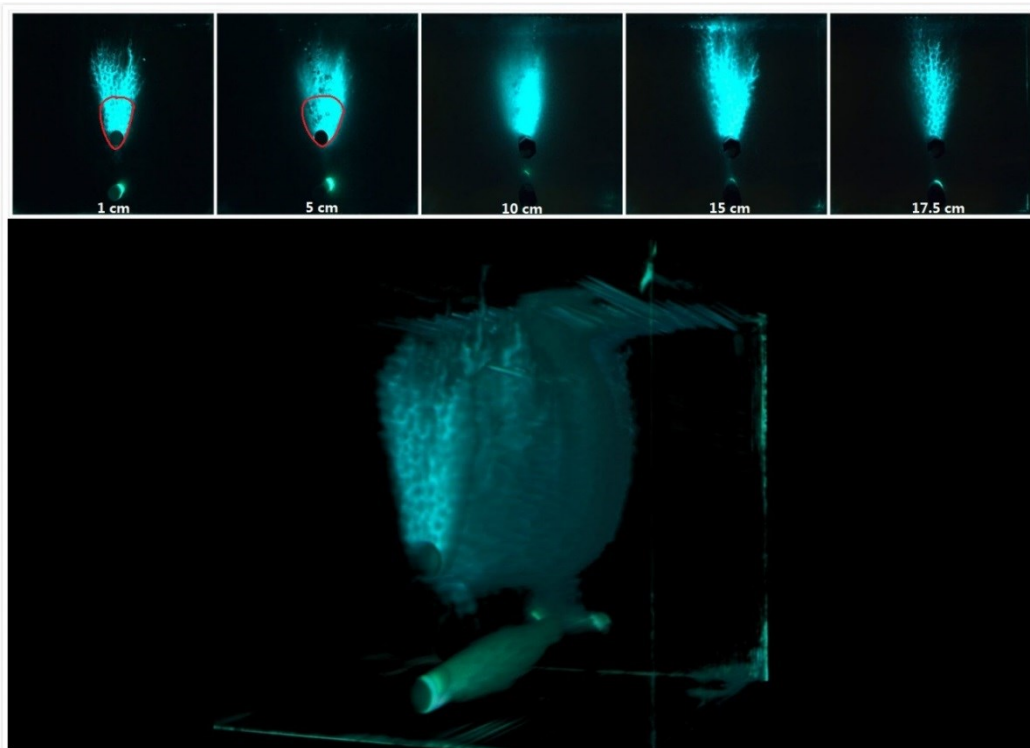


**Fig. 3.10—VAPEX injected at 1.5 ml/min at 1 cm, 5 cm, 10 cm, 15 cm, 17.5 cm and 3-D images from the toe at 34 min.**

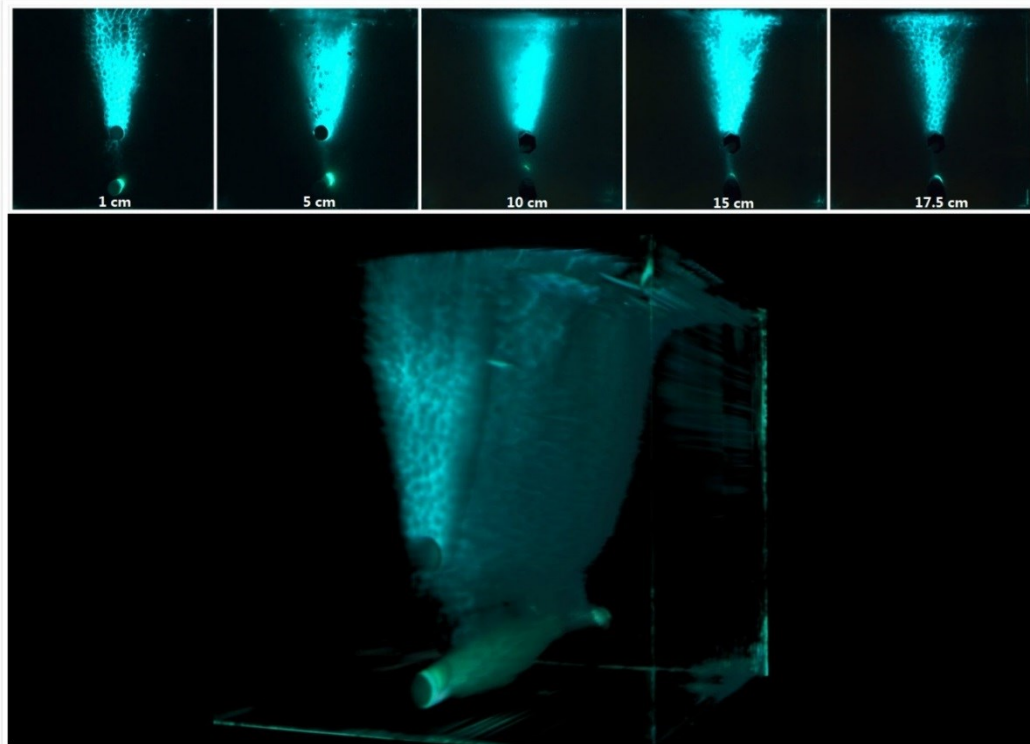


**Fig. 3.11—VAPeX injected at 1.5 ml/min at 1 cm, 5 cm, 10 cm, 15 cm, 17.5 cm and 3-D images from the toe at 59 min.**

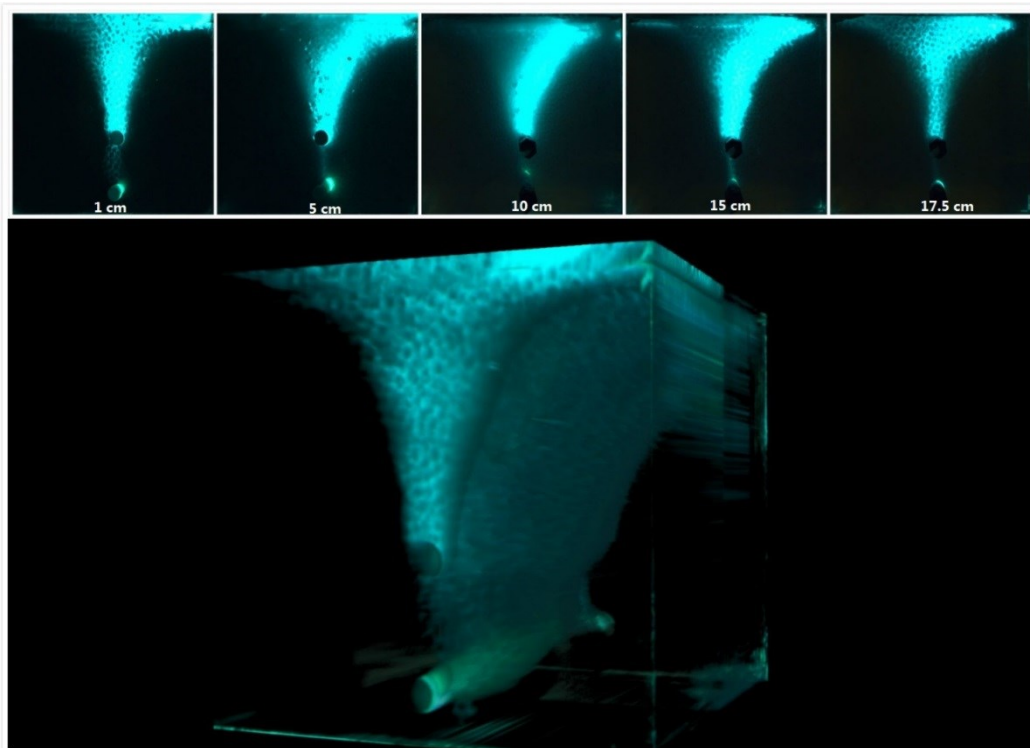


**Fig. 3.12—VAPeX injected at 1.5 ml/min at 1 cm, 5 cm, 10 cm, 15 cm, 17.5 cm and 3-D images from the toe at 98 min.**

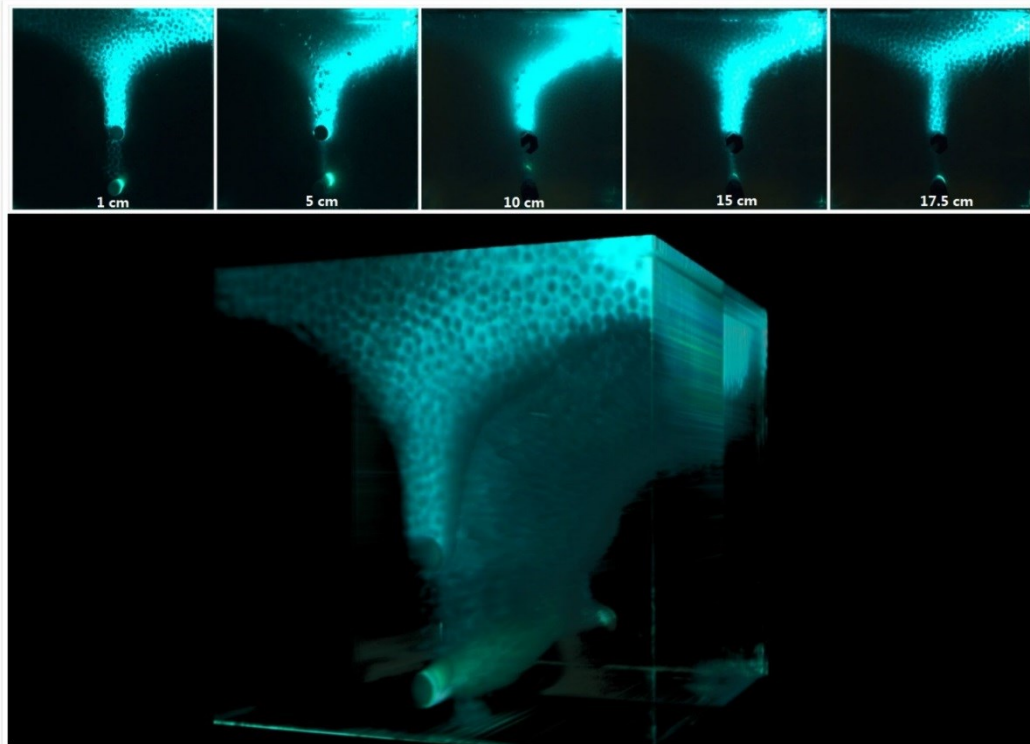


Fig. 3.13—VAPeX injected at 1.5 ml/min at 1 cm, 5 cm, 10 cm, 15 cm, 17.5 cm and 3-D images from the toe at 153 min.

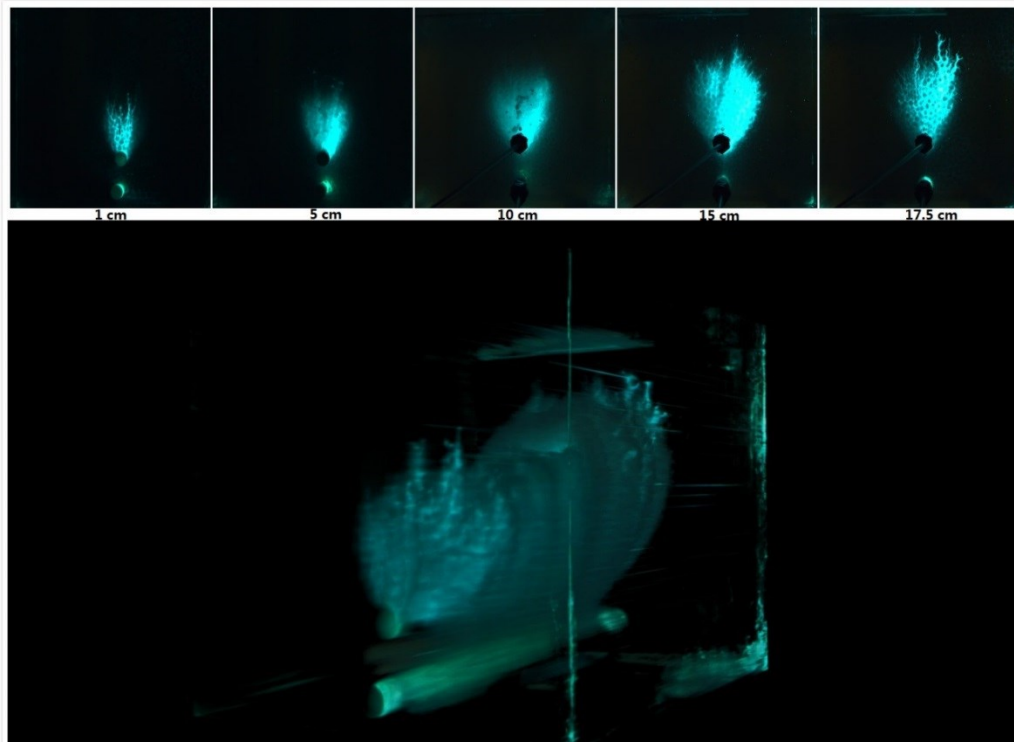
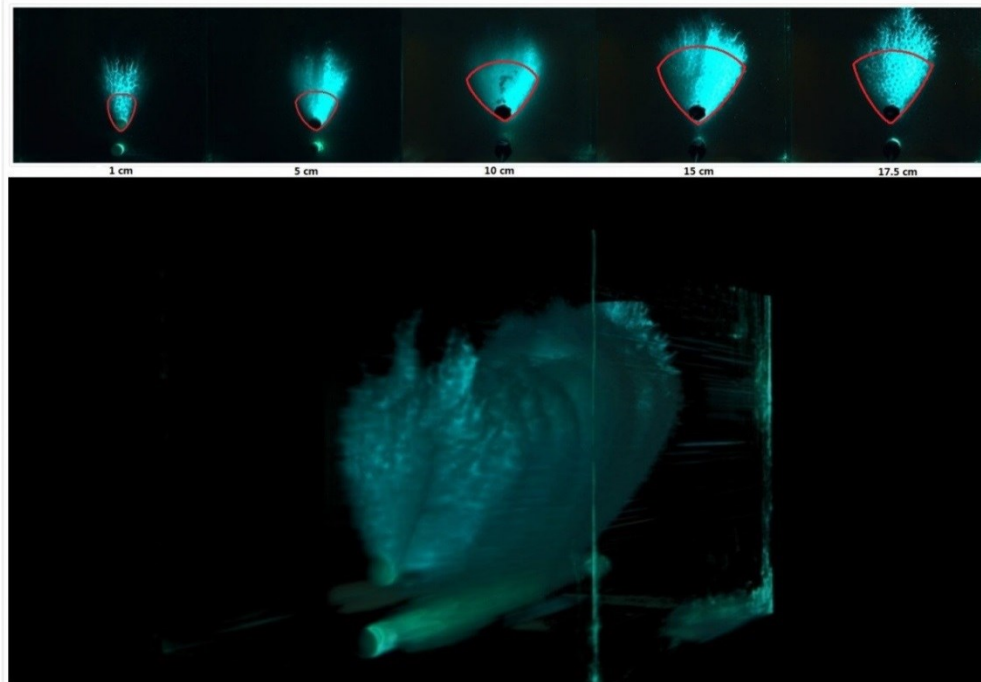
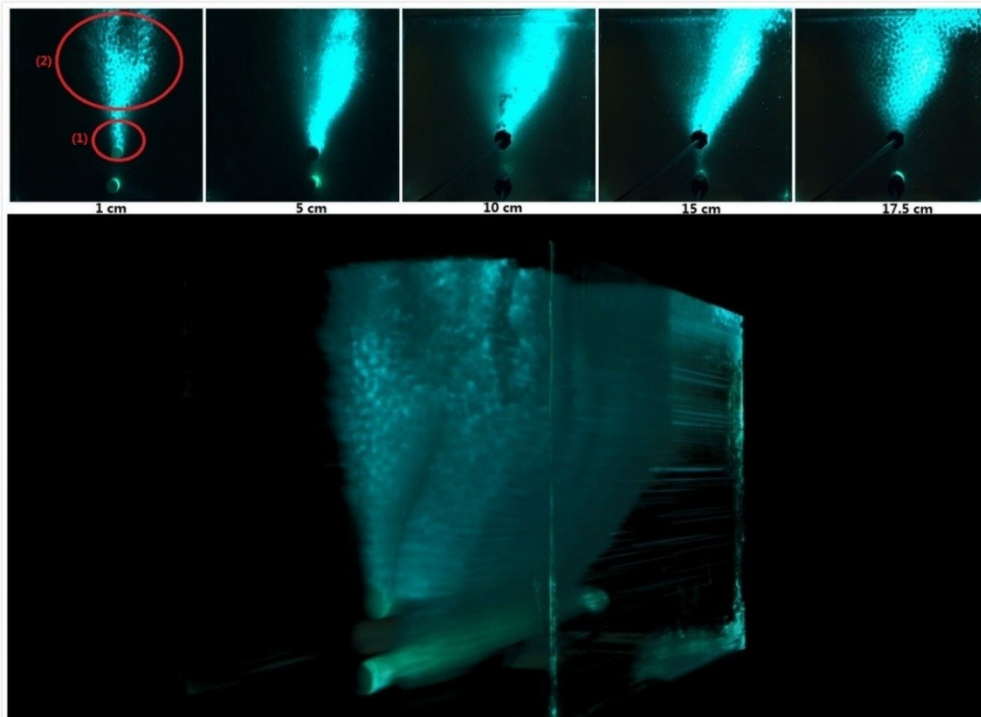


Fig. 3.14—VAPeX injected at 3 ml/min followed by 0.5 ml/min at 1 cm, 5 cm, 10 cm, 15 cm, 17.5 cm and 3-D images from the toe at 12 min.



**Fig. 3.15—VAPEx injected at 3 ml/min followed by 0.5 ml/min at 1 cm, 5 cm, 10 cm, 15 cm, 17.5 cm and 3-D images from the toe at 18 min.**



**Fig. 3.16—VAPEx injected at 3 ml/min followed by 0.5 ml/min at 1 cm, 5 cm, 10 cm, 15 cm, 17.5 cm and 3-D images from the toe at 55 min. Two parts of the chamber are obvious: (1) Very narrow located near the injector, and (2) wide above this narrow part.**

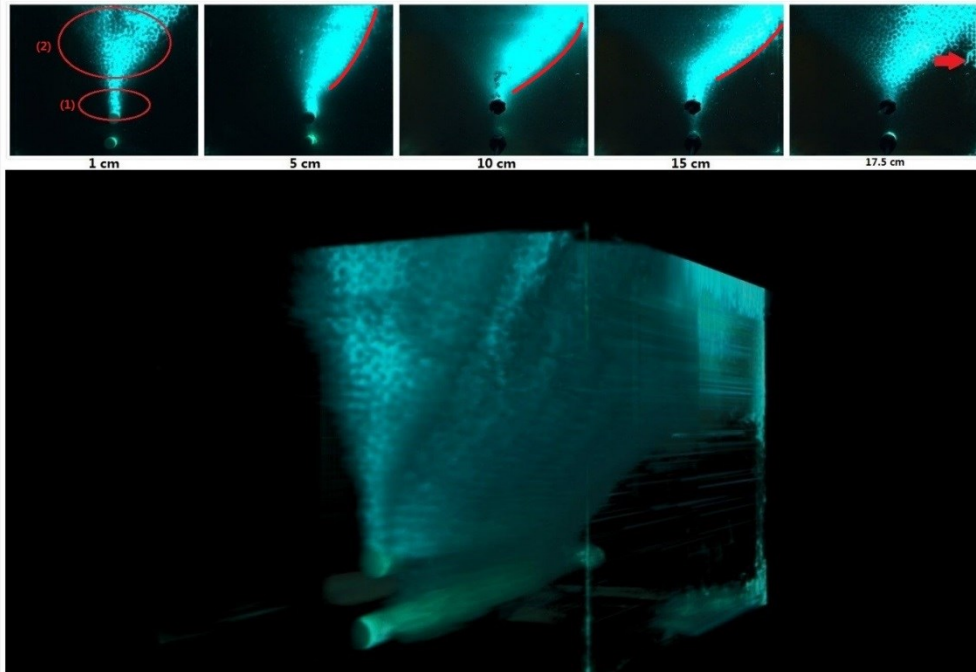


**Fig. 3.17—VAPOR injected at 3 ml/min followed by 0.5 ml/min at 1 cm, 5 cm, 10 cm, 15 cm, 17.5 cm and 3-D images from the toe at 88 min. Two parts of the chamber are obvious: (1) Very narrow located near the injector, and (2) wide above this narrow part.**

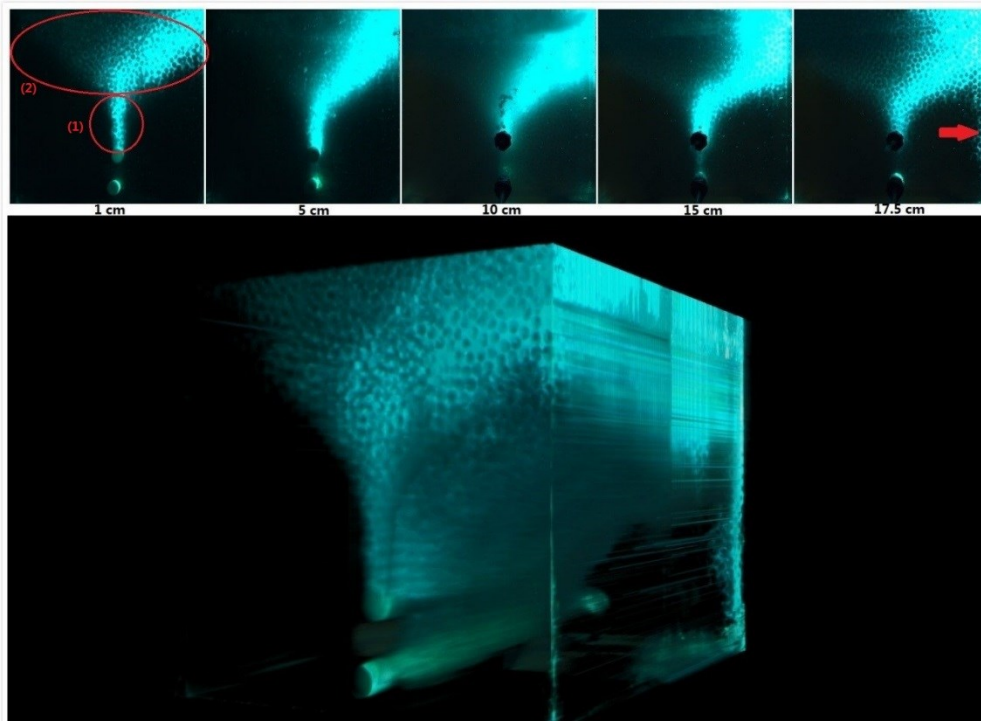


**Fig. 3.18—VAPOR injected at 3 ml/min followed by 0.5 ml/min at 1 cm, 5 cm, 10 cm, 15 cm, 17.5 cm and 3-D images from the toe at 165 min. Two parts of the chamber are obvious: (1) Very narrow located near the injector, and (2) wide above this narrow part.**

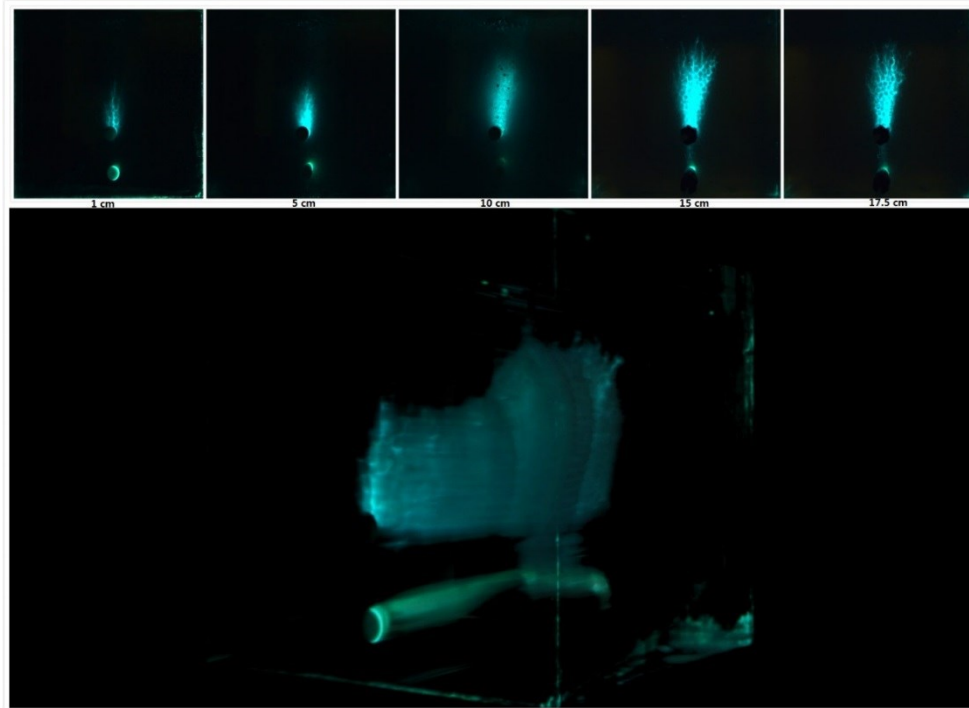


**Fig. 3.19—VAPeX injected at 0.5 ml/min followed by 3 ml/min at 1 cm, 5 cm, 10 cm, 15 cm, 17.5 cm and 3-D images from the toe at 23 min.**

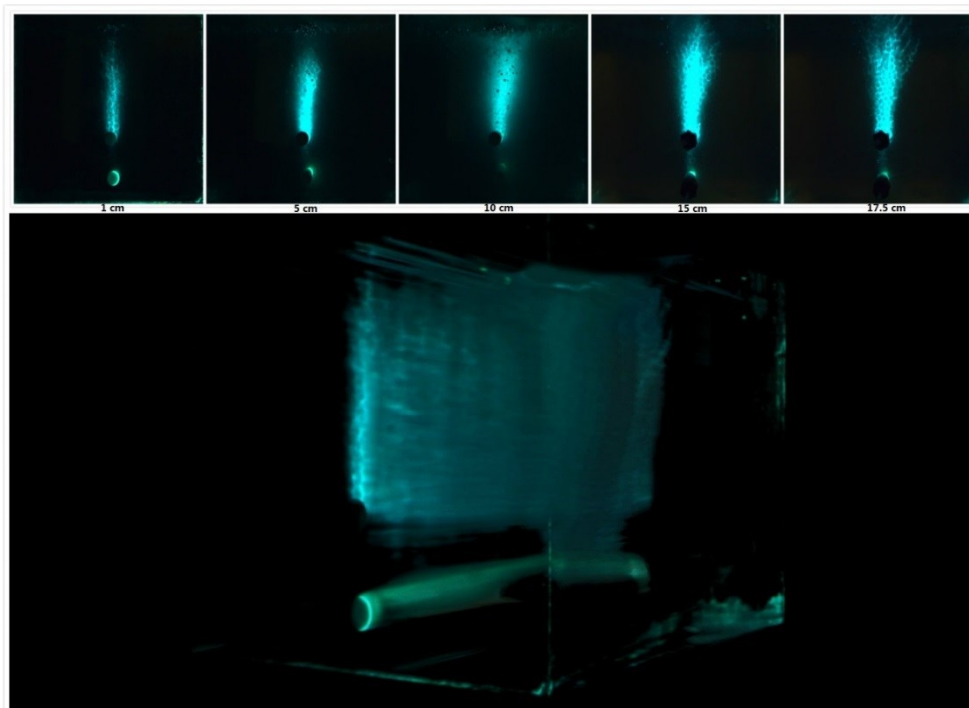


**Fig. 3.20—VAPeX injected at 0.5 ml/min followed by 3 ml/min at 1 cm, 5 cm, 10 cm, 15 cm, 17.5 cm and 3-D images from the toe at 46 min.**

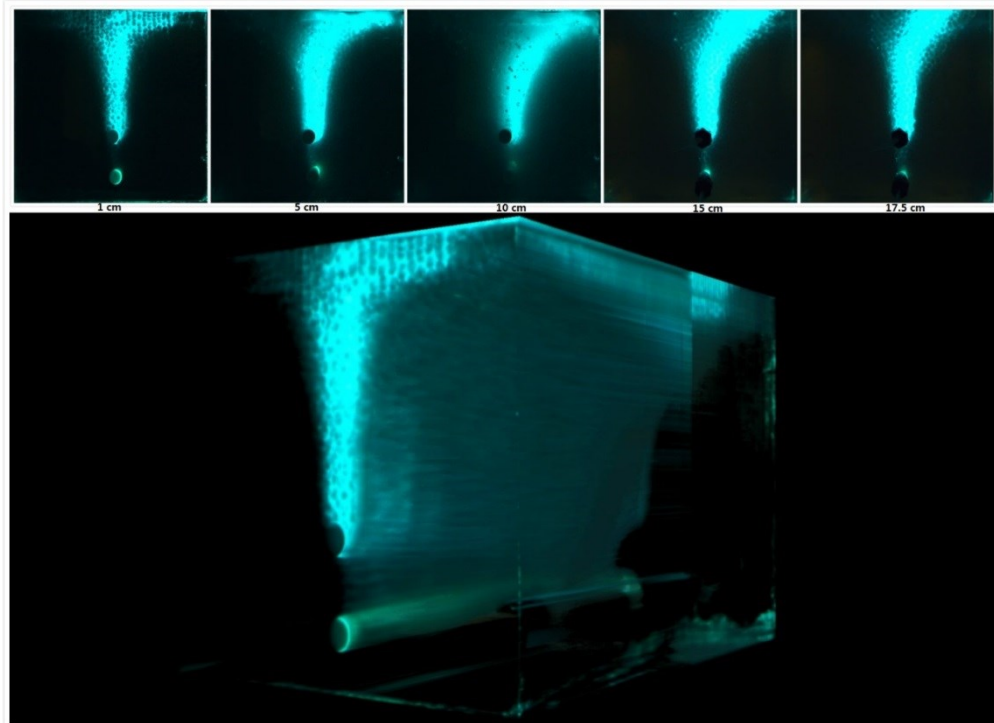


**Fig. 3.21—VAPEx injected at 0.5 ml/min followed by 3 ml/min at 1 cm, 5 cm, 10 cm, 15 cm, 17.5 cm and 3-D images from the toe at 102 min.**

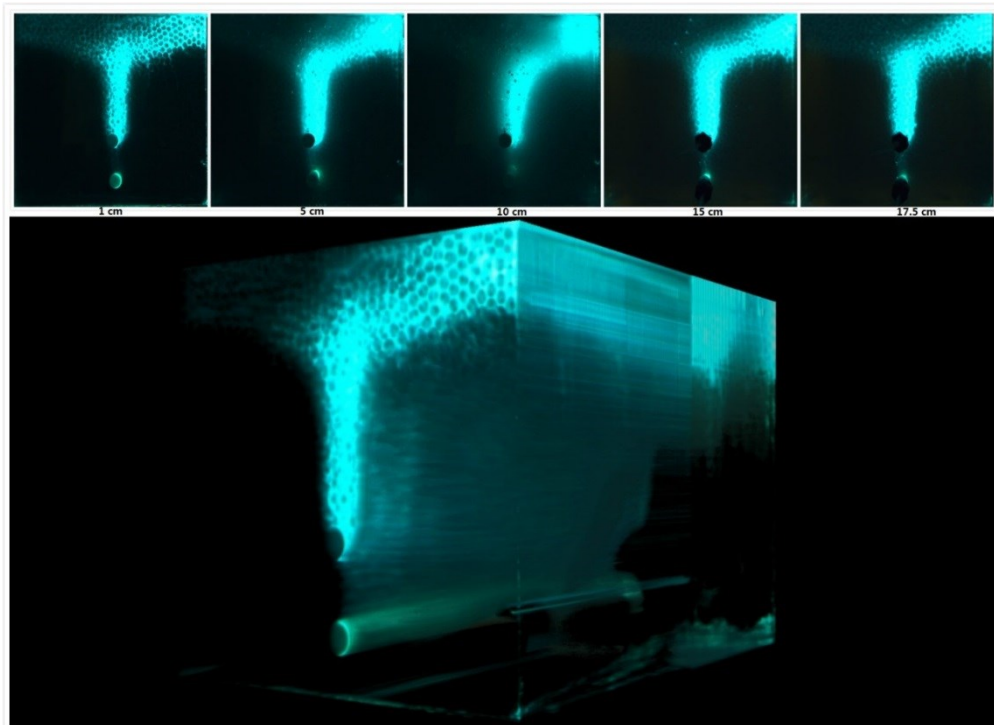


**Fig. 3.22—VAPEx injected at 0.5 ml/min followed by 3 ml/min at 1 cm, 5 cm, 10 cm, 15 cm, 17.5 cm and 3-D images from the toe at 159 min.**

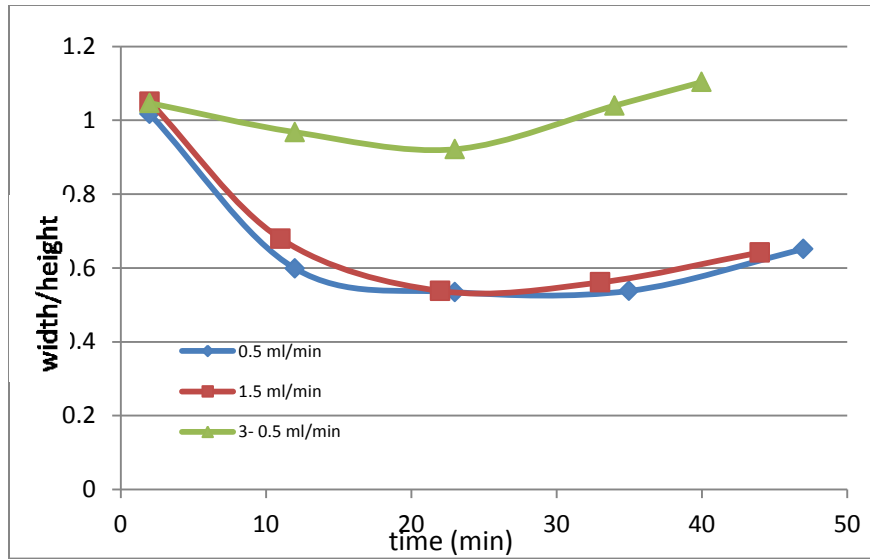


**Fig. 3.23—Ratio of maximum width over maximum height of the solvent chambers with time at injection rates of 0.5 ml/min, 1.5 ml/min, and 3-0.5 ml/min.**

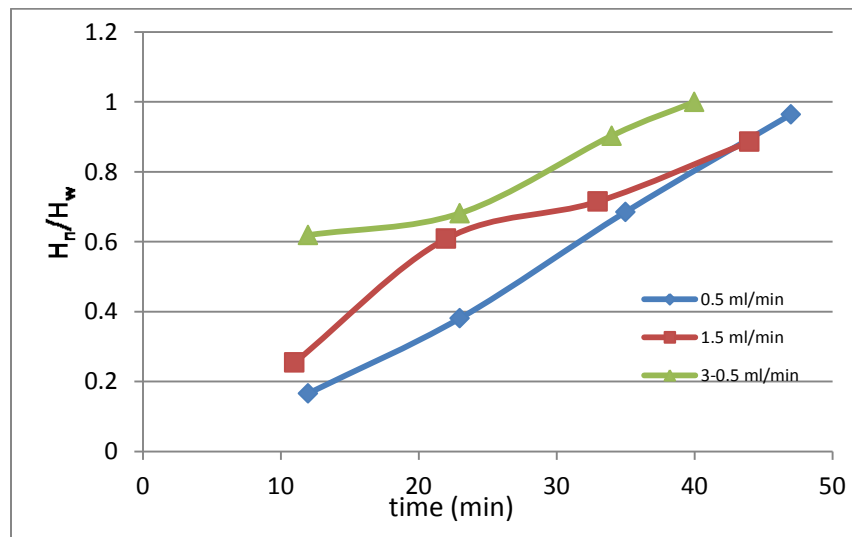


**Fig. 3.24—Ratio of height at the toe and at the heel of the injector with time at injection rates of 0.5 ml/min, 1.5 ml/min, and 3-0.5 ml/min.**

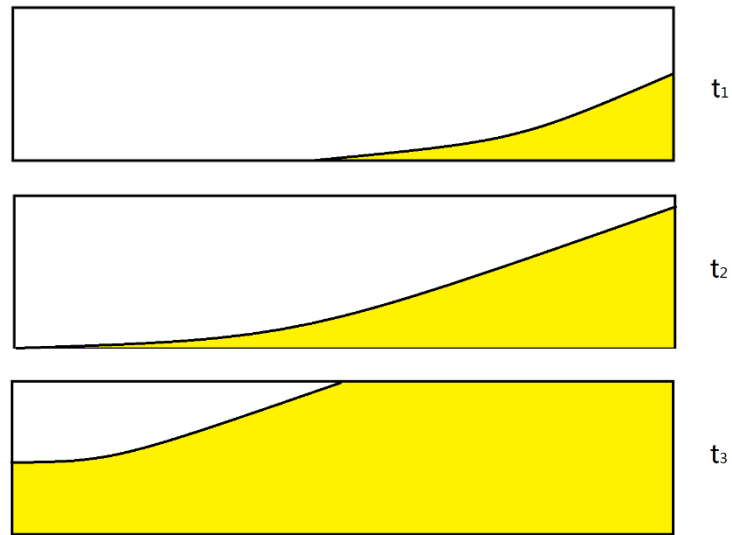


Fig. 3.25—Solvent propagation in the injector at different time where  $t_1 < t_2 < t_3$ .

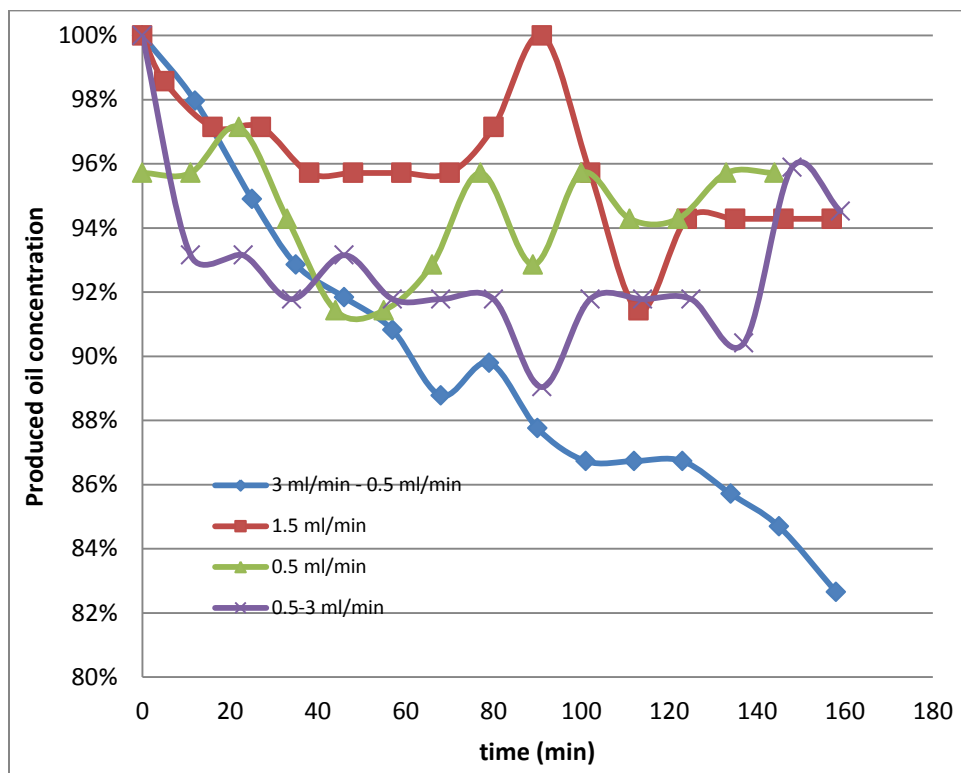


Fig. 3.26—Oil concentration in the produced fluids vs. time for different injection rates and scenarios.

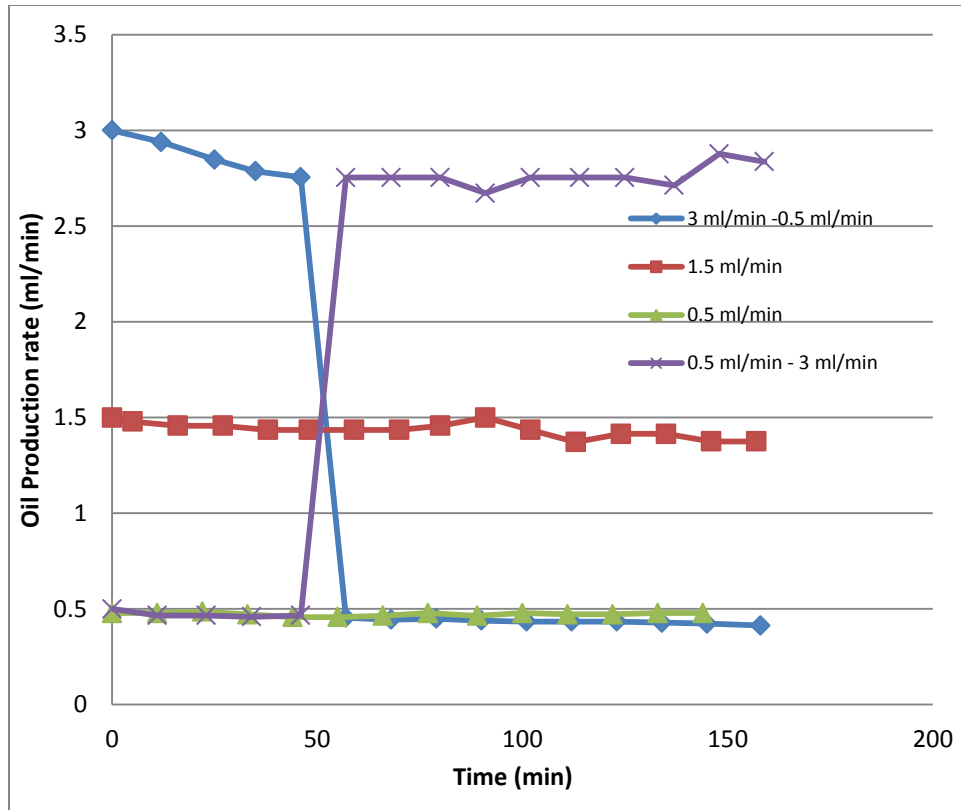


Fig. 3.27—Oil production rate vs. time for different injection rates and scenarios.

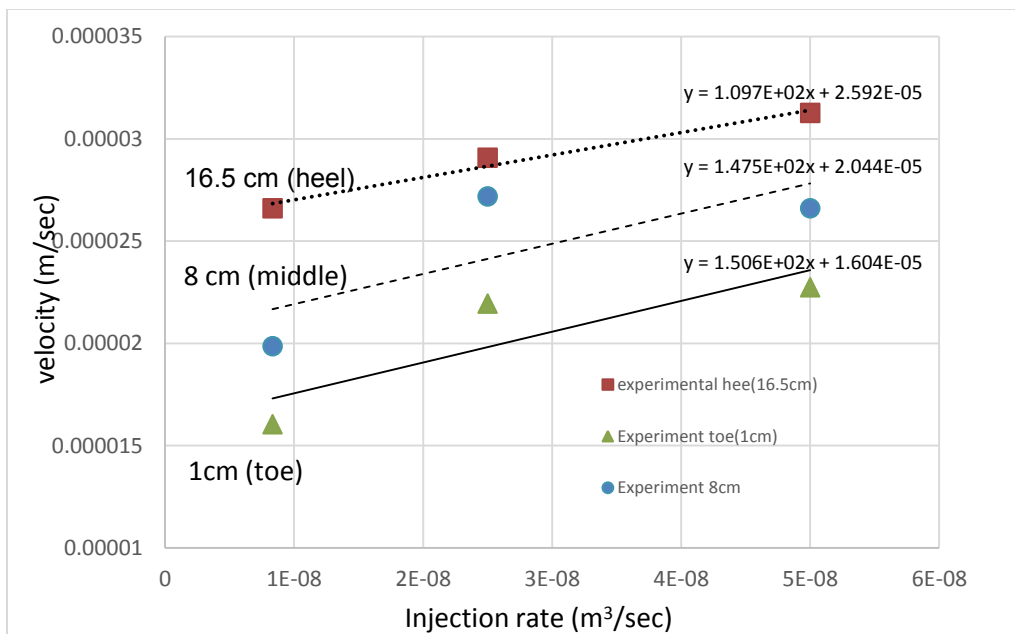
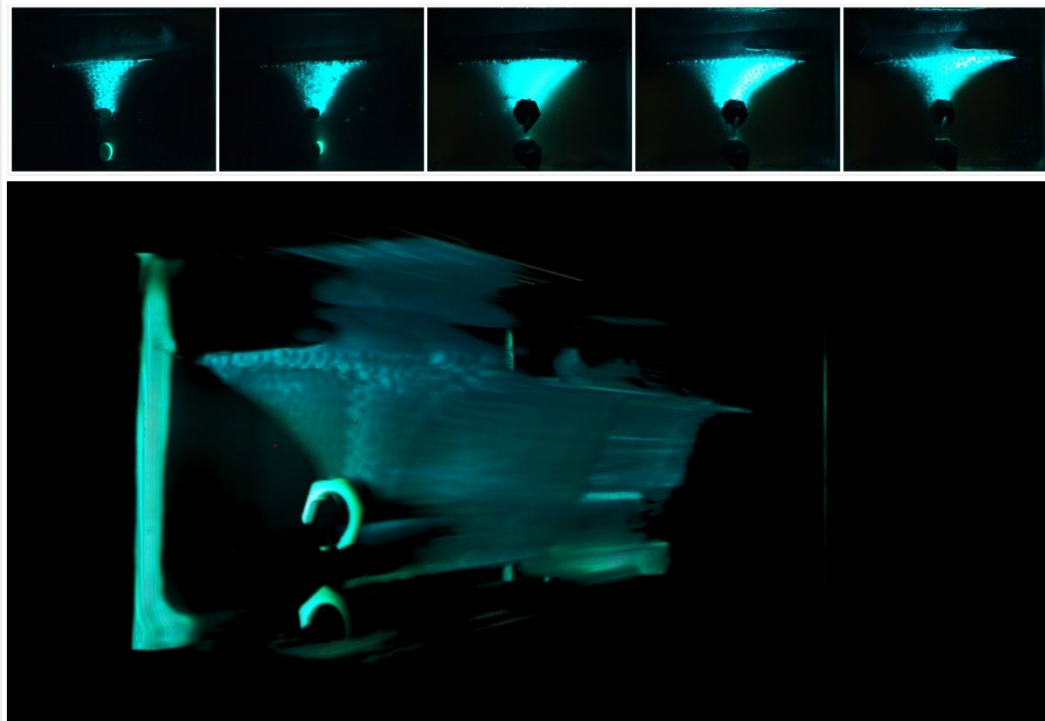


Fig. 3.28—Matching of solvent front progressing velocity vs. injection rate at the heel (16.5 cm), in the middle (8 cm), and at the toe (1 cm). Symbols: Experimental data. Straight lines: Best matches to the experimental data using Eq. 5 and constants given in Table 3.4.



**Fig. 3.29—VAPEx injected at 1.5 ml/min into the model with low permeability zone at the top at 1 cm, 5 cm, 10 cm, 15 cm, 17.5 cm and 3-D images from the heel at 69 min.**



**Fig. 3.30—VAPEx injected at 1.5 ml/min into the model with low permeability zone at the top at 1 cm, 5 cm, 10 cm, 15 cm, 17.5 cm and 3-D images from the heel at 147 min.**

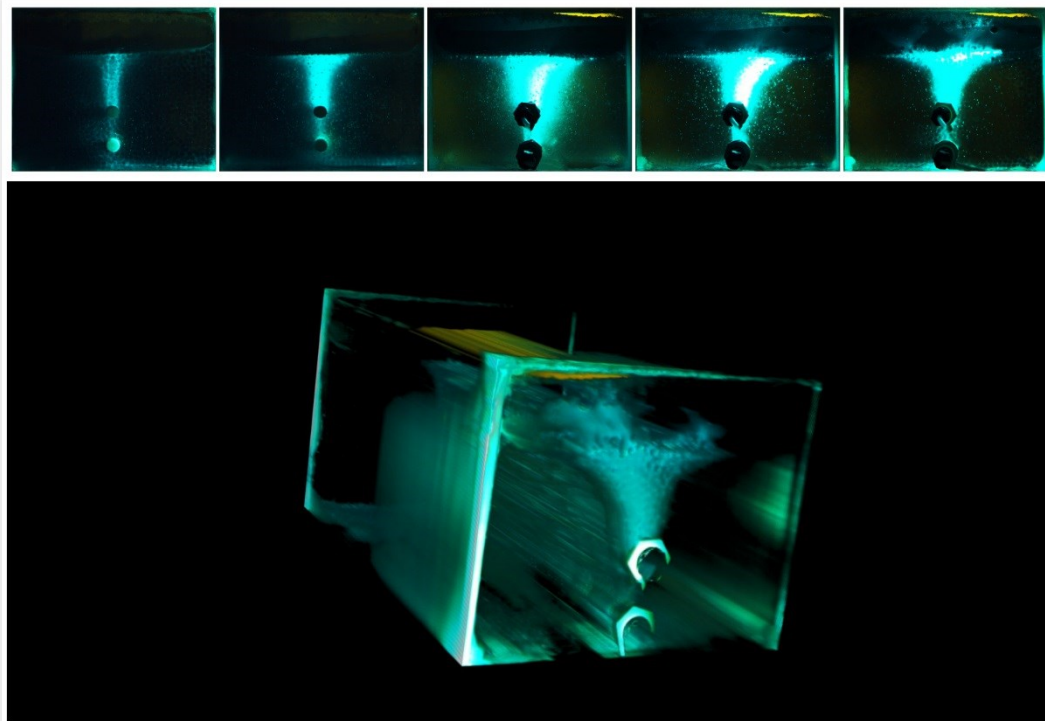


**Fig. 3.31—VAPEx injected at 0.5 ml/min into the model with low permeability zone at the top at 1 cm, 5 cm, 10 cm, 15 cm, 17.5 cm and 3-D images from the heel at 79 min.**

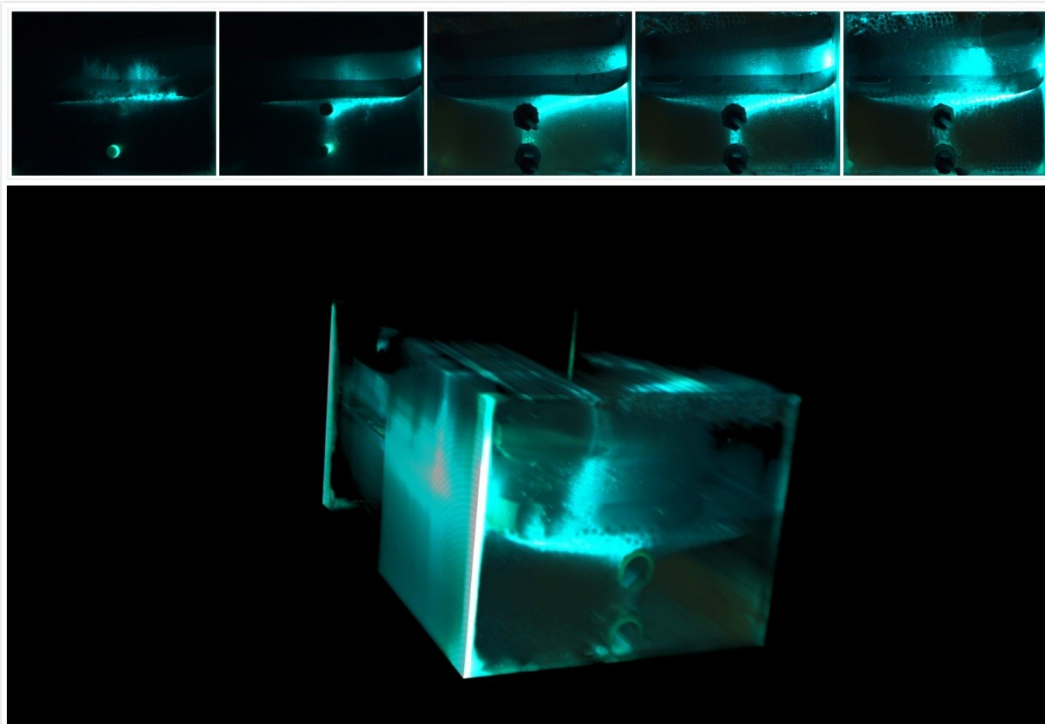


**Fig. 3.32—VAPEx injected at 1.5 ml/min into the model with low permeability zone in the middle at 1 cm, 5 cm, 10 cm, 15 cm, 17.5 cm and 3-D images from the heel at 93 min.**

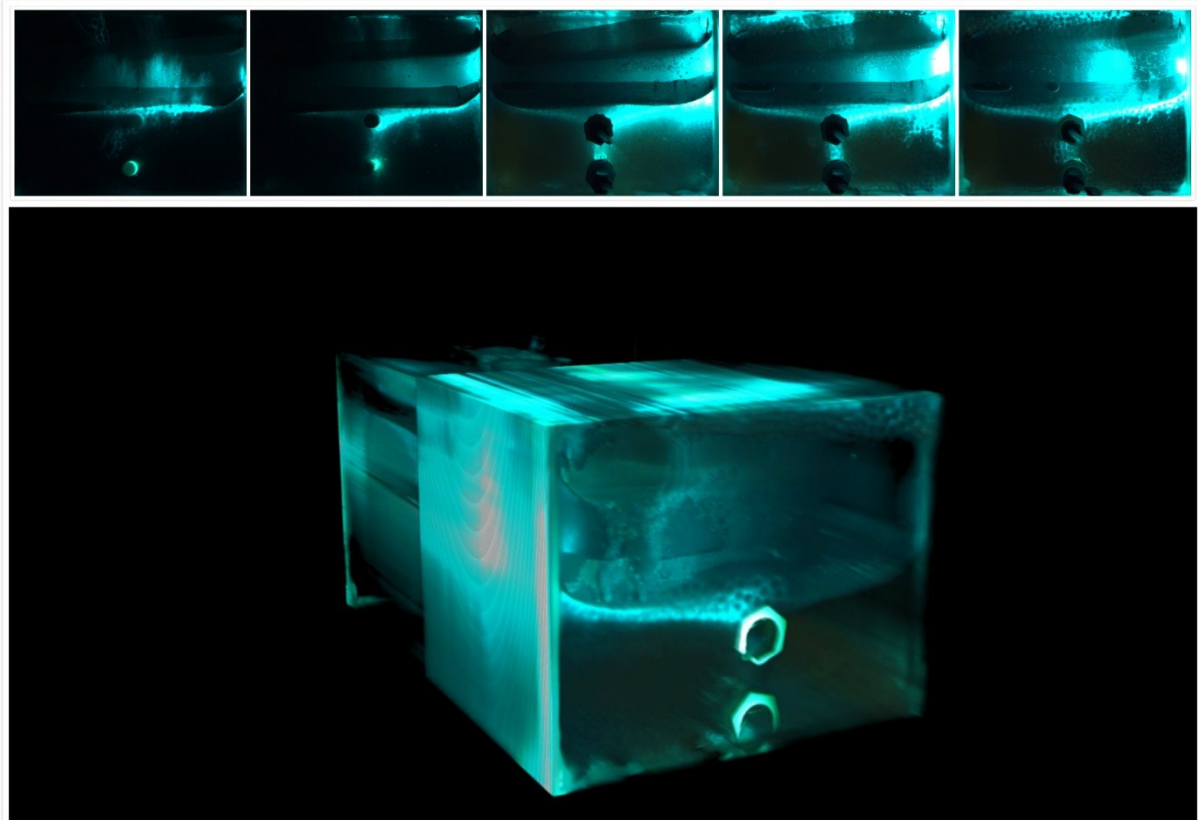


**Fig. 3.33—VAPEx injected at 1.5 ml/min into the model with low permeability zone in the middle at 1 cm, 5 cm, 10 cm, 15 cm, 17.5 cm and 3-D images from the heel at 147 min.**

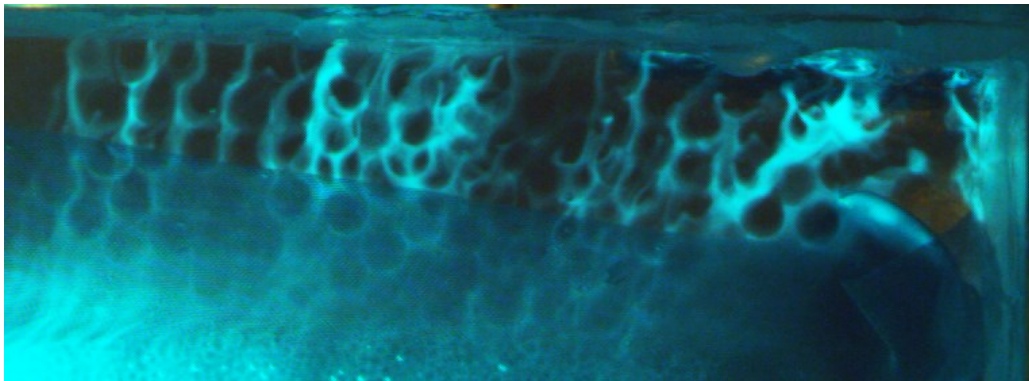


**Fig. 3.34—Zoom of transition from low permeability zone to high permeability zone with injection rate of 1.5 ml/min.**

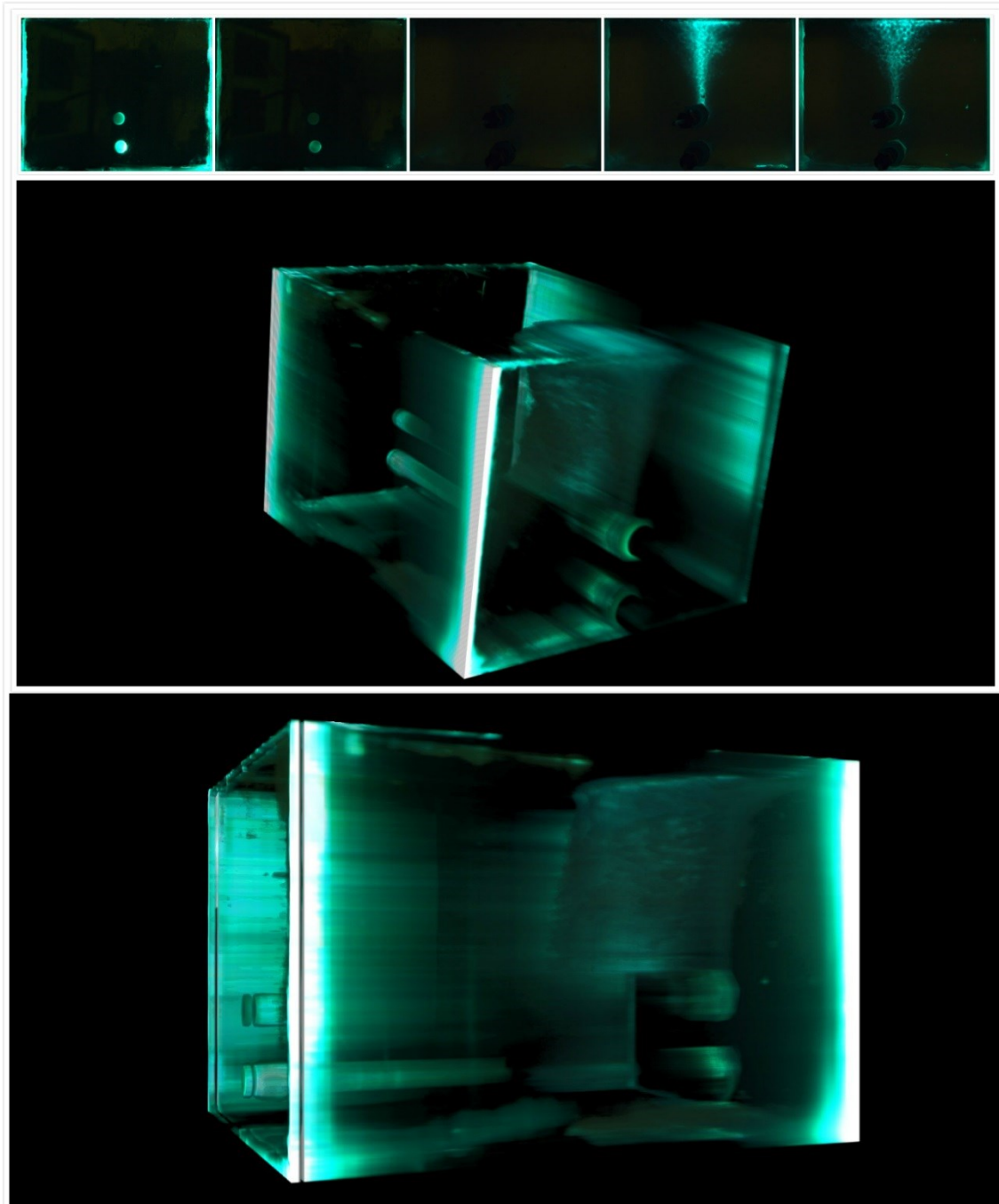


**Fig. 3.35—VAPEx (solvent 2) injected at 1.5 ml/min at 1 cm, 5 cm, 10 cm, 15 cm, 17.5 cm and 3-D images from the toe (middle) and the side (bottom) at 5 min.**

## **CHAPTER 4: 3-D Visualization of Solvent Diffusion into Oil Saturated Porous Media Using Laser Technology and Fractal Analysis of the Mixing/Displacement Process**

---

This paper is submitted to a journal.

## 4.1 Preface

A 3-D visualization technique with laser sheet scanning of refractive index matched glass-bead-pack model was used to study the effect of permeability, solvent density, viscosity and boundary effect on mixing by diffusion. Three types of solvents were used: (1) solvent with density higher than oil but low viscosity, (2) solvent lighter than oil but has relatively high viscosity, and (3) light and thin solvent. The permeability of 1 mm and 4 mm glass beads was about 70 Darcy, and 1120 Darcy, respectively.

The fractal dimension of the solvent diffusion front in 3-D calculated by the box-counting method was applied to compare the progress of the solvent-oil interfaces (mixing) for different conditions. Wider fingers or swept areas were observed for less viscous solvent, which results in lower fractal dimension. The solvent front tends to develop along both oil- and water-wet boundaries (plexiglaas and glass models, respectively), but more obvious in the high permeability model with oil-wet walls. Solvent 1 and 2 slowly mixed and rose to the top of the model filling most of the pores in the model, and then diffuse into the unsweep region. Solvent 3 reached the top of the model in an extremely short time along the boundary with thin fingering, displaces downward afterwards. These frontal progresses were analyzed quantitatively through the change of the fractal dimension during the process.

## 4.2 Introduction

Mixing processes in porous media are commonly encountered in oil, gas, groundwater, nuclear waste depository and CO<sub>2</sub> storage reservoirs. In a specific case, when a miscible fluid is injected into a fractured reservoir containing oil, a mass transfer occurs between the oil saturated rock matrix and solvent saturated fracture. This transfer is purely diffusive (Fickian type) but as the non-equilibrium condition is reached in the matrix due to density difference caused by mixing, gravity controlled convective mass transfer also takes place in addition to diffusion inside the rock matrix. Clear understating of the physics of this process is critically important to optimize this process from economics (expensive solvent is used in oil reservoirs) and environmental points of view (permanent sequestration of CO<sub>2</sub> or storage of nuclear waste).

Experimental analyses of oil-solvent mixing by diffusion in the presence of porous media have been practically done through core experiments. Although this type of experimentation is able to represent the process in 3-D, visualization of the frontal process may not be easily done to scrutinize the frontal progress of the mixing process. Hatiboglu and Babadagli (2004, 2007a) clarified the effects of matrix shape, gravity, viscosity, and wettability through core experiments, which may be considered as 3-D approach. They further performed parametric analyses visually using 2-D glass beads packed models under immiscible (Hatiboglu and Babadagli, 2010) and miscible conditions (Hatiboglu and Babadagli, 2007b; Hatiboglu and Babadagli, 2008). A convective displacement was observed when the matrix-fracture diffusive interaction takes place in a counter-current manner.

When a lower viscosity fluid displaces viscous fluid, the viscous fingering will be formed and the displacement yields a diffusion limited aggression (DLA) type displacement (Lenormand,

1989). DLA is a process where particles do random walk and create a branch like cluster. Hatiboglu and Babadagli (2008) simulated the diffusion process from this random walk theory. Gharbi et al. (2001) and Doorwar and Mohanty (2011) related the fractal dimension with the diffusion fingering and sweep efficiency. Gharbi et al. (2001) concluded that the areal sweep efficiency increases as the gravity difference and the viscosity ratio increase. Doorwar and Mohanty (2011) indicated that the number of fingers decreases as the viscosity ratio increases, and the process is more close to DLA type (random walk) as the viscosity ratio increases.

Visual analysis is essential in clarifying the physics of the DLA type displacement/mixing process but studies are limited to 2-D porous models due to limitations in visualization of porous media. However, such a complex process in which diffusion, convection and gravity play a role, may not be clearly understood through 2-D visual systems to should be visually analyzed in 3-D to establish data for further numerical model studies.

This paper studies the boundary effects, viscosity ratio, density, and permeability solvent diffusion into oil saturated porous media by 3-D visualization using laser technology. After analyzing the images qualitatively, a quantitative analysis was done using the fractal dimensions of the displacement/mixing front.

### **4.3 Experimental Theory and Details**

The basic idea of the laser sheet 3-D scanning system is to build a 3D image from a stack of 2D images which present the distribution of oil, solvent, and porous media located with a significantly small distance apart from each other. This requires a special design of the porous media model as explained below.

4.3.1 Model. The model used is cubic with a side length of 5 cm filled densely with 1 mm and 4 mm glass beads. The permeability is 70 Darcy and 1120 Darcy for 1 mm and 4 mm glass beads, respectively, based on the calculation through the Kozeny-Carman equation (Mavko and Nur, 1997). The models were made of oil-wet (plexiglass) and water-wet (glass) materials to clarify the boundary (wall) effect (Fig. 1). The cubic model was placed in a 1.5 cm deep solvent tray with a 4-6 layers of a cloth at the bottom. The cloth introduces a several millimeter gap between the tray and the model to allow the solvent to enter the model uniformly. Hence, the solvent contacts with the porous media model from the bottom part only and, as the all other sides are close to flow, the interaction takes place in a counter-current manner as typically encountered in underground -fractured- reservoirs.

**4.3.2 Refractive index matching.** In order to take 2D images at any location in a model with a camera, the glass beads have to be invisible in the oil and solvent. This means that the refractive indices (RI) for all the materials including in the model the oil, solvent and the porous media must be the same (Chen and Wada; 1986, Wiederseiner et al., 2001). Fig. 4.2 shows the invisible glass beads in the fluid at the bottom compared with the glass beads in the air at the top. As the RI of the solid is constant at the same temperature, the RI's of the fluids were adjusted to the same RI as the glass beads by mixing the fluids with different RI's. The RI's of the common transparent solvents and oils in the lab yield from 1.38 to 1.52 (Table 4.1). Therefore, the glass beads used in the experiments have the RI of 1.473, which is in the range of 1.38-1.52.

Four mixtures of fluids were generated with densities from 0.830 g/cc to 0.908 g/cc and viscosities <1 cP up to 45 cP (Table 4.2). The mixture with maximum viscosity was selected as the oleic phase. Solvent 1 was denser than the oleic phase; solvent 2 was lighter but the viscosity was close to the oil; solvent 3 had significantly lower viscosity than the oleic phase. A list of experiments is given in Table 4.3.

**4.3.3 Experimental set-up (Fig. 4.3).** The experiment was operated in a dark room. The solvent was colored by yellow fluorescent dyes which is visible with the excitation of a blue (wavelength: 445 nm) laser sheet. Therefore, only the solvent in the image with laser excitation was visible and the oil and glass beads were dark. Two cameras located at the front and back of the model took pictures when the laser system - and sheet- moves every 1 mm. After scanning the whole model, a movable stage carried the laser to the starting position. As the laser is in the visible range, the blue becomes noise for the yellow solvent. Therefore, a filter which blocks the blue laser and transmits the yellow light was attached on the lens of the camera.

#### **4.3.4 Image processing and fractal dimension (box-counting analysis).**

On the basis of the above explained design and conditions, the brightness of the image represents the concentration of the solvent due to the absorption and multi-reflection of laser in the liquid and the glass beads. The original images were made into binary by setting a threshold at different brightness values (50, 80 and 100). 3-D surface images (Fig. 4.4) show the solvent swept region with high concentration is smaller than that with lower concentrations. Notice that threshold range is from between 0 and 255. Even though a threshold value of 50 is small, the darker region still needs to be filtered out. Then, the outlines were picked out (Fig. 4.5). Stacking the 2-D images to 3-D and converting them into binary, the fractal dimension of the interface (front) were calculated using ImageJ (Rasband, 1997-2005).

We used box counting fractal dimension of the solvent and oil interface (displacement or mixing front) to quantify the “smoothness” of the solvent front. Box-counting method was applied to calculate the fractal dimension (D):

$$D = \frac{\log(N_r)}{\log\left(\frac{1}{r}\right)} \quad (1)$$

$N_r$  is the number of boxes with side length  $r$  (Sarkar and Chaudhuri, 1994; Du et al., 2009). The slope of a log-log plot of  $N_r$  vs.  $1/r$  with different  $r$  is the fractal dimension. The fractal dimension equals 2 for a continuous flat surface. The value will increase for a rougher surface.

## 4.4 Experimental Results and Analysis

### 4.4.1 Solvent 1 diffusion into 4 mm glass beads packed plexiglass (oil-wet) wall model.

A strong boundary effect is observed, i.e., the solvent progressed faster at the left front and right back corner, and along the back and right wall (Figs. 4.6 and 4.7). Hatiboglu and Babadagli (2008) observed a similar behaviour in the 2-D counter current visualization experiments. They pointed out that the “initial -inner- pressure distribution” resulted in less resistance of the flow near the boundary. Another reason is the wettability of the model wall. When the solvent reached the top through the corners and the walls of the model, it propagated along the top of the model and slowly diffused into the centre from the solvent existing corners, walls and the top. Although there exist no immiscible fluids in the system, the affinity of diffusing phase (solvent) to the wall of the model compared to the oil is still a critical issue. While mixing is occurring, there is still a period over which a non-zero interfacial tension is applicable and during this period the solvent might progress through the walls faster than diffusing into (and mixing with) oil. As will be discussed later, if the wall is made of glass the diffusion behavior is different as a proof of this.

The fractal dimension increases as the interface becomes more complex and the behavior is linear within the time period (10 hrs) applied (Fig. 4.8). What is more interesting is that the setting the threshold (brightness) is critically important as it is implicitly a representation of the

concentration of the solvent. Therefore, different threshold levels represent different mixing levels and the evaluation will be made for three threshold values throughout this paper.

Another parameter to be considered is the effect of boundary condition (the wall of the model). To avoid this effect, fractal analysis were also made for the middle part of the cubical model (3 cm (width) x 3 cm (length) x 5 cm (height)). Significant change was observed when the center part was considered for threshold values of 80 and 100 (Fig. 4.9a). A decline in the fractal dimensions was observed nearly after 6 hours (Fig. 4.9b-c) and in turn the front loses its fractal nature (dimension less than 2). These threshold values (80 and 100) captured the reach of the front at the top of the model and start of convective transport (displacement towards the bottom due to gravity difference). A similar behavior was reported and visualized by Hatiboglu and Babadagli (2007b).

As seen in Figure 4.8, at a higher concentrations of solvent (i.e., lower threshold levels such as 50 and 80), the front progresses in a uniform manner after 6 hours so that the fractal dimension becomes stable. The visual support for this is shown in Fig. 4.10 at the pore scale (circled in red). Over this two-hour period, the diffusion process did not change fractally while it progressed.

4.4.2 Solvent 2 diffusion into 4 mm glass beads packed plexiglass (oil-wet) wall model. The boundary effect is more pronounced for solvent 2 compared with solvent 1. The solvent at the right back and the left front corners rose faster. Then, solvent fingering formed in the centre of the model (Figs. 11). The width of the solvent swept area was narrower than that for solvent 1.

Similar to solvent 1, the fractal dimension increased with time (Fig. 4.12) but the values of the fractal dimension is higher indicating existing of more complex front (fingers). This can be identified through visual analysis of the refined images given in Fig. 4.7 and 4.11. Also note that a

linear behavior was obtained for the threshold values of 80 and 100 during the process (18 hours) (Fig. 4.12) while it was flattened after six hours for solvent 1 (Fig. 4.8). Due to lower density, the solvent tended to rise rather than quickly in the case of solvent 2 despite its higher viscosity than solvent 1. Hence, the fractal dimension showed an increasing trend.

Interestingly, the fractal dimensions obtained for the images from the central part of the model are similar to the ones obtained for the whole model because the process was predominantly continued at the center (as fingering) unlike solvent 1 (Fig. 4.12). Slightly lower fractal dimensions in the centre can be attributed to the solvent rise through right back corner which was included in the whole model evaluation (blue diamond symbols in Fig. 4.13).

**4.4.3 Solvent 2 diffusion into 4 mm glass beads packed glass (water-wet) wall model.** To clarify the effect of boundaries (walls of the model), the material used to manufacture the cubical model was changed to glass. The boundary effect is still felt as shown in the raw (Fig. 4.14a). Fingers were formed at early times (Fig. 4.14a) but the solvent diffuse more uniformly sweeping the whole model eventually (Fig. 4.14d ). In other words, the solvent in the center progressed as fast as the solvent along the walls. As a result, the difference in fractal dimensions for the whole model and the center turned out to be small (Fig. 4.15 ).

The fractal dimension for low threshold (50) starts to decrease after 9<sup>th</sup> hours (Fig. 4.16). One may observe through images in Fig. 4.14c (8 hrs) and Fig. 4.14d (11 hrs), the solvent reached the top of the model and started to fill the non-swept region. This effect was felt earlier for threshold of 50 (fractal dimension stabilizing after 8 hours), while it occurred after 11 hours for the threshold level of 80.

**4.4.4** Solvent 2 diffusion into 1 mm glass beads packed glass (water-wet) wall model. Fingers were thinner in this case due to smaller grain size (or lower permeability). They were more obvious along the front and left walls and the swept region was wider and smoothed off at the front left corner (Fig. 4.17). The wall did not affect the process as much as it did in the 4 mm glass beads packed model cases. The whole experiments took 32 hrs, significantly longer than the larger glass beads porous media (11 hrs).

In general, the fractal dimension is lower than that for 4 mm glass beads models (Fig. 4.18). By viewing the 3-D surface images, one may observe that the surface of the large glass beads contribute to the complexity of the solvent interface. Similar to the last experiment, the fractal dimension increased when the solvent propagated upward, and then decreased as the solvent started displacing downwards after 23<sup>rd</sup> hr, i.e., convective transport region (Fig. 4.17d).

Although the whole model showed a linear trend of fractal dimension changes (Fig. 21), the values obtained for the center images were more erratic (Fig. 4.19a). Initially, the fractal dimension in the center of the model was higher than that for the whole model because the solvent moved predominantly in the center (Fig. 19b-d). The value in the centre decreased earlier because the solvent progressed faster around the boundary and reached at the top of the model after 24 hrs (Fig. 20c). Then, convective transport (downward displacement by gravity) started and the solvent gradually displaced oil by mixing with it from left to right in the centre.

4.4.5 Solvent 3 diffusion into 4 mm glass beads packed glass (water-wet) wall model. The solvent front reached at the top of the model in less than 5 min along the left front, right front and back corners due to the large density difference between the oleic phase and solvent 3 (Figs. 20). There was no solvent rising at the center and the solvent quickly spread along the top of the model and moved downward sweeping quite uniformly. The whole process took only 4 hrs.

At a low concentration (threshold 50), the fractal dimension dropped in one hour (Fig. 21) and due the short time for solvent rising to the top, the increase in fractal dimension was not detected. Then, the fractal dimension declined while the solvent was spreading along the top (first hour). When the solvent started displacing downward, the fractal dimension increase slightly (between 1 and 2 hours). Finally, the value dropped sharply when the solvent filled the unswept pores at the bottom (between 2hrs and 3 hrs). However, at higher concentrations (thresholds 80 and 100), the fluctuation was not observed (Fig. 21) and a similar trend was followed by these two cases.

The center images showed similar trends (Fig. 22a). However, the fractal dimension in the centre was significantly lower than that for the whole model (Figs. 22b, c, and d) due to highly boundary controlled process.

**4.4.6** Solvent 3 diffusion into 1 mm glass beads packed glass (water-wet) wall model. The diffusion process was observed to be the same as the 4 mm glass beads case, but the swept regions along the walls were thicker and the progress was twice slower (Figs. 23). After an increase in the fractal dimension due to fingering type progress within the first hour (Figs. 27a and 23a), similar fluctuations to the larger (4mm) beads model was observed until the end of experiment (Fig. 24). The boundary effect resulted in significantly lower fractal dimensions in the centre as well (Fig. 25a).

The fractal dimension in the centre for solvent 3 was less than the solvent 2 case at the beginning of the experiments. Since almost no solvent entered into the center of the model, there was not a continuous surface but some spots in this space and this resulted in fractal dimension less than 2 in the beginning (red curves in Figs. 25a, b, c, and d). They later increased and eventually converged to 2 at the end of the experiment.

**4.4.7** Comparison with 2-D results. A 2-D version of similar experiments were performed by Hatiboglu and Babadagli (2005). Fig. 26 shows the comparison of fractal dimension changes over the displacement process with their experiments (two curves marked as 2-D). They observed an increase in fractal dimension during solvent front development, and then it decreased after the solvent progressed to the top in 2-D experiments. They also found that for the lower mobility ratio vertical diffusion case, there is a tiny drop in the fractal dimension around 1000 sec while the solvent progress along the top boundary. The drop exists in the lower mobility ratio (Fig. 18) in 3-D diffusion, but it is more obvious in higher mobility ratio (Figs. 21 and 24). Therefore, their trends are similar to higher mobility ratio cases of our study.

For the same side length (5 cm) of the 3-D and 2-D models, the total progress time for 3-D models is from 4 hours up to 32 hours, while the solvent took 46 min (0.77 hours) to 451 min (7.52 hours) to diffuse the 2-D model (glass bead pack, countercurrent, vertical cases in

Hatiboglu and Babadagli, 2005, 2007b, 2008). The difference in speed is caused by the mobility ratio (from 1.96 to more than 76 in this paper; 7.63 and 95.58 in 2-D cases), the glass beads size (1 mm and 4 mm in this paper, and ~0.1 mm in 2-D experiments) and the capillary pressure due to the shape of the model (capillary pressure in the thin space between 2-D plates). The mobility ratios for both cases are close, and decrease in glass bead size slows the process down as observed in this paper. Also critical is the decline portion of the curves that correspond to downward/convective displacement. 3-D cases of high mobility ration (orange circles and red squares) showed significant decrease in fractal dimensions while it was not significant in the 2-D case. Note that when the fractal dimensions of 2-D experiments, which are to be between 1 and 2, are converted to “3-D” version by adding one, much higher values were obtained (Fig. 27) compared to the 3-D version.

This comparative analysis reveals critical information as to the use of 2-D data to represent a 3-D behavior, which would be crucial in modeling and up-scaling (to field scale matrix shape and sizes) studies. Although 2-D data showed similar trends to 3-D process, certain discrepancies as pointed above needs to be questioned if one wants to apply -simpler- 2-D approach to model the diffusion process into a rock matrix.

## **4.5 Conclusions**

Cubical models made of different materials (oil-wet plexiglass and water wet glass) walls and filled with 1 mm and 4 mm glass beads and different types of oils were used to visualize the - Fickian- diffusion of solvent with different densities and viscosities.

Boundary effect exists in both model types being more prominent with the solvent with extremely low viscosity (solvent 3). The width of the solvent swept region depended on the

density of the solvent. The speed of the process was faster in the high permeability porous media (4mm glass beads). Solvents 1 and 2 propagated into the model from the whole bottom of the model, while solvent 3 reached the top in a short period of time and propagated from the top of model downward representing a convective transport.

The fractal dimension increased before the solvent reached at the top of the model. For solvents 1 and 2, the fractal dimension decreased afterward. However, for solvent 3, the value declined because the solvent took time to spread along the top of the model due to its extremely low viscosity and density. Then, the fractal dimension increased as the solvent propagated from top to bottom, and dropped to a value of 2 (flat surface) as the solvent filled the pores at the bottom by mixing with oil there.

The objective of this paper was to use laser imaging technique to visualize the diffusion controlled mass transfer process. We showed that this technique can be applicable for a wide range of oil-solvent viscosity and density ratios despite its limitations due fixed range of refractive index use. The qualitative analysis supported by 3-D images was complemented through a quantitative analysis using fractal dimensions. The values of fractal dimensions were useful to clarify the physics of the diffusion controlled mixing process. It is hoped that the qualitative and quantitative results totally based on 3-D analysis will be useful in modeling such a complex process more accurately compared to using 2-D modeling version of the process.

## 4.6 References

- Chen, J.D. and Wada, N. 1986. A New Technique for visualizing the Distribution of Oil, Water, and Quartz Grains in a Transparent, Three-Dimensional, Porous Medium. *SPE Form Eval* **1** (2): 205-208. <http://dx.doi.org/10.2118/13349-PA>.
- Doorwar, S., and Mohanty, K., 2011. Viscous Fingering during Non-Thermal Heavy Oil

- Recovery. SPE-146841-MS paper presented at Annual Technical Conference and Exhibition, Denver, Colorado, USA 30 October-2 November. <http://dx.doi.org/10.2118/146841-MS>.
- Fang, F. and Babadagli, T. 2014. Three Dimensional Visualization of Solvent Chamber Growth in Solvent Injection Processes: An Experimental Approach. SPE 170649 presented at SPE Annual Technical Conference & Exhibition, Amsterdam, Netherlands, 27-30 October. <http://dx.doi.org/10.2523/IPTC-18115-MS>.
- Gharbi, R.B.C., Qasem, F., and Peters, E.J. 2001. A Relationship between the Fractal Dimension and Scaling Groups of Unstable Miscible Displacements. *Experiments in Fluids* **31** (4): 357-366
- Hatiboglu, C.U. and Babadagli, T. 2004. Experimental Analysis of Primary and Secondary Oil recovery from Matrix by Counter-Current Diffusion and Spontaneous Imbibition. SPE 90312 paper presented at the SPE Annual Technical Conference and Exhibition, Houston, TX, 26-29 September. <http://dx.doi.org/10.2118/90312-MS>.
- Hatiboglu, C.U. and Babadagli, T. 2005. Visualization Studies on Matrix- Fracture Transfer Due to Diffusion. Paper 2005-077 presented at the Canadian International Petroleum Conference, Calgary, Alberta, Canada, 7-9 June. <http://dx.doi.org/10.2118/2005-077>.
- Hatiboglu, C.U. and Babadagli, T. 2007a. Oil recovery by counter-current spontaneous imbibition: Effects of matrix shape factor, gravity, IFT, oil viscosity, wettability, and rock type. *J. Pet. Sci. and Eng.* **59** (1-2): 106-122. <http://dx.doi.org/10.1016/j.petrol.2007.03.005>.
- Hatiboglu, C.U. and Babadagli, T. 2007b. Lattice-Boltzmann Simulation of Solvent Diffusion into Oil-Saturated Porous Media. *Phys. Rev. E* **76**. <http://dx.doi.org/10.1103/PhysRevE.76.066309>.
- Hatiboglu, C.U. and Babadagli, T. 2008. Diffusion Mass Transfer in Miscible Oil Recovery: Visual Experiment and Simulation. *Transport in Porous Media* **74** (2): 169-184. <http://dx.doi.org/10.1007/s11242-007-9189-1>.
- Hatiboglu, C.U. and Babadagli, T. 2010. Experimental and visual analysis of co-and counter-current spontaneous imbibition for different viscosity ratios, interfacial tensions, and wettabilities. *J. Pet. Sci. and Eng.* **70** (3-4): 214-228. <http://dx.doi.org/10.1016/j.petrol.2009.11.013>.
- Lenormand, R. 1989. Flow through Porous Media: Limits of Fractal Pattern. *Proc. R. Soc. Lond. A* **423**: 159-168. <http://dx.doi.org/10.1098/rspa.1989.0048>.
- Li, J., Du, Q., and Sun, C. 2009. An Improved Box-Counting Method for Image Fractal Dimension Estimation. *Pattern Recognition* **42** (11): 2460-2469. <http://dx.doi.org/10.1016/j.patcog.2009.03.00>.
- Mavko, G. and Nur, A. 1997. The Effect of a Percolation Threshold in the Kozeny-Carman Relation. *Geophysics* **62**: 1480-1482. <http://dx.doi.org/10.1190/1.1444251>.
- Rasband, W.S. (1997-2005), ImageJ, U. S. National Institutes of Health, Bethesda, Maryland, USA, <http://rsbweb.nih.gov/ij/docs/user-guide.pdf>.
- Sarkar, N. and Chaudhuri, B.B. 1994. An Efficient Differential Box-Counting Approach to Compute Fractal Dimension of Image. *IEEE Transactions on Systems, Man, and Cybernetics: Systems* **24** (1): 115-120. <http://dx.doi.org/10.1109/21.259692>.
- Wiederseiner, S., Andreini, N., Epely-Chauvin, G., et al. 2001. Refractive-Index and Density Matching in Concentrated Particle Suspensions: A Review. *Experiments in Fluids* **50**: 1183-1206. <http://dx.doi.org/10.1007/s00348-010-0996-8>.

Refractive Index		
1	Heptane	1.386
2	Light Mineral Oil	1.469
3	Heavy Mineral Oil	1.483
4	Toluene	1.497
5	Kerosene	1.433
6	Silicone Oil	1.520

**Table 4.1 Refractive indices of original materials.**

		Refractive Index	Density g/cc	Viscosity cP
		±0.0003	±0.003	±5
Oleic Phase	Mixture 1 and 3	1.473	0.866	45
Solvent Phase 1	Mixture 5 and 6	1.473	0.908	8
Solvent Phase 2	Mixture 2 and 4	1.473	0.857	23
Solvent Phase 3	Mixture 1 and 4	1.473	0.830	< 1 (0.39 – 0.59)
Porous Media	Glass Beads	1.473	-	-

**Table 4.2 Fluids used in the experiment after refractive index matching.**

Exp. No.	Wall Wettability	Solvent	Glass Beads Size (mm)
1	Oil Wet	1	4
2	Oil Wet	2	4
3	Water Wet	2	4
4	Water Wet	2	1
5	Water Wet	3	4
6	Water Wet	3	1

**Table 4.3 List of experiments.**

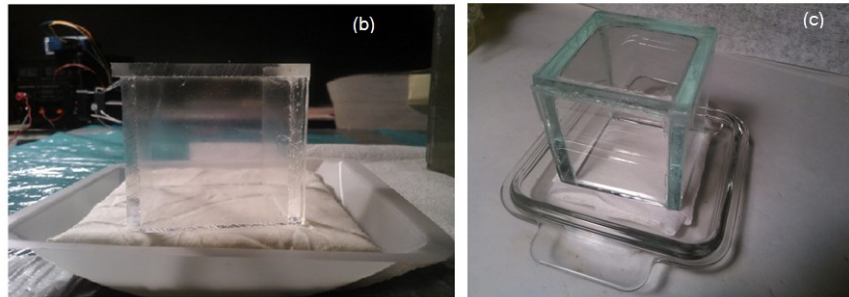
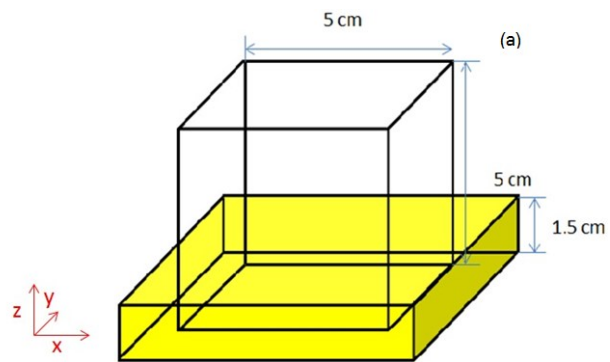


**Fig. 4.1 Dimension (a) of the oil-wet plexiglass (b) and water-wet glass (c) model.**

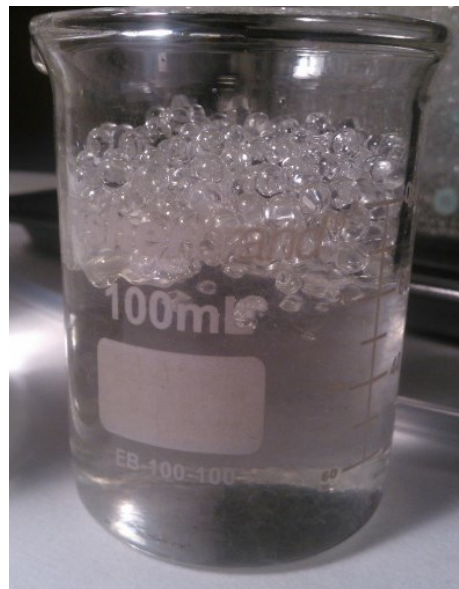


**Fig. 4.2 Invisible glass beads in the fluid (oleic phase) at the bottom and the glass beads in the air at the top.**

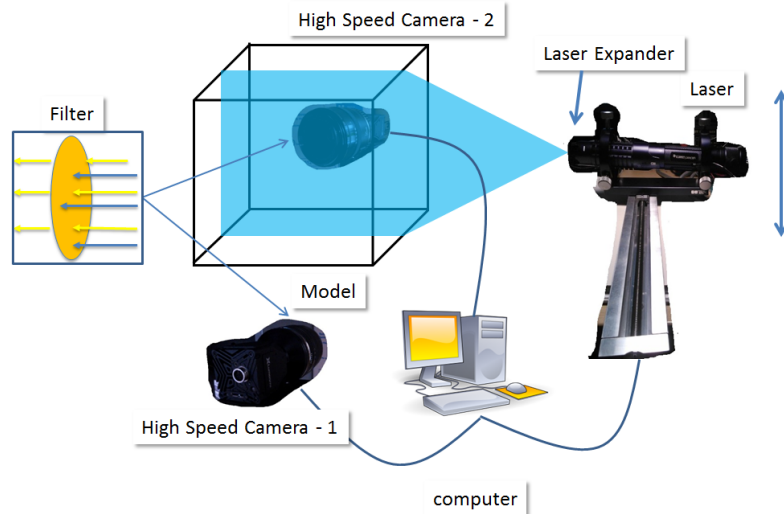


**Fig. 4.3 Laser imaging system set-up (Fang and Babadagli, 2014).**

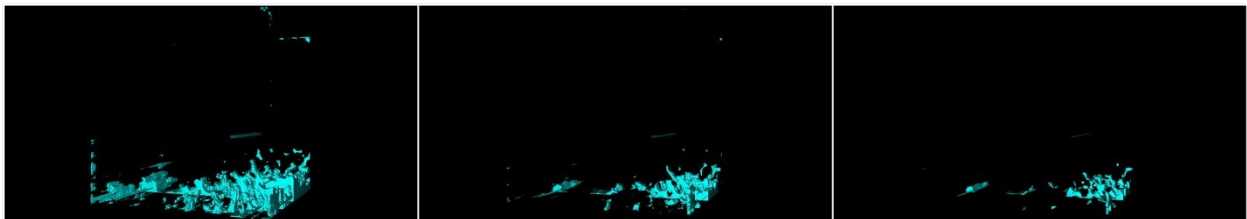


**Fig. 4.4 3-D surface images of solvent 1 diffusion into 4 mm glass beads packed plexiglass (oil-wet) wall model at 180 min with threshold at 50 (left), 80 (middle) and 100 (right).**

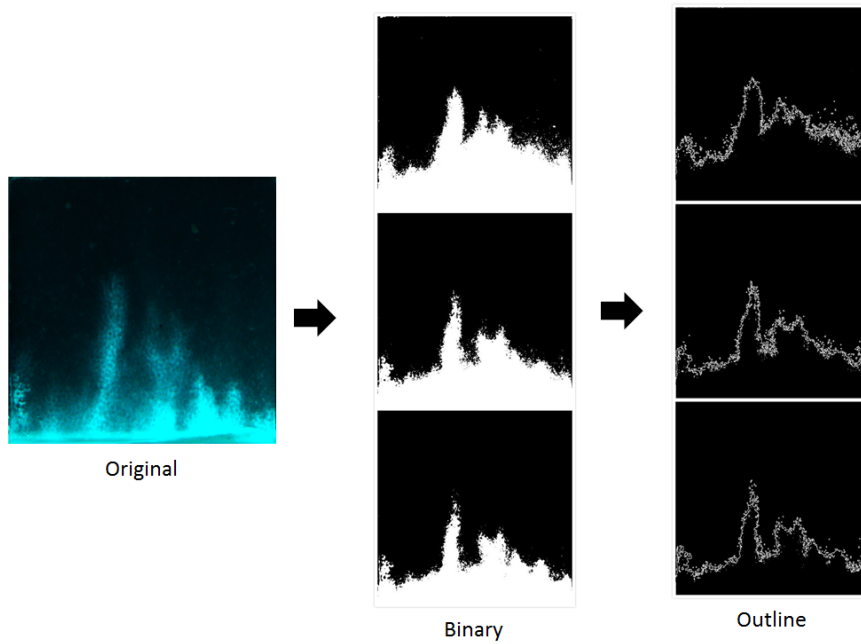


**Fig. 4.5 Image processing for fractal dimension calculation from original images to binary images and outline images with thresholds of 50 (top), 80 (middle) and 100 (bottom).**

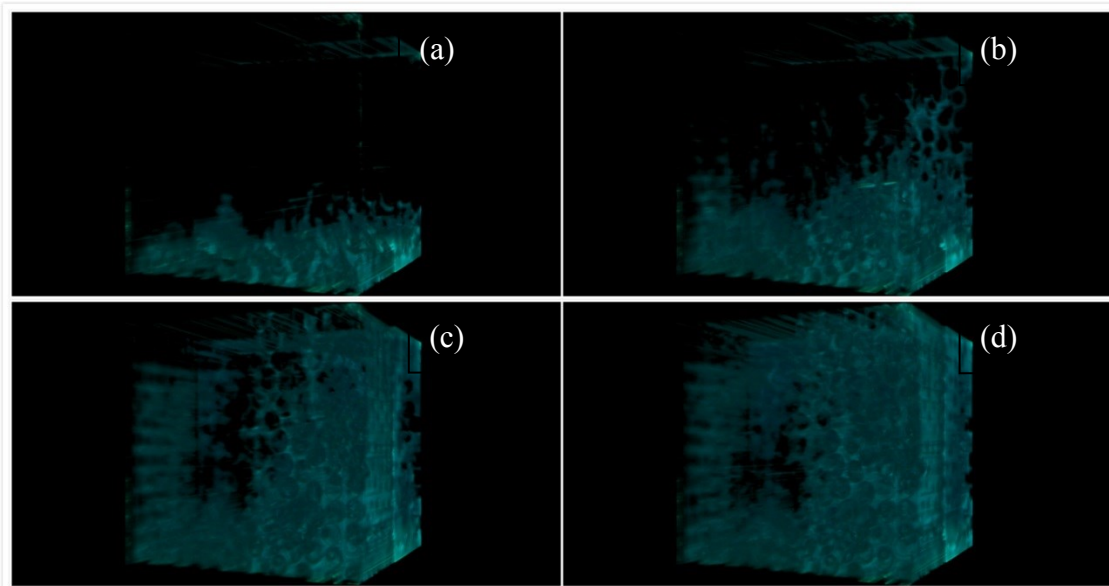


**Fig. 4.6 Solvent 1 diffusion into 4 mm glass beads packed plexiglass (oil-wet) wall model at 3 hrs (a), 6 hrs (b), 8 hrs (c), and 10 hrs (d).**

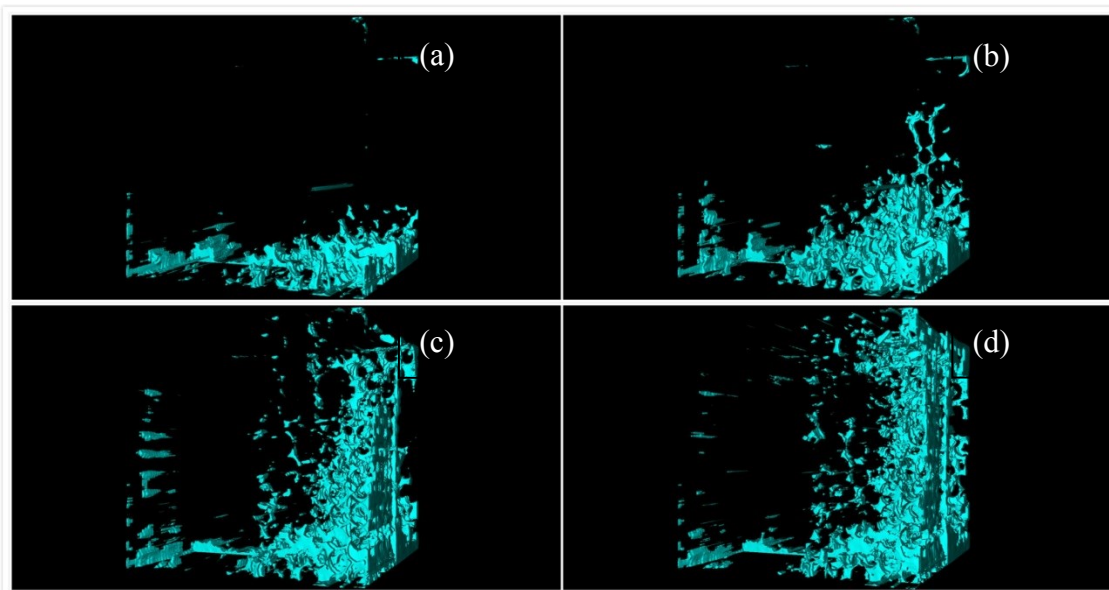


**Fig. 4.7 3-D surface images at threshold of 50 of solvent 1 diffusion into 4 mm glass beads packed plexiglass (oil-wet) wall model at 3 hrs (a), 6 hrs (b), 8 hrs (c), and 10 hrs (d).**

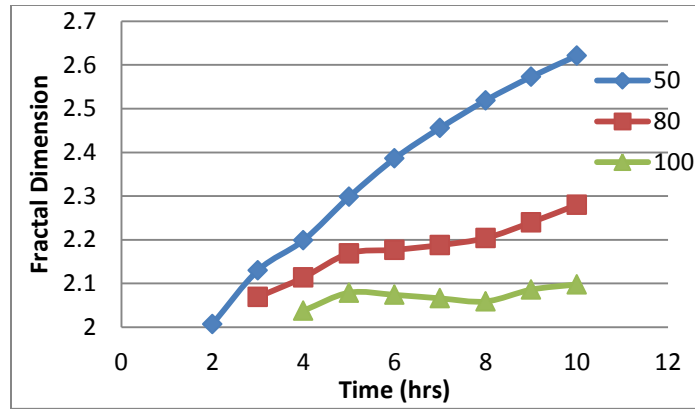


Fig. 4.8 Fractal dimension of Solvent 1 diffusion into 4 mm glass beads packed plexiglass (oil-wet) wall model with thresholds of 50, 80 and 100.

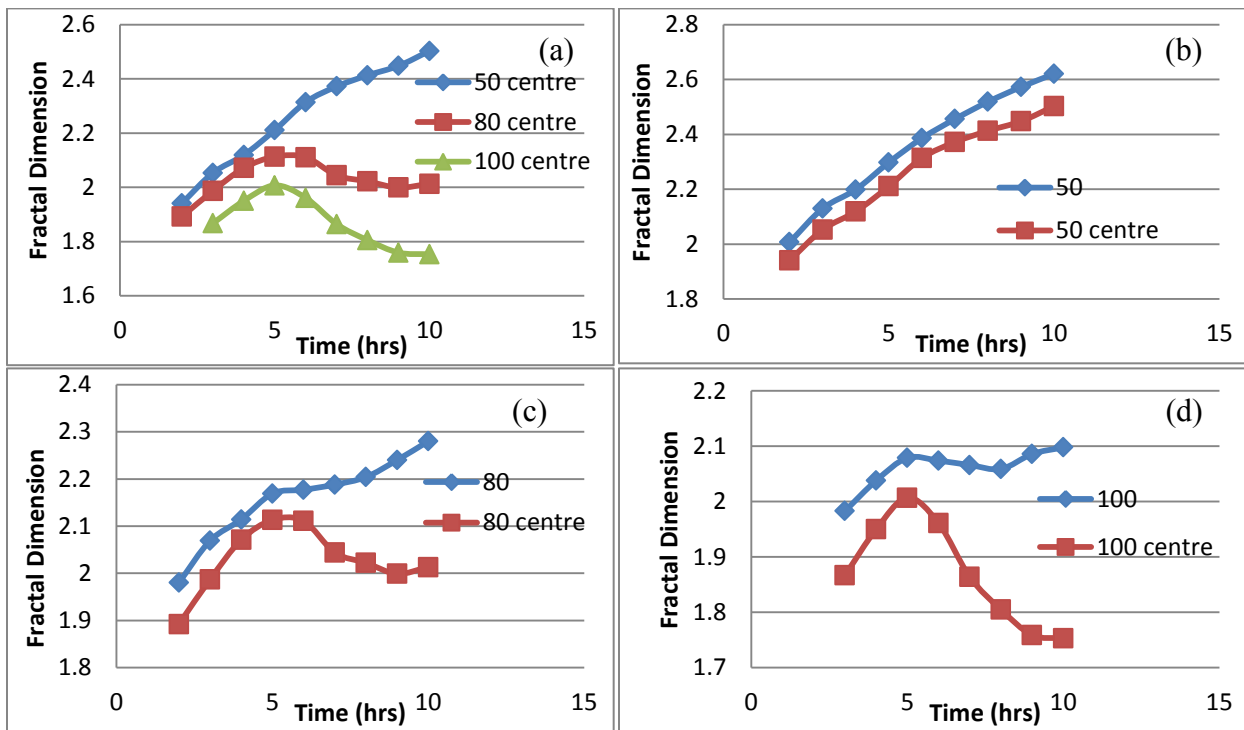


Fig. 4.9 Fractal dimension in the center of solvent 1 diffusion in 4 mm glass beads packed plexiglass (oil-wet) wall model at different threshold (a), comparison with the whole model with thresholds of 50 (b), 80 (c), and 100 (d).

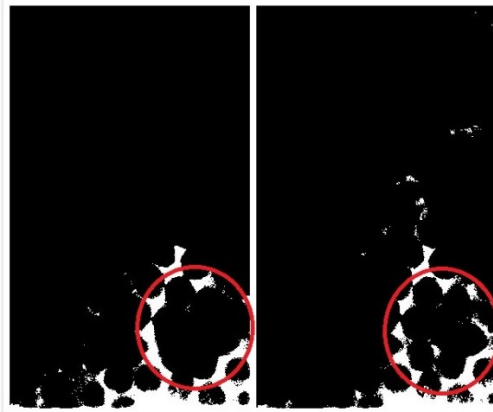


Fig. 4.10 Solvent 1 fill the pores at 3.6 cm from the front surface at 6 hrs (left) and 8 hrs (right) with a threshold of 80.

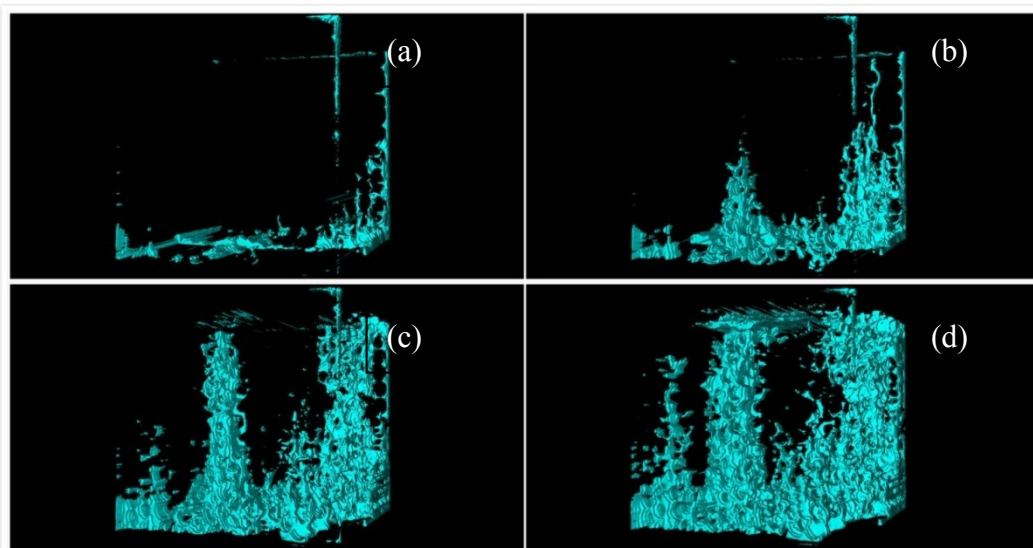


Fig. 4.11 3-D surface images at threshold of 50 of solvent 2 diffusion into 4 mm glass beads packed plexiglass (oil-wet) wall model at 3 hrs (a), 7 hrs (b), 11 hrs (c), and 15 hrs (d).

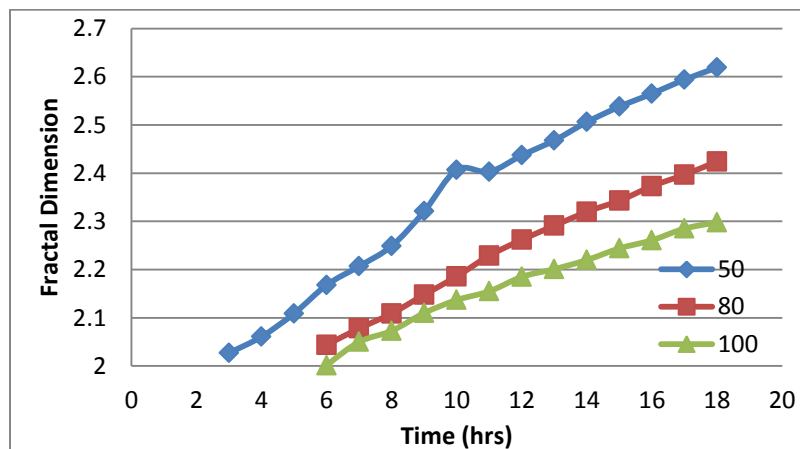


Fig. 4.12 Fractal dimension of Solvent 2 diffusion into 4 mm glass beads packed plexiglass (oil-wet) wall model with thresholds of 50, 80 and 100.

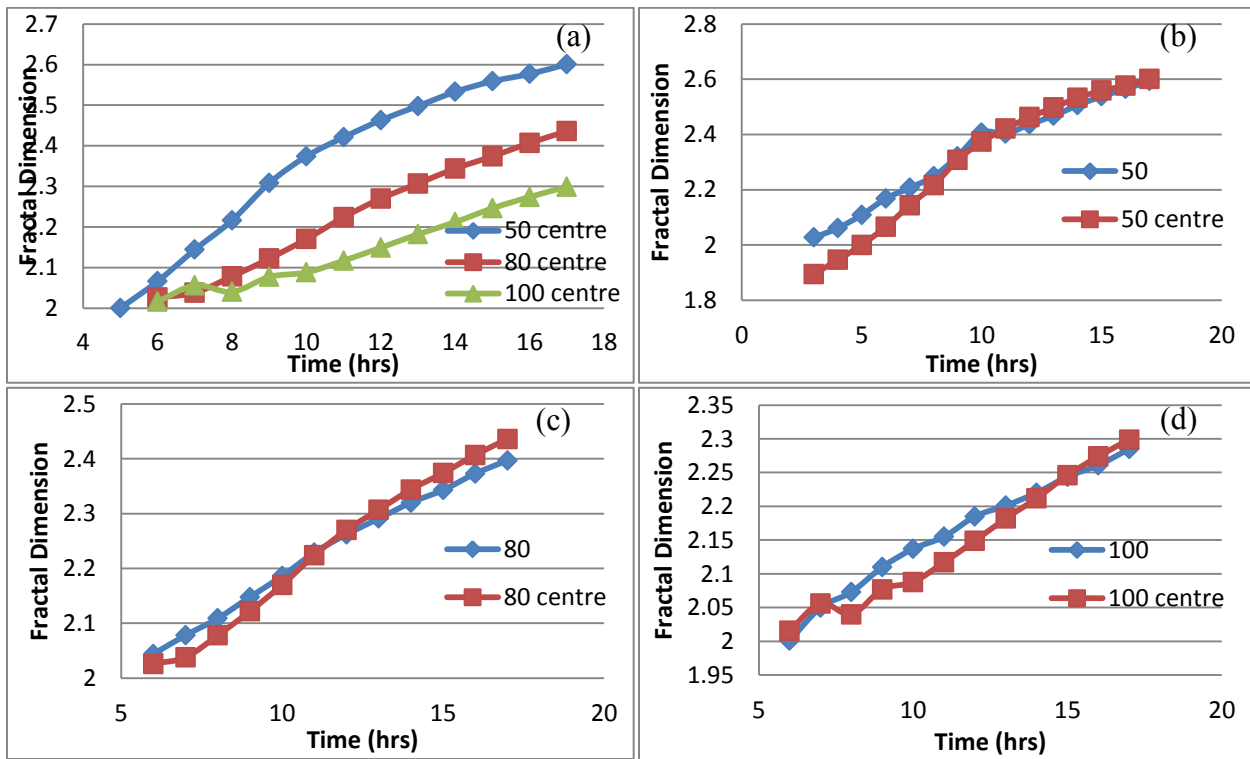


Fig. 4.13 Fractal dimension in the center of solvent 2 diffusion in 4 mm glass beads packed plexiglass (oil-wet) wall model at different thresholds (a), comparison with the whole model with threshold of 50 (b), 80 (c), and 100 (d).

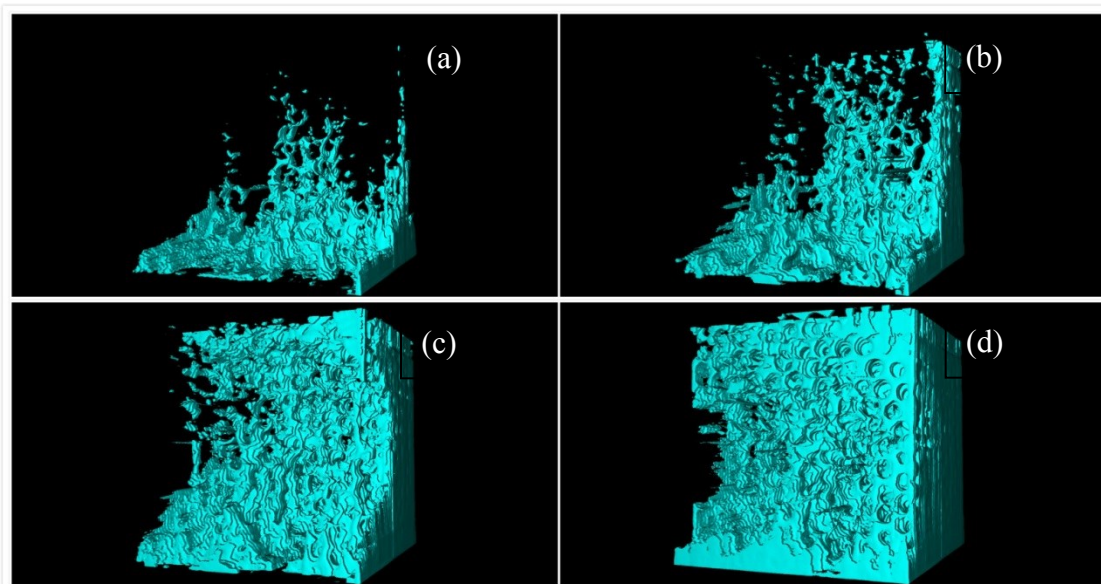


Fig. 4.14 3-D surface images at threshold of 50 of solvent 2 diffusion into 4 mm glass beads packed glass (water-wet) wall model at 3 hrs (a), 5 hrs (b), 8 hrs (c), and 11 hrs (d).

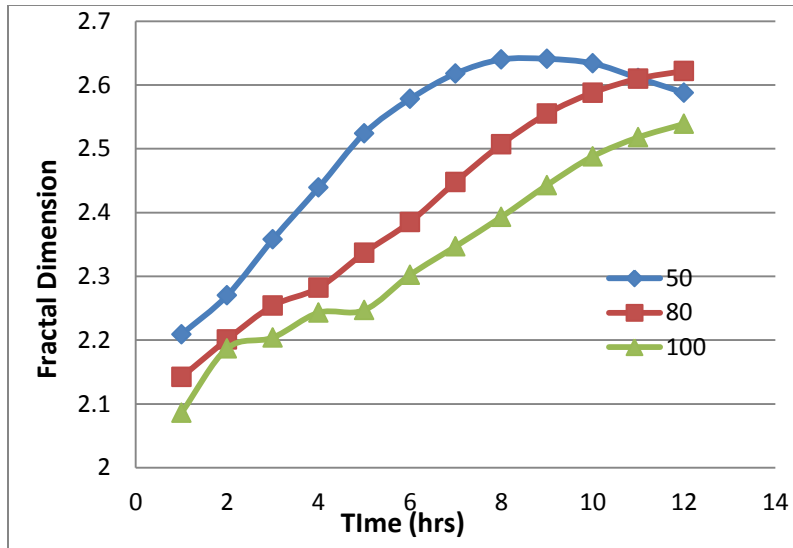


Fig. 4.15 Fractal dimension of Solvent 2 diffusion into 4 mm glass beads packed glass (water-wet) wall model with thresholds of 50, 80 and 100.

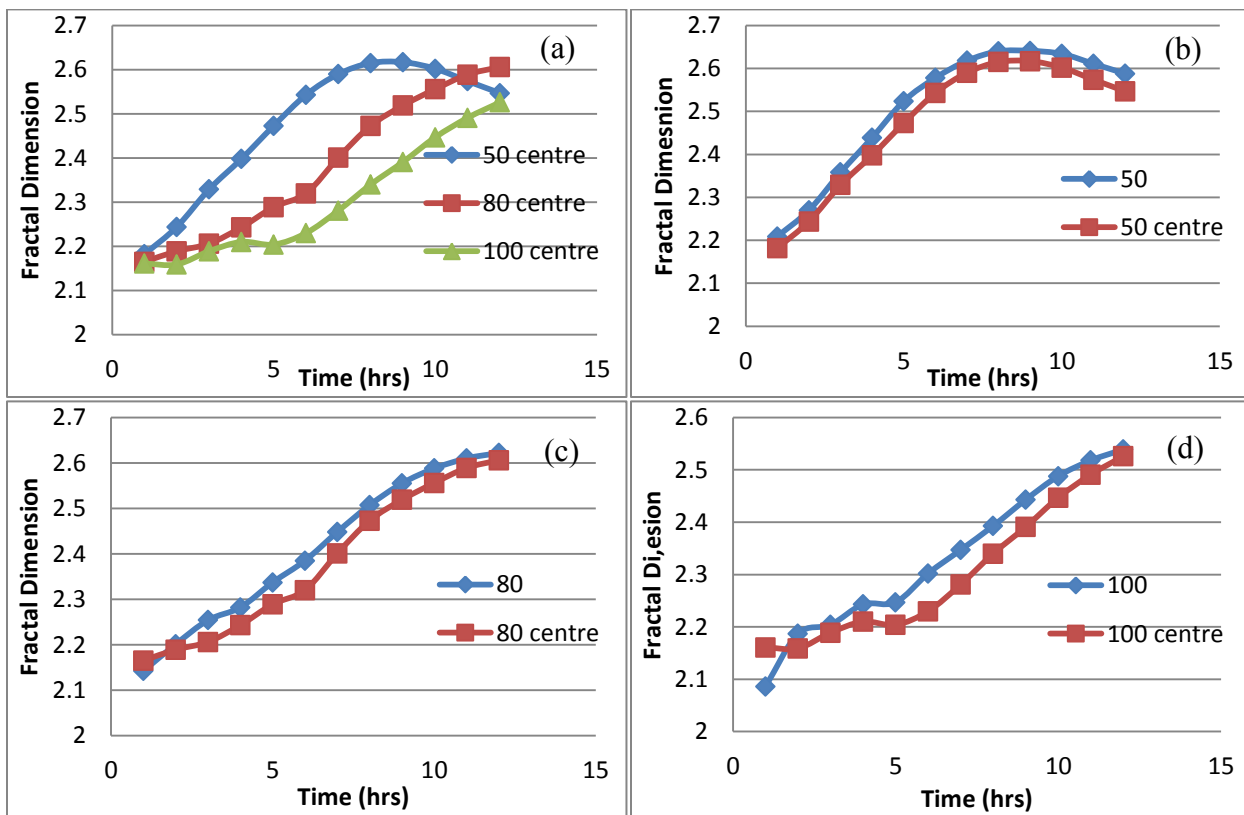
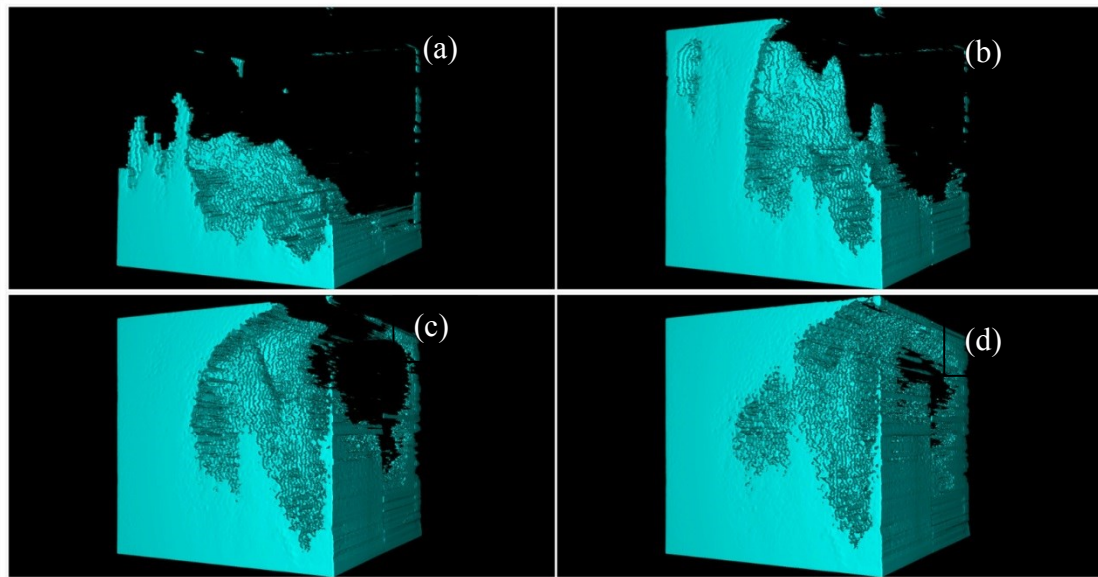
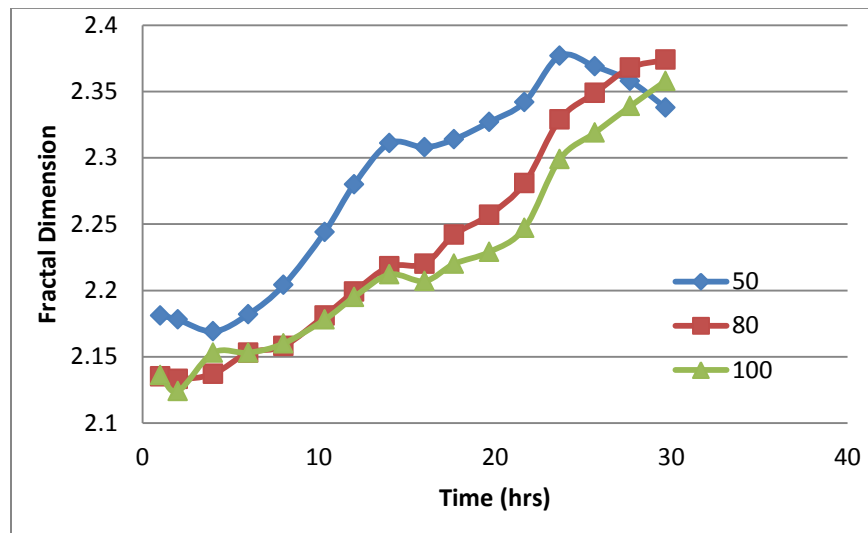


Fig. 4.16 Fractal dimension in the center of solvent 2 diffusion in 4 mm glass beads packed glass (water-wet) wall model at different thresholds (a), and comparison with the whole model with thresholds of 50 (b), 80 (c), and 100 (d).



**Fig. 4.17** 3-D surface images at thresholds of 50 of solvent 2 diffusion into 1 mm glass beads packed glass (water-wet) wall model at 8 hrs (a), 16 hrs (b), 24 hrs (c), and 32 hrs (d).



**Fig. 4.18** Fractal dimension of Solvent 2 diffusion into 1 mm glass beads packed glass (water-wet) wall model with thresholds of 50, 80 and 100.

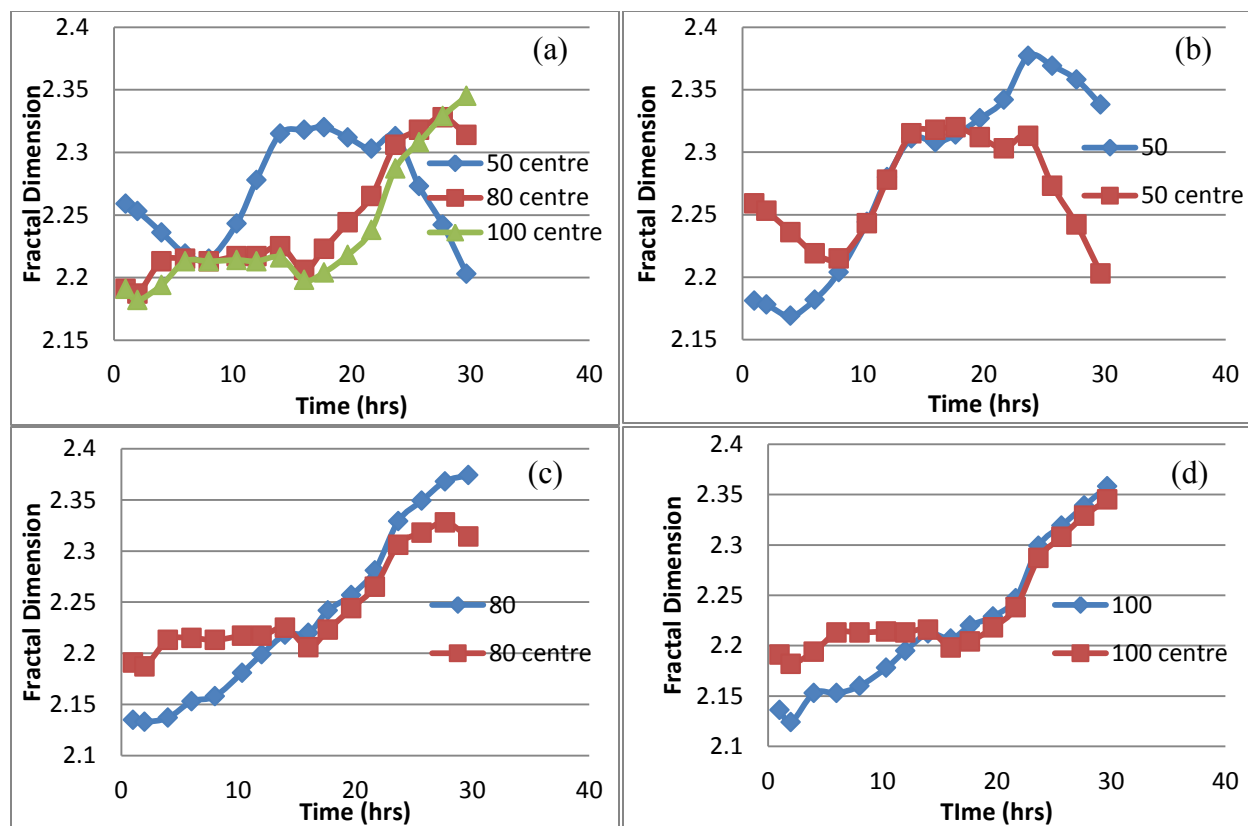


Fig. 4.19 Fractal dimension in the center of solvent 2 diffusion in 1 mm glass beads packed glass (water-wet) wall model at different thresholds (a), and comparison with the whole model with thresholds of 50 (b), 80 (c), and 100 (d).

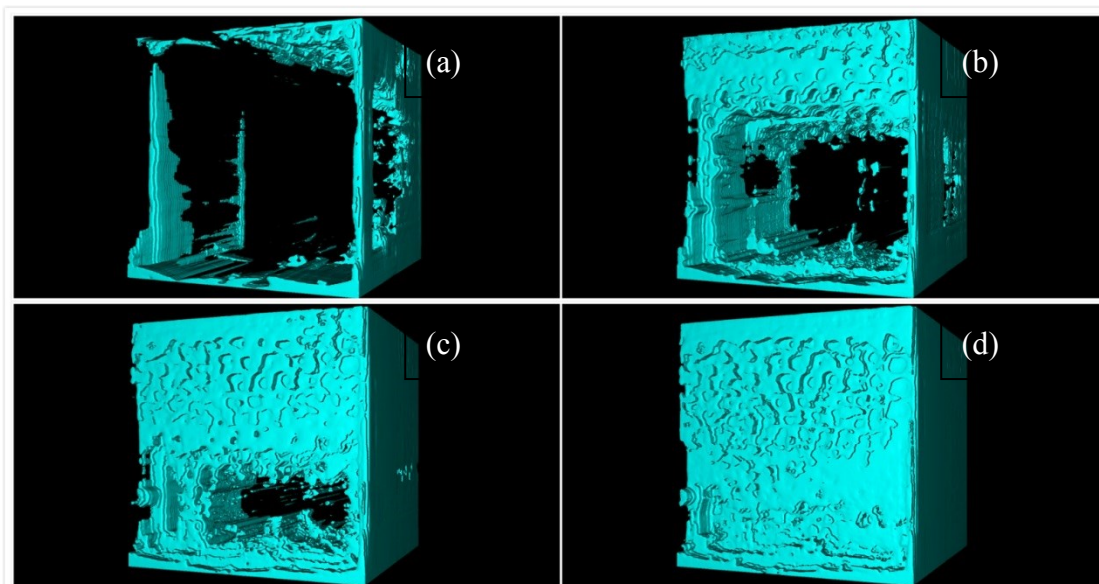


Fig. 4.20 3-D surface images at threshold of 50 of solvent 1 diffusion into 1 mm glass beads packed glass (water-wet) wall model at 5 min (a), 1 hrs (b), 2 hrs (c), and 3 hrs (d).

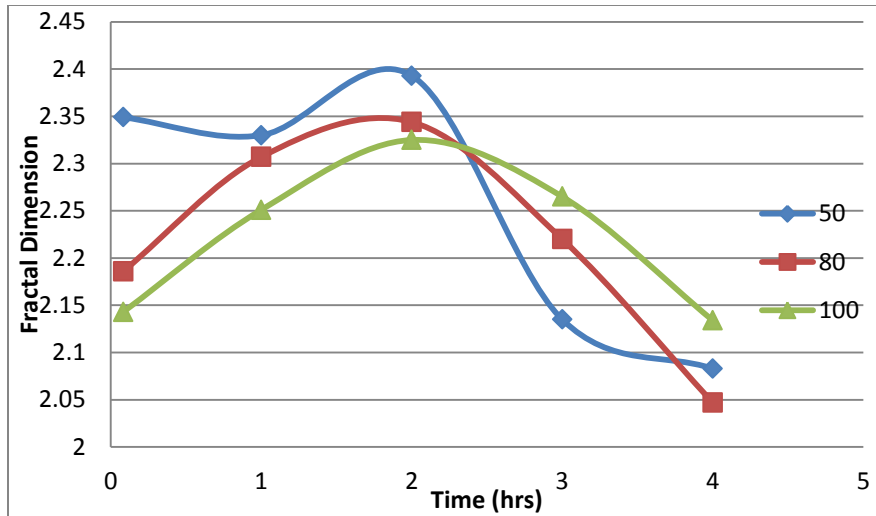


Fig. 4.21 Fractal dimension of Solvent 3 diffusion into 4 mm glass beads packed glass (water-wet) wall model with thresholds of 50, 80 and 100.

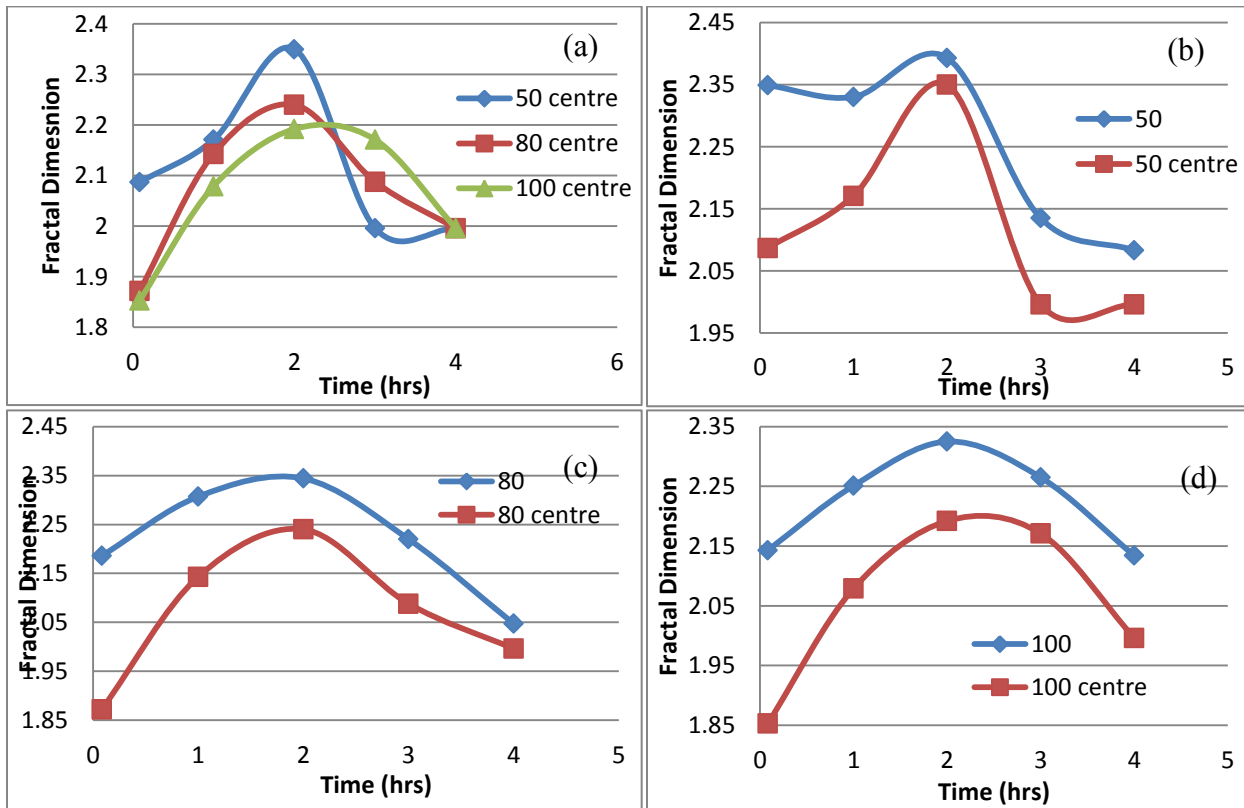


Fig. 4.22 Fractal dimension in the center of solvent 3 diffusion in 4 mm glass beads packed glass (water-wet) wall model at different thresholds (a), and comparison with the whole model with thresholds of 50 (b), 80 (c), and 100 (d).

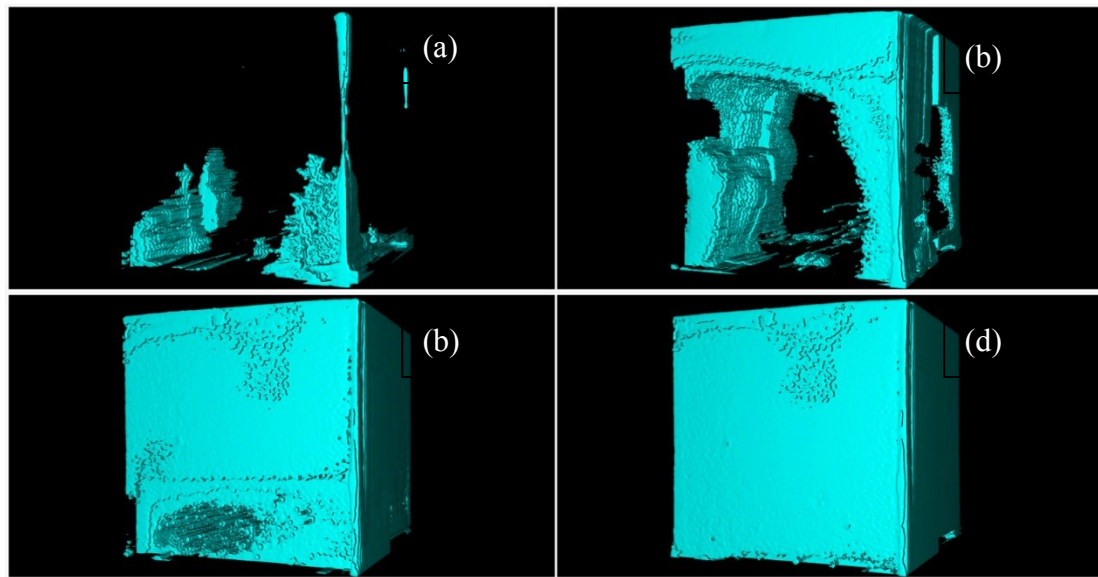


Fig. 4.23 3-D surface images at a threshold of 50 of solvent 1 diffusion into 1 mm glass beads packed glass (water-wet) wall model at 5 min (a), 1 hrs (b), 4 hrs (c), and 7 hrs (d).

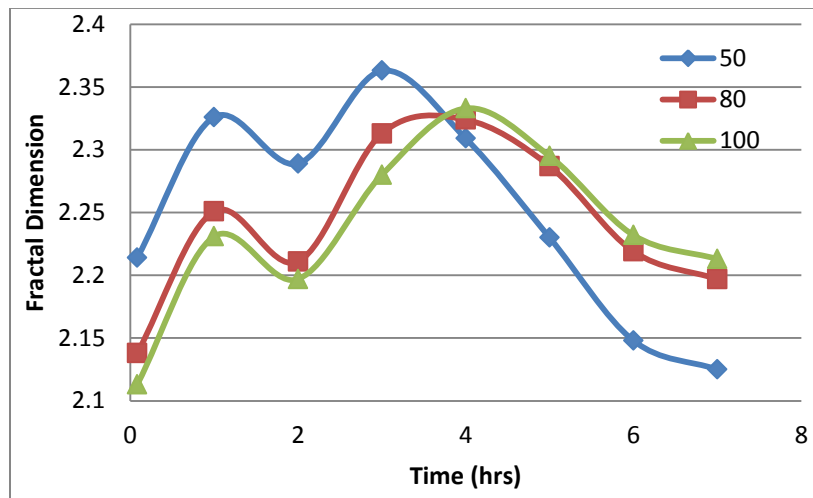


Fig. 4.24 Fractal dimension of Solvent 3 diffusion into 1 mm glass beads packed glass (water-wet) wall model with thresholds of 50, 80 and 100.

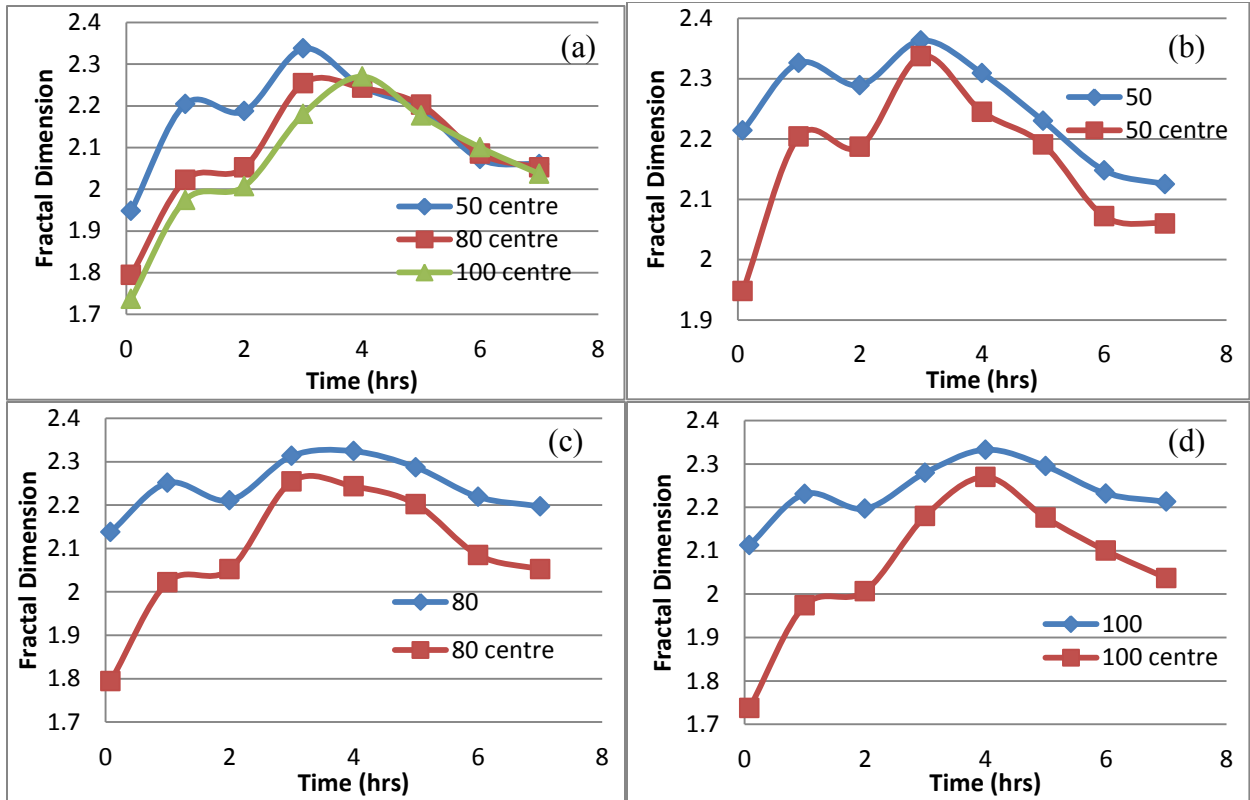


Fig. 4.25 Fractal dimension in the center of solvent 3 diffusion in 1 mm glass beads packed glass (water-wet) wall model at different thresholds (a), and comparison with the whole model with thresholds of 50 (b), 80 (c), and 100 (d).

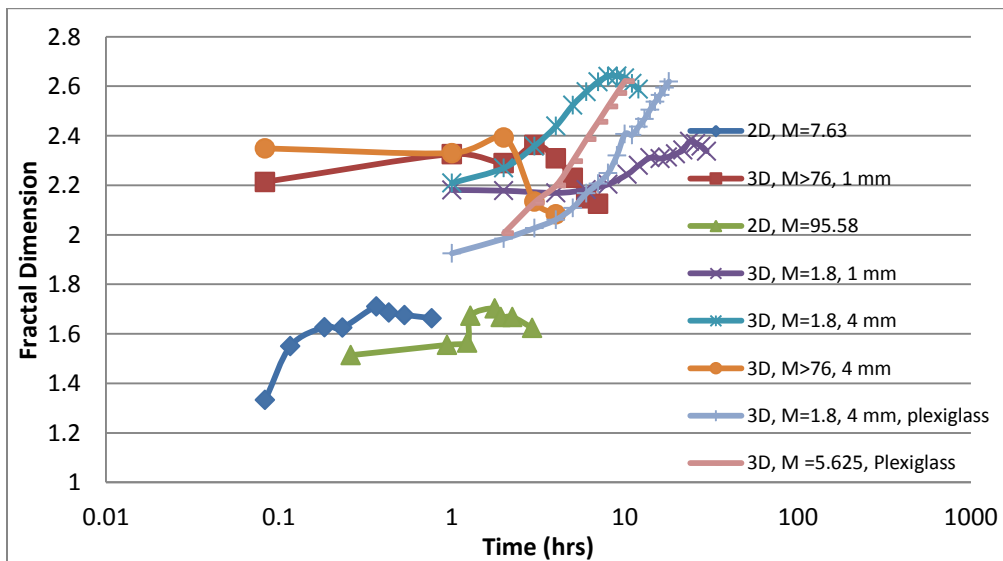
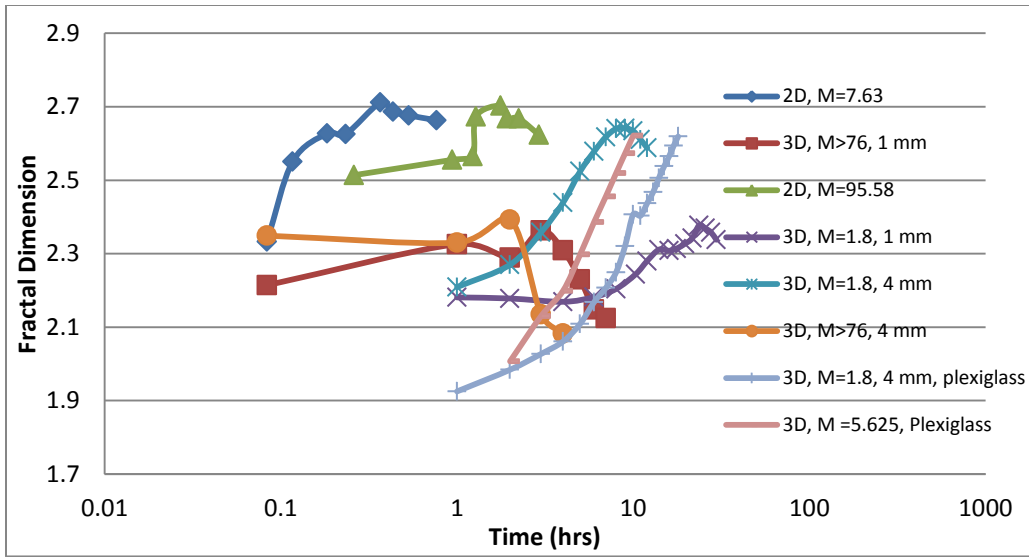


Fig. 4.26 Comparison of 3-D and 2-D behavior (or fractal dimensions). 2-D data (blue diamond and green triangles) are from Hatiboglu and Babadagli (2005).



**Fig. 4.27 Comparison of 3-D fractal dimension with “3-D versions” of 2-D fractal dimension (by adding 1 to the values given in Fig. 4.26).**

## **CHAPTER 5: Conclusions and Recommendations**

---

## 5.1 Conclusions and Contributions

Use of hydrocarbon solvents in enhanced oil/heavy-oil recovery processes has received remarkable attention recently. The main advantage of solvent -dilution- processes is that it is energy efficiency compared to thermal process. The energy required by VAPEX was estimated to be approximately only 3% of that for SAGD (Torabi et al., 2012). Such non-thermal processes have also an advantage on the environmental side. However, considering the price of hydrocarbon solvent, an optimum design is required to reduce the cost of solvent. This implies that the choice of optimal injection rate and ideal solvent type to maximize the recovery and minimize the cost is essential. This requires maximized sweep and larger contact areas between the injected solvent and rock matrix and oil. 3-D visualization of the process is critically important and therefore this research focused on this for different solvent injection applications involved in displacement by viscous and gravitational forces, and solvent oil-interaction (mass transfer) by diffusion and convection. The major achievements made in this thesis and the limitations of the technique are listed below:

- High resolution 2-D stack images of solvent displacement processes were obtained by matching the refractive indices of the solvent, oleic, and solid phases for different size models with and without solvent injection options. The solvent colored by fluorescent dyes in the transparent model, containing three phases (oil solvent and glass beads) of which the refractive indices were matched, were observed with the excitation of blue laser.
- The visualization system was created using two identical cameras to take pictures from the front and the back side every time the laser sheet was moved by 1 mm. The 2-D stack images were converted to an animated movie by integrating them and the video of the process was analyzed through a 3-D visualization system (virtual reality).

- The size of the model was limited depending on the size of glass beads and concentration of fluorescent dyes or solvent due to the scattering and refraction at the surface of glass beads.
- The brightness in the images did not exactly represent the concentration of the solvent since the light was absorbed by the fluids and the glass beads along the light path.
- To process the images, a threshold was set to select the data lighter than certain brightness. Since the solvent was diffused in the oil, the threshold filtered some low solvent concentration region.
- The 3-D images only showed the bulk of diffused volume, but did not display the concentration of the solvent. However, by setting different values in the threshold step, the difference of the volumes represents the mixing zone.

In Chapter 3 we defined the optimum injection method through visual inspection of sweep efficiency from the shape and size of the solvent chamber in the 3-D videos. Quantitative analysis was also achieved using the recorded production rate. The shape and progress speed of the solvent chamber for a light solvent significantly differ from a viscous and denser solvent. The main conclusions of this chapter are listed below:

- The solvent chamber was wider, taller, and dome-shaped when the injection pressure was high.
- Due to the pressure loss along the wells, the chamber became smaller in both horizontal and vertical directions but had less effect on the height.
- Viscous fingering was observed at the top of the solvent chamber.

- After the solvent had spread along the ceiling, it started to displace the oil downward, wherein the interface with oil tilted towards the rising solvent chamber in the middle. The shape of solvent boundary was found to be dependent on the initial injection rate.
- Light and thin solvent formed a thin solvent chamber.
- Light and thin solvent rose much faster, but the injection distance along the well was shorter.
- Flowing through the low permeability zone in the middle, the solvent chamber became wider and entered the high permeability zone through multiple points.
- The solvent chamber was less uniform in a tighter reservoir.

From the “diffusion experiments” (static models) given in Chapter 4, we can conclude that:

- The width of the solvent swept region depended on the density of the solvent.
- The speed of the process was faster in the high permeability porous media.
- Boundary effect existed in both plexiglass and glass model being more prominent with the solvent with extremely low viscosity.
- Solvents 1 (higher density but less viscosity than oil) and 2 (higher viscosity than the other solvents but less viscosity than the oil) propagated into the model from the whole bottom of the model, while thin and light solvent 3 reached the top in a short period of time and propagated from the top of model downward, representing a convective transport.
- The fractal dimension increased before the solvent reached at the top of the model and reached a peak value.
- The fractal dimension increased as the solvent propagated from top to bottom in light and thin solvent case.
- The fractal dimension dropped as the solvent filled the unswept pores.

## 5.2 Recommendations

- Different material with different permeability and pore sizes of the well can be used in the VAPEX experiments to find an optimum well type for a more uniform chamber distribution along the injector.
- Doorwar and Mohanty (2011) indicated that the space between viscous fingers is smaller as the viscosity ratio increases. A larger diffusion model can be used to determine if the strong wall effect for solvent 3 (light and thin) is due to the space between fingers.
- Oil with higher viscosity can be used to represent Canadian heavy-oil cases more realistically. The viscosity of mixture used as the oleic phase was 45 cP because refractive index matching requires mixture of fluids with low and high refractive indices. However, fluid with low refractive index has low viscosity and reduces the viscosity of the mixture sharply. If a special oil has high viscosity but low refractive index can be obtained for refractive index matching, this goal could be reached.

### 5.3 References

- Torabi, F., Jamaloei, B.Y., Stengler, B.M. et al. 2012. The Evaluation of CO<sub>2</sub>-Based Vapor Extraction (VAPEX) Process for Heavy-Oil Recovery. *Journal of Petroleum Exploration and Production Technology* **2** (2): 93-105. [http://dx.doi.org/ 10.1007/s13202-012-0025-y](http://dx.doi.org/10.1007/s13202-012-0025-y).
- Doorwar, S. and Mohanty, K. 2011. Viscous Fingering during Non-Thermal Heavy Oil Recovery. SPE-146841-MS paper presented at Annual Technical Conference and Exhibition, Denver, Colorado, USA, 30 October-2 November. <http://dx.doi.org/10.2118/146841-MS>.

## References

- Al-Bahlani, A.M. and Babadagli, T. 2009. SAGD Laboratory Experimental and Numerical Simulation Studies: A Review of Current Status and Future Issues. *J. Petr. Sci. and Eng.* **68** (3–4): 135–150. <http://dx.doi.org/10.1016/j.petrol.2009.06.011>.
- Alkindi, A.S., Al-Wahaibi, Y. M., Muggeridge, A. 2011. Experimental and Numerical Investigations into Oil-Drainage Rates during Vapor Extraction of Heavy Oils. *SPE J.* **16** (2): 343-357. <http://dx.doi.org/10.2118/141053-PA>.
- Butler R. and Morkys I.J. 1989. Solvent Analog Model of Steam-Assisted Gravity Drainage. *AOSTRA J Res* **5** (1):1-8. <http://dx.doi.org/10.2118/93-03-02>.
- Butler, R. M. 1985. A New Approach to the Modelling of Steam-Assisted Gravity Drainage. *JCPT.* **24** (03). <http://dx.doi.org/10.2118/85-03-01>.
- Butler, A.M. and Morkys, I.J. 1992. Recovery Of Heavy Oils Using Vaporized Hydrocarbon Solvents: Further Development Of The Vapex Process. Paper SS-92-7 presented at Technical Meeting/Petroleum Conference of The South Saskatchewan Section, Regina, Saskatchewan, Canada, 7 - 9 October. <http://dx.doi.org/10.2118/SS-92-7>.
- Butler, R. M. and Yee, C. T. 2002. Progress in the In Situ Recovery of Heavy Oils and Bitumen. *JCPT.* **41** (1). <http://dx.doi.org/10.2118/02-01-02>.
- Cessou1, A., Meier, U., and Stepowski, D. 2000. Applications of Planar Laser Induced Fluorescence in Turbulent Reacting Flows. *Meas. Sci. Technol.* **11** :887. <http://dx.doi.org/10.1088/0957-0233/11/7/305>.
- Chao, Y.C., Han, J.M., and Jeng, M.S. 1990. A Quantitative Laser Sheet Image Processing Method for the Study of the Coherent Structure of a Circular Jet Flow. *Experiments in Fluids* **9**: 323-332. <http://dx.doi.org/10.1007/BF00188761>.
- Chen, J.D. and Wada, N. 1986. A New Technique for visualizing the Distribution of Oil, Water, and Quartz Grains in a Transparent, Three-Dimensional, Porous Medium. *SPE Form Eval* **1** (2):205-208. <http://dx.doi.org/10.2118/13349-PA>.
- Chen, B., Mikamib, F., Nishikawab, N. 2005. Experimental Studies on Transient Features of Natural Convection in Particles Suspensions. *International Journal of Heat and Mass Transfer* **48** (14): 2933–2942. <http://dx.doi.org/10.1016/j.ijheatmasstransfer.2004.11.016>.
- Collins, P. M. 2007. The False Lucre of Low-Pressure SAGD. *JCPT* **46** (1). <http://dx.doi.org/10.2118/07-01-02>.
- Cuthiell, D., McCarthy, C., Frauenfeld, T., et al. 2003. Investigation of the VAPEX Process Using CT Scanning and Numerical Simulation. *JCPT* **42** (2). <http://dx.doi.org/10.2118/03-02-04>.
- Das, S. K. 1998. VAPEX: An Efficient Process for the Recovery of Heavy Oil and Bitumen. *SPE J.* **3**: 232-267. <http://dx.doi.org/10.2118/50941-PA>.
- Das, S. K. and Bulter, R. M. 1998. Mechanism of the Vapor Extraction Process for Heavy Oil and Bitumen. *Journal of Petroleum Science and Engineering* **21** (1-2): 43–59. [http://dx.doi.org/10.1016/S0920-4105\(98\)00002-3](http://dx.doi.org/10.1016/S0920-4105(98)00002-3).
- Das, S. 2005. Improving the Performance of SAGD. SPE-97921-MS presented at the SPE International Thermal Operations and Heavy Oil Symposium, Calgary, Alberta, Canada, 1-3 November. <http://dx.doi.org/10.2118/97921-MS>.

- Doorwar, S., and Mohanty, K., 2011. Viscous Fingering during Non-Thermal Heavy Oil Recovery. SPE-146841-MS paper presented at Annual Technical Conference and Exhibition, Denver, Colorado, USA 30 October-2 November. <http://dx.doi.org/10.2118/146841-MS>.
- Fang, F. and Babadagli, T. 2014. Three Dimensional Visualization of Solvent Chamber Growth in Solvent Injection Processes: An Experimental Approach. SPE 170649 presented at SPE Annual Technical Conference & Exhibition, Amsterdam, Netherlands, 27-30 October. <http://dx.doi.org/10.2523/IPTC-18115-MS>.
- Fang, F. and Babadagli, T. 2014. Three Dimensional Visualization of Solvent Chamber Growth in Solvent Injection Processes: An Experimental Approach. Paper IPTC 18115, presented at the Int. Petr. Tech. Conf. (IPTC), Kuala Lumpur, Malaysia, 10-12 Dec. <http://dx.doi.org/10.2523/IPTC-18115-MS>.
- Fayers, F.J. and Ann H.M. 1990. Extensions to Dietz Theory and Behavior of Gravity Tongues in Slightly Tilted Reservoirs. *SPE* **5** (4): 487–494. <http://dx.doi.org/10.2118/18438-PA>.
- Gates, I.D., Kenny, J., Hernandez-Hdez, I.L., et al. 2007. Steam Injection Strategy and Energetics of Steam-Assisted Gravity Drainage. *SPE Reservoir Evaluation & Engineering* **10** (1): 19–34. <http://dx.doi.org/10.2118/97742-PA>.
- Gharbi, R.B.C., Qasem, F., and Peters, E.J. 2001. A Relationship Between the Fractal Dimension and Scaling Groups of Unstable Miscible Displacements. *Experiments in Fluids* **31** (4):357-366
- Hatiboglu, C. U. and Babadagli, T. 2004. Experimental Analysis of Primary and Secondary Oil recovery from Matrix by Counter-Current Diffusion and Spontaneous Imbibition. SPE 90312 paper presented at the SPE Annual Technical Conference and Exhibition, Houston, TX, 26-29 September. <http://dx.doi.org/10.2118/90312-MS>.
- Hatiboglu, C.U. and Babadagli, T. 2005. Visualization Studies on Matrix- Fracture Transfer Due to Diffusion. Paper 2005-077 presented at the Canadian International Petroleum Conference, Calgary, Alberta, Canada, 7-9 June. <http://dx.doi.org/10.2118/2005-077>.
- Hatiboglu, C.U. and Babadagli, T. 2007a. Oil recovery by counter-current spontaneous imbibition: Effects of matrix shape factor, gravity, IFT, oil viscosity, wettability, and rock type. *J. Pet. Sci. and Eng.* **59** (1-2): 106-122. <http://dx.doi.org/10.1016/j.petrol.2007.03.005>.
- Hatiboglu, C.U. and Babadagli, T. 2007b. Lattice-Boltzmann Simulation of Solvent Diffusion into Oil-Saturated Porous Media. *Phys. Rev. E* **76**. <http://dx.doi.org/10.1103/PhysRevE.76.066309>.
- Hatiboglu, C.U. and Babadagli, T. 2008. Diffusion Mass Transfer in Miscible Oil Recovery: Visual Experiment and Simulation. *J Transport in Porous Media* **74** (2): 169-184. <http://dx.doi.org/10.1007/s11242-007-9189-1>.
- Hatiboglu, C.U. and Babadagli, T. 2010. Experimental and Visual Analysis of Co-and Counter-Current Spontaneous Imbibition for Different Viscosity Ratios, Interfacial Tensions, and Wettabilities. *J. Pet. Sci. and Eng.* **70** (3-4): 214-228. <http://dx.doi.org/10.1016/j.petrol.2009.11.013>.
- Heller, W. 1945. The Determination of Refractive Indices of Colloidal Particles by Means of a New Mixture Rule or from Measurements of Light Scattering. *Phys. Rev. E.* **68**: 5–10. <http://dx.doi.org/10.1103/PhysRev.68.5>.

- Hut, J., Omrane, A., Nygren, J., Kaminski, et al. 2002. Quantitative Three-Dimensional Imaging of soot Volume Fraction in Turbulent Non-premixed Flames. *Experiments in Fluids* **33**: 265-269. <http://dx.doi.org/10.1007/s00348-002-0410-2>.
- Ito, Y. and Ipek, G. 2005. Steam-Fingering Phenomenon during SAGD Process. Paper SPE-97729 presented at the SPE International Thermal Operations and Heavy Oil Symposium, Calgary, Alberta, Canada, 1-3 November. <http://dx.doi.org/10.2118/97729-MS>.
- Ivory, J.J., Zheng, R., Nasr, T.N., et al. 2008. Investigation of Low Pressure ES-SAGD. SPE-117759-MS presented at International Thermal Operations and Heavy Oil Symposium, Calgary, Alberta, Canada, 20-23 October. <http://dx.doi.org/10.2118/117759-MS>.
- Jiang, Q. and Butler, R.M., 1996. Experimental Studies on Effects of Reservoir Heterogeneity on the Vapex Process. *JCPT* **35** (10): 46-54. <http://dx.doi.org/10.2118/96-10-04>.
- Lenormand, R. 1989. Flow through Porous Media: Limits of Fractal Pattern. *Proc. R. Soc. Lond. A* **423**: 159-168. <http://dx.doi.org/10.1098/rspa.1989.0048>.
- Li, J., Du, Q., and Sun, C. 2009. An Improved Box-Counting Method for Image Fractal Dimension Estimation. *Pattern Recognition* **42** (11): 2460-2469. <http://dx.doi.org/10.1016/j.patcog.2009.03.00>.
- Li, W., Mamora, D., Li, Y. and Qiu, F. 2011. Numerical Investigation of Potential Injection Strategies to Reduce Shale Barrier Impacts on SAGD Process. *JCPT* **50** (03): 57-64. <http://dx.doi.org/10.2118/133298-PA>.
- Lin, L., Zeng, F. and Gu, Y. 2014. A Circular Solvent Chamber Model for Simulating the VAPEX Heavy Oil Recovery Process. *Journal of Petroleum Science and Engineering* **118**: 27-39. <http://dx.doi.org/10.1016/j.petrol.2014.03.010>.
- Mavko, G. and Nur, A. 1997. The Effect of a Percolation Threshold in the Kozeny-Carman Relation. *Geophysics* **62**(1480-1482). <http://dx.doi.org/10.1190/1.1444251>.
- Monkrys, I.J. and Butler, R.M., 1993. The Rise of Interfering Solvent Chambers: Solvent Analog Model of Steam-Assisted Gravity Drainage. *JCPT*, 26-36. <http://dx.doi.org/10.2118/93-03-02>
- Nygren, J., Richter, M., Alden, M., et al. 2002. Three-Dimensional Laser Induced Fluorescence of Fuel Distribution in an HCCI Engine. Proc., Combustion Institute, **29** (679-685). [http://dx.doi.org/10.1016/S1540-7489\(02\)80087-6](http://dx.doi.org/10.1016/S1540-7489(02)80087-6).
- Ravalec, M. L.; Morlot, C.; Marmier R. and Foulon, D. 2009. Heterogeneity Impact on SAGD Process Performance in Mobile Heavy Oil Reservoirs. *Oil & Gas Science and Technology – Rev. IFP* **64** (4): 469-476. <http://dx.doi.org/10.2516/ogst/2009014>.
- Sasaki, K.S., Akibayashi, N., Yazawa, Q.T., et al. 2001. Experimental Modeling of the SAGD Process-Enhancing SAGD Performance with Periodic Stimulation of the Horizontal Producer. *SPE Journal* **6** (01): 89-97. <http://dx.doi.org/10.2118/69742-PA>.
- Sakakibara, J., Adrian, R. J. 1999. Whole Field Measurement of Temperature in Water Using Two-Color Laser Induced Fluorescence. *Experiments in Fluids*. **26** (1-2): 7-15. <http://dx.doi.org/10.1007/s003480050260>.
- Sharma, P., Aswathi, P., Sane, A., et al. 2011. Three-Dimensional Real-Time Imaging of Bi-Phasic Flow through Porous Media. *Review of Scientific Instruments*, **82**. <http://dx.doi.org/10.1063/1.3658822>.
- Sutton, J.A., Fisher, B.T., Fleming, J.W. 2008. A Laser-Induced Fluorescence Measurement for Aqueous Fluid Flows with Improved Temperature Sensitivity. *Experiments in Fluids*. **45** (5):

869-881. <http://dx.doi.org/10.1007/s00348-008-0506-4>.

Torabi, F., Jamaloei, B.Y., Stengler, B.M. et al. 2012. The Evaluation of CO<sub>2</sub>-Based Vapor Extraction (VAPEX) Process for Heavy-Oil Recovery. *Journal of Petroleum Exploration and Production Technology* 2 (2): 93-105. <http://dx.doi.org/10.1007/s13202-012-0025-y>.

Trivedi, J. and Babadagli, T. 2008. Efficiency of Diffusion Controlled Miscible Displacement in Fractured Porous Media. *Transport in Porous Media*. **71** (3): 379-394.

Wiederseiner, S., Andreini, N., Epely-Chauvin, G., et al. 2001. Refractive-Index and Density Matching in Concentrated Particle Suspensions: A Review. *Experiments in Fluids* **50**: 1183-1206. <http://dx.doi.org/10.1007/s00348-010-0996-8>.